Energy-Efficient Designs and Principles for Miniature Mobile Robotic Systems

A THESIS
SUBMITTED TO THE FACULTY OF THE GRADUATE SCHOOL
OF THE UNIVERSITY OF MINNESOTA
BY

APOSTOLOS DIMITRIOS KOTTAS

IN PARTIAL FULFILLMENT OF THE REQUIREMENTS
FOR THE DEGREE OF
MASTER OF SCIENCE

Advisor: Nikolaos Papanikolopoulos, Professor

JUNE, 2012

Energy-Efficient Designs and Principles for Miniature Mobile Robotic Systems

by APOSTOLOS DIMITRIOS KOTTAS

ABSTRACT

Mobile robots are only as useful as their limited, abatable energy sources allow them to be. There are many components onboard a mobile robot, which are investigated in variable detail, each contributing differently to the reduction in available energy. Embedding power-aware characteristics in mobile systems is a widely studied topic - on many levels. In this thesis, it begins with a robot's ability to maintain an active profile of its energy expenditure, as well as its remaining energy. To address these demands, a versitile fuel-gauge circuit was designed and integrated across several different robotic systems. The end-design offers a scalable means to accurately monitor a battery's dynamics, while providing a simple, and moreover safe solution for integrating Li-ion technologies in mobile robots.

Acknowledgements

I have so many people to thank for several different things. First and foremost, I am forever grateful to my parent, Dimitrios and Ioanna, and my sister Andromache. Without your wisdom and advice I cannot imagine where I would be. Thank you for your understanding, for your constant support, and for tolerating my constant absence from home - amidst the long nights in the lab.

I am very thankful for all the invaluable advice from Robert Terhaar. Thank you for listening, for always offering suggestions, talking me through whatever problems I would get stuck on, and for helping with some figures.

I am vastly indebted to Andrew Drenner and Ian Burt for their assistance and mentorship at the Center for Distributed Robotics Laboratory, from the time I started in the lab as an undergraduate - eight (long) years ago. Thank you for making yourselves available, and for your help in so many of the projects I lost myself in throughout my years at the lab.

I would like to thank Sandeep Dhull for his contributions in developing custom software to automate collection of some data that would otherwise have been very cumbersome and time consuming. I owe a huge thank you to Ruben D'Sa for all his contributions with mechanical systems modeling of the robots discussed in this work. Finally I would like to thank Justin Dancs and Alex Kossett for their assistance in mechanical modeling formulation and validation.

Contents

List of Tables

List of Figures

Chapter 1

Introduction

Mobile robots are often proposed as a favorable substitute to human correspondence in many real-world situations. Whether surveying remote (potentially hazardous) environments - such as in space and deep-sea exploration, or performing menial tasks - such as vacuuming and cleaning, a robot's capabilities should reflect the demands associated with its end-use application. Untethered mechatronic systems such as mobile robots are usually equipped with some computational resources, sensing capabilities, wireless radios for communication, energy source, and form of mobility. These devices however can remain active and prove useful, until their finite energy diminishes.

There are many complex energy conversions onboard a mobile robot. For example a battery's electrochemical potential energy is transformed to electrical energy. Electrical energy can be further converted to mechanical kinetic energy via an electromagnetic motor, with dissipative thermal losses as a byproduct of all conversions. Usually electrical energy undergoes several more conversions, since all circuits in a mobile robot rarely operates at the same voltage level; hence power converters and voltage regulators are often scattered throughout a mobile robot's electronics. Regardless the chosen method or topology in power conversion, even the newest, most efficient devices can be quite inefficient throughout a given operating range. On the other hand, electromechanical devices, such as servos and motors, are sometimes run at efficiencies around 60% - even less if drive trains with high gear-reduction ratios are employed. It becomes evident that such losses must be accounted for when developing strategies to effectively appropriate system resources.

Given a robot's available energy and a set of operating conditions, we might choose to maximize operating time, a specific device's power consumption, overall battery life, the distance driven, area covered, number of measurements taken by sensors, and so many others. This will define whether to design around increasing energy efficiency, versus power, total run-time, or *task* efficiency.

1.1 Motivation

The task selected to investigate, is a robot's ability to effectuate mobility. This thesis exposes how various embedded devices within a mobile robot contribute to the reduction of its battery's available energy. The goal is to shed some light on how to design more efficient embedded systems.

Some key points in this thesis, when combined, distinguish this work from others in the literature. First, the concepts discussed cover a wide range of disciplines, taking into account many dynamic variables that usually go unmentioned in other work. Second, such a detailed analysis has not been published for a small mobile robot, nor have been designed into several custom (and even a commercial) platforms. Third, is the integration of an *on-system* fuel-gauge used in a *system-side* configuration (these terms are defined in Appendix B).

In addition, there are a few reocurring themes - in terms of design and analysis of a mobile robot's power systems. The first and most important is to design around end-user safety. Another focus is on designing a flexible system, in terms of scalability. Scalable designs are preferred in embedded systems, since the framework developed for one platform can be applied to another - requiring minimal modifications or customizations.

With this in mind, a versatile fuel-gauging chipset was incorporated into three small custom PCB designs. These devices provide a scalable and safe means to integrating Li-ion battery technologies across four custom miniature mobile robots as well as one commercial system. Measurements logged by the fuel-gauge can in turn aid with evaluating a robot's performance by characterizing various in-system dynamics, and can even serve to enhance simulations in the work of [6] that inspired this thesis.

1.2 Thesis Organization

A closed-form expression describing the kaleidoscope of interdependencies governing a robot's energy dynamics can never be exactly determined. Mobile robots are inherently dissipative, otherwise known as *open*, thermodynamic systems. Energy transfer from source to load is never 100% efficient, and almost every variable is time-varying and temperature dependent. So obtaining an explicit, closed-form expression detailing every factor and its contribution(s) to energy dynamics, is not only highly unrealistic but impractical and computationally inefficient.

Following a divide and conquor approach, electrical systems onboard a mobile robot are divided in two categories: its source, and load. The chapters that follow cover a broad range of concepts - some in more detail than others. For brevity and clarity, detailed discussions about designs and experimental platforms will be deferred to the appendices. Material is organized in the following manner:

- Chapter 2 outlines related work associated with monitoring battery dynamics, applications in robotics, and also in teams of mobile robots.
- Chapter 3 describes the features of interest when profiling a robot's source dynamics, specifically during discharge conditions.
- Chapter 4 provides the details in modeling various electrical components often used in embedded robotic systems.
- Chapter 5 discusses the mechanical energies associated with displacing a robot, particularly a two-wheeled differentially driven mobile robot with a balancing caster-arm.
- Chapter 6 presents a practial, and moreover simple, means to track battery dynamics using an embed hardware fuel-gauge chipset integrated onboard three different custom PCBs. Upon introducing these designs, this chapter also shows their application in experimental mobile robotic platforms - which are further detailed in Appendix B.
- Chapter 7 offers some concluding remarks regarding topics presented in this thesis, as well as some future directives to expand on this work.

Chapter 2

Related Work in Literature

Embedding power-aware characteristics in mobile systems, is a widely studied inter-disciplinary topic investigated on many levels. In this work it begins with a system's ability to maintain an active profile of its remaining energy. This can be accomplished in many ways, as there exist several stategies to monitor and predict a battery's dynamics. These topics have been applied to a plethora of work in the fields that comprising mobile robotics, as well as extensions applicable to multi-robot teams. In the sections below, many such methods and algorithms are discussed, and some of the more relevant literature will be compared to the topics presented in this thesis.

2.1 Battery Models

The choice in battery chemistry should undoubtably reflect the system's overall demands and end-use application. Lead-acid batteries and fuel cells are usually not employed in light-weight mobile systems, as they are generally large and heavy. Similarly NiMH batterys are not used in devices that see everyday use and frequent partial (dis)charge cycling - since they suffer from the *memory effect*. Most portable consumer electronics, ranging from cell phones to digital multi-media players, use Li-ion cell chemistries as a secondary battery source. Their low self-discharge rate, long cycle life, high energy density, and rapid charge capability are just a few of the many advantages which make these batteries a favorable alternative to other battery chemistries, such as NiCd, NiMH, and alkaline [7].

Li-ion polymer (LiP or LiPo, used synonymously) battery chemistries in particular have a much higher power-to-weight ratio. They can be manufactured in a thin, light-weight, flexible casing, making this battery type an appealing substitute to other Li-ion chemistries. Factoring in commercial availability and cost, LiP batteries (LiPBs for short) proved the best, most reliable choice for a power solution in a miniature mobile robot. Hence the specific Li-ion cell chemistry of focus in this thesis will be LiP, which was used in all systems designed as well as battery

experiments performed (specific details can be found in Appendix B).

These favorable attributes however come at a price. One of the primary drawbacks to using Li-ion batteries is that they require close monitoring to ensure safe operation. The consequences of over-charging or exposure to high temperatures are (at the very least) performance reduction, materials degradation, and may even compromise user safety - by increasing the risk of cell venting and combustion. Figure 2.1 shows a normal LiPB cell (on the right) compared to the same cell that has gone bad (on the left).

Figure 2.1: *Left*: Front and back sides of two bad (swollen) LiPB cells. *Right*: A normal cell of the same type.

Although the cells depicted here are almost a decade old, the two on the left have been left over-discharged for an extended period of time (years). Their swelling is likely a result of the cell's seperator starting to degrade and/or the electrolyte starting to breakdown. If the internal pressure generated from this chemical reaction eventually ruptures the cell's aluminum casing, the electrolyte and lithium (salt) solvent would be exposed to the air's oxygen. The resulting chemical reaction can be quite violent, as the solvent quickly ignites and burst into flames. So secondary Li-ion cells require protective circuitry to ensure safe operating conditions.

Monitoring the physical dynamics of Li-ion based power sources (of which LiPBs are a subset) can be done in many ways. Generally they are grouped into four broad categories: physical, empirical, abstract, and mixed models.

Physical models are the slowest to provide estimates, most difficult to (re)configure, but can be the most accurate. They require knowledge of battery structure, chemical composition, temperature, capacity, and many others, just to set up the model's system of interdependent partial differential equations - not to mention the difficulties involved in solving these equations [8]. So, although such a deterministic method for predicting battery dynamics may be highly

accurate, it lacks algorithmic scalability (that is, the ability to easily reapply formulated framework to many other systems). In addition, solving the complex mathematical equations can be strenuous on a processor, which might even increase the system's overall power consumption.

The empirical model in [9] computes battery efficiency of multi-battery systems through the usage of interleaved power supply and load splitting. Other models use Weibull fitting [10] in addition to simple empirical measurements. The main drawback to empirical models are the tedious experimental setups, requiring recalibration at each temperature measured in order to create a database profile of the battery's characteristics and temperature dependence. Though not too accurate, the main benefit in this approach is the low computational complexity involved in execution, only requiring the specification of two or three parameters.

Frequently referred to as book-keeping methods for tracking LiB dynamics in the literature, these techniques store discrete battery (chemistry-specific) parameters in a local table. Such variables can in turn be measured during active use (whether discharging or charging) compared to those tabulated, and in turn corrected - as needed. The battery's capacity is usually tracked by some sort of Coulomb-counting algorithm, which counts the incremental amount of charge entering or exiting the battery.

Abstract models are known to be fairly accurate as well. In [11], capacity is estimated via a discrete-time stochastic prediction model. Electrical circuit models discussed in [12] and [13] attempt to model the entire system in terms of passive circuit elements. Equivalent circuit models offer a means to couple empirical observations of internal electrochemical processes with electrical analogies. These models range in complexity from approximating a battery's internal impedance as a single real-valued resistance, to detailed distributed-parameter circuit networks which model spatio-temporal effects. Lying somewhere in between (in terms of complexity) are a variety of lumped-parameter circuits that use a small number of passive elements to model cell dynamics, such as the Randles equivalent circuit (see Figure C.2 in Appendix C.1.1).

The analytical-based prediction algorithm discussed in [9] models cell aging (or degradation) phenomenon observed in Li-ion cells in terms of their chemical structure and its decomposition. One of the key results in [9] is the definition of a battery's state of health (abbreviated SoH) to visualize the effects of capacity fading. Employed repeatedly throughout the parameterization of Li-ion batteries within this model are physical principles governed by the Arrhenius temperature dependence of conductivity and reaction rate [14], [7]. The promising results obtained by the analytic method in [9] give a best-case error of 3.5% [15]. One of the main drawbacks observed in this model is its lack of scalability, requiring over fifteen parameters to configure the system. Furthermore, the methods of [9] differ from the approach presented in this thesis, since it does not capture the relaxation phenomenon in Li-ion based batteries [16].

An important detail worth mentioning is that relevant works in the literature are usually not applied to mobile robots, but instead hybrid-electric vehicles (HEVs). As such, these batteries are noted to operated between 95%–5% or even down to only 10% of their capacity limits, so the

full range of battery charge is often not included models [17] However for a small, light-weight mobile robot, the last few percentages of charge could determine the success or failure of its goal.

The approach considered in this thesis, in which model battery dynamics are modeled, bears slight resemblance to the methods presented in [18] and [19]. These works do not rely primarily on the internal chemical dynamics of a battery cell, but instead utilize the relaxation effects observed at its terminal voltage following a measureable disturbance in current pulse. These features will be discussed in subsequent chapters.

A mobile robot's battery is rarely discharged at a constant rate during an entire cycle. Most of the time, this rate will vary as processing demands change, and sensors or actuators are utilized. So there may be brief times where power consumption peaks, and others when the discharge rate plateaus to an arguably negligible value. Considering such stepped variations occur during normal operation, we can utilize this information as a relaxation period to infer the loaded internal DC resistance of the battery.

Almost all the robots described in this thesis are designed and built in the guise of prototypes. They are intended to operate in relatively structured indoor environments, and will be used by university researchers - primarily graduate students. For this reason it is fair to assume that the systems will not be used continuously; that is, for extended periods of time. Such robots are usually turned off after use, and could remain off for variable amounts of time - whether one night, a week, or even shelved for months. Exposing this seemingly subtle piece of information about how robots will be used, can be exploited to robustify robot designs.

2.2 Power Management in Mobile Robotics

The work in [20] provides an overview of the overall goals outlining power-aware systems and techniques in achieving these results. The energy-aware algorithm, *Autopower*, introduced in [21], is a model characterizing an autonomous distributed team of robots in terms of their software systems' computation and communication energy behaviors. In this manner, various decision can be made in regards to where the robots should move, and also how the robots should interact. However the model proposed does not take into account power source dynamics in the various behaviors considered. That is, there is no explicit model of a battery, and finally robot sensing or motion behaviors are not considered when adjusting robot software systems' energy behavior.

In [22], the authors presents a similar concept of mapping energy usage to an application process in software, while still considering hardware factors contributing to the overall energy demands. Using this information the authors propose a power management policy model to meet a given objective, which is implemented in a Linux kernel.

The focus in [23] is in motion planning, and neglects the power-consumption in the processor

and communication electronics, which can sometimes overshadow the effects of motors. In [24] the model and subsequent formulations are based on the claims that the power consumed by the DC motors accounts for over 70% of the overall power supplied. While some systems do indeed exhibit majority power dissipation across their drive motors, others may experience higher losses elsewhere. Miniature robots (such as the one considered here) often utilize miniature and sub-miniature DC motors (often referred to as DC micro-motors), and contribute only a small fraction to the overall system's power consumption. In such small robots, single-board computers (SBCs) and multi-core embedded processors are examples of active peripherals whose active power consumption can vastly reduce operating time if not accounted for in the dynamic models considered.

An optimal, analytic minimum-energy velocity controller is introduced in [25]. Emphasis is on minimizing energy consumption in a two-wheeled mobile robot (TWMR) through trajectory planning and generation, resulting in 10% battery energy savings. Similarly, the focus in [23] is in motion planning, neglecting the power consumption in other active onboard electronics.

A control strategy to minimize power consumption in a wheeled mobile robot (WMR) is described in [26]. The authors introduce the notion of *joint speed control and power scheduling* by controlling both the robot's traveling speed and its onboard processor frequency simultaneously. This strategy however, does not describe the power consumed by sensors, voltage regulators and/or power converters, wireless radio devices, or other peripherals utilized during exploration.

Besides the mathematical simplifications that arise, the structure of TWMRs can facilitate impact invariant designs, such as in [4] and the considerations outlined in [27]. Unless actively controlled to maintain balance (similar to the classic inverted pendulum problem), TWMRs require a stabilizing caster arm in order to constrain their kinematics and avoid spinning in place about their wheel-axle's normal axis (the axis along the wheel-base). Use of a caster will generally reduce the overall power consumption in both motors. Otherwise an additional (torque) control loop must be added to the motor controller algorithm in order to maintain balance and stabilize the robot's shifting center of gravity. Depending on the stabilizing caster arm's placement, orientation, material properties (such as ductility, flexibility and compliance), and whether it is dynamic (actuated) or passive (fixed), static power draw from the robot's power supply will vary significantly. Additionally the robot's rotational inertia may change for varying caster placement and orientation, which are contributing factors to its resultant kinetic energy. Quite often however, such effects and their impact on the system's dynamics go unmentioned in the literature, as kinematic trajectory synthesis and control of translational dynamics overwhelm energy-driven discussions in robotics analysis.

2.3 Energy-Awareness in Teams of Mobile Robots

In addition to estimating remaining power, the system must encompass the ability to apply these estimates to the task(s) of interest. Consider the scenario where a docking-station is introduced as a means to enable recharging of the robots in remote environments. In this application the importance outlining the question of "what can the robot accomplish" arises, and the subsequent similar question of "how long can the robot run for," given its remaining energy level. This information defines the inherent trade-off(s) between the energy expended (cost) to perform a given task (consequence).

The design of a robotic team can be built around maximizing the longevity of the overall team in missions with unpredictable duration. To achieve this, the deployed systems must be capable of refueling if and when the need arises. Energy might be extracted from the environments - by employing passive or active energy harvesting techniques; each another - that is, other members within the team; or a seperate recharging station - which can be stationary or mobile. Each of these methods can be realized in a number of ways.

In [28, 29], and [30], robots are deployed in fixed environments and navigate to predetermined recharging points. In controlled, known environments, such as laboratories and manufacturing centers, this approach works well. Known landmarks in the environment can be used to correct for errors in odometry and these robots can continuously operate. However, in scenarios where these types of systems would likely be used, it is unlikely that the environment would be known *a priori* and that recharge points would be appropriately staged or even functional.

The method chosen to transport and deploy mobile robots in a given environment, can be accomplished in many ways. In [31], a larger four-wheeled commercial ranger robot is chosen to transport (up to ten) as well as deploy a team of two-wheeled robotic scouts by using a launcher mechanism affixed to its top. To facilitate robot deployment, while ensuring minimal modifications are required, the scout robots are encased in a custom, ruggedized shell to withstand ground impacts as they reach an area of interest.

In [32], a simulated robot acts as a tanker which traverses an environment to seek out robots in need of refueling. This system resembles an aerial tanker during an in-flight refuel - able to only service a single robotic system at one time. An interesting, though atypical, alternative to recharging is proposed in [33], where the robots in the team can physically exchange batteries. This system is exceptional with respect to the rate of energy transfer between team members, though it requires a high degree of precision to be successful.

Every approach discussed relies on utilizing accurate estimations of the available energy to the deployable systems. This work attempts to address the issues by providing accurate solution to measuring critical battery parameters on a small custom robot, considering such end-use applications. To promote such efficiency in such mobile robotic teams, the same solution implemented in the design of the robots is implemented into the mobile docking and recharging

station (MDS) described in [34]. The result is a versitile fuel-gauging circuit design, and its realization on a custom PCB, thus adding a layer of intelligence to the MDS system by enabling a straightforward easy-to-use method to determine how many robots the MDS can service.

Chapter 3

Battery Source Dynamics

As mentioned previously, a mobile robot's electical system can be divided in two categories: its source and load, where each component and its influence on energy dynamics can be modeled with arbitrary complexity. Focusing first on the system's source dynamics (load dynamics will be discussed later), this work concentrates on the battery during discharge conditions.

3.1 Li-ion Battery Modeling

Consider a battery with remaining energy $E_{rem}(t_n)$, at time t_n. The rate of energy reduction during discharging is given by the battery's discharge power P_{dsg}; which, by definition, is $P_{dsg} = V_{bat} \cdot I_{dsg}$, where V_{bat} and I_{dsg} represent battery voltage and discharge current, respectively. If the battery is discharged at P_{dsg} over a time interval $\Delta t = t_n - t_{n-1}$, the energy *removed* (hence the negative sign) is $-\Delta E_{rem} = E_{rem}(t_n) - E_{rem}(t_{n-1})$. Knowing that $-\Delta E_{rem} = P_{dsg} \cdot \Delta t$, then the present energy level $E_{rem}(t_n)$ can be written as in Equation 3.1.

$$E_{rem}(t_n) = E_{rem}(t_{n-1}) - \underbrace{V_{bat}(t_n) \cdot I_{dsg}(t_n)}_{P_{dsg}} \cdot \Delta t \tag{3.1}$$

Continuing to discharge the battery at a rate of P_{dsg}, when present energy level is $E_{rem}(t_n)$, the system's remaining time until empty (t_{RTE}) is given in Equation 3.2 below [35]. This is a direct result of applying Equation 3.1 with $\Delta t = t_{RTE}$.

$$t_{RTE} = \frac{\Delta E_{rem}}{P_{dsg}} \tag{3.2}$$

The battery's voltage (V_{bat}) is defined here as the system's source voltage. This refers to the *loaded* voltage, measured during active use - whether (dis)charging. The *open-circuit* voltage V_{oc}, often called OCV in some literature, is defined as the battery's measured voltage under

no-load conditions. It is not synonymous with battery *electromotive force* (EMF) voltage. In contrast, the EMF voltage, abbreviated V_{emf}, describes the observed open-circuit potential when all cells within the battery pack are in a fully relaxed (equilibrium) state.

Here the term *relaxed* suggests that all cells within the pack have been given adequate time to rest after being perturbed during (dis)charge. Mathematically, this is the limit of $V_{bat}|_{I_{dsg}=0}$ (or equivalently V_{oc}), as both time t and cell temperature T_K (in kelvin), approach relaxation time t_{rlx} and equilibrium temperature $\overline{T}_K$, respectively. If during t_{rlx} there are no external temperature disturbances or anomales, this limit can be written with respect to t_{rlx} alone - since $\overline{T}_K$ will follow after t_{rlx} has elapsed. Equation 3.3 summarizes this statement mathematically.

$$V_{emf}\left(Q_{rem}, \overline{T}_K, t_{rlx}\right) = \lim_{t \to t_{rlx}} V_{oc}(Q_{rem}, \underbrace{\dot{Q}_{rem}}_{I_{dsg}}, T_K, t)\Big|_{\dot{Q}_{rem}=0} \tag{3.3}$$

Notice V_{emf} is a function of three variables, whereas V_{oc} and V_{bat} also depend on the rate at which remaining charge Q_{rem} is being reduced. In other words, Q_{rem} only correlates with battery voltage when all cells within the pack are fully relaxed. Most of the time, remaining charge is given as a percentage, with respect to the battery's full charge capacity (Q_{fcc}). This is known as the state of charge (SoC), and is defined as SoC $= Q_{rem}/Q_{fcc}$. Often a distinction is made between relative and absolute state of charge (RSoC and ASoC, respectively), where the latter is defined with respect to the battery's maximum chemical charge Q_{max}, which will decrease with use (discussed shortly). Notice that RSoC $\geq$ ASoC initially (that is, for a new battery), and becomes a strict inequality after primary use.

During discharging or charging, the sum of all voltage drops within a battery, consequent to the flow of electrical current, is often referred to as the battery's *overpotential* (V_η). More details can be found in Appendix C.1.1. Depending on the present operating conditions, contributions from each overpotential to total V_η can be weighted. Operating conditions are defined by the present I_{dsg}, ambient temperature $T_{amb,K}$, and SoC. For example, we know that $V_{\eta,dif}$ is attributed to the increased rate of energy reduction as the battery approaches empty [36]. Often overpotentials are ascribed an equivalent impedance, based on a cell's response to external stimuli. This facilitates coupling empirical observations associated with charge-transfer processes, to electrical circuit analogies.

A LiPB's frequency response actually exhibits similar characteristics to a capacitor with very large ($R{\cdot}C$) time-constant [37], where R represents an equivalent series resistance (ESR). Hence long relaxation times (t_{rlx}) are alotted to find the time-constant(s) associated with $R{\cdot}C$ value(s) [38]. Figure 3.1 is a generic plot of a Li-ion battery's impedance spectra, showing the associated kinetic steps in electrochemical charge-transfer. These charge-transfer steps are often assigned time constants time in terms of the battery's voltage response [39].

Here the complex plane is drawn slightly modified, since the imaginary axis is backwards.

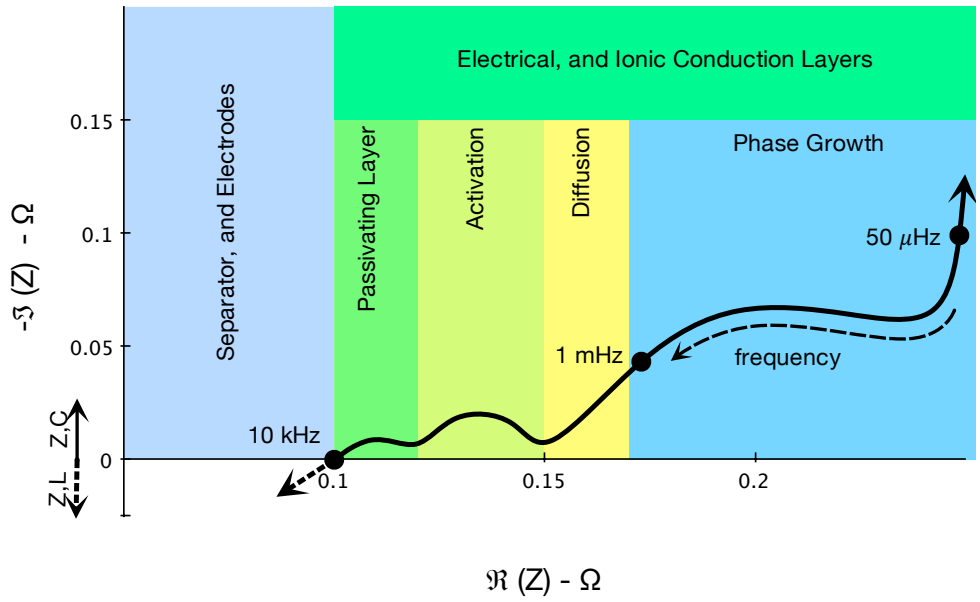

Figure 3.1: Generalization of a LiPB's complex impedance ($Z = R - j{\cdot}X$) spectrum on a modified Nyquist plot - where the horizontal and vertical axes represent the real and imaginary axes, respectively, with frequency increasing from right to left - as indicated by the arrow.

So a negative reactance (denoting a capacitive impedance, Z_C) points upward, while positive reactance (representing an inductive impedance, Z_L) points downward, as indicated at the bottom-left corner of the graph. In this modified form, the Nyquist plot is often referred to as a Cole-Cole plot. It should be noted that the electrical and ionic conduction layers bin sizes in this figure are not drawn to exact scale, and so does not imply anything about the spacing and distribution of frequency points indicated. In fact, the downward pointing arrow at the Z_C-Z_L cross-over point should be much steeper. However the lower frequency range is of most interest in the type of mobile robots considered here.

Figure 3.2 plots the measured the impedance magnitude ($|Z_c|$) versus DoD for each of two cells within a $2_{\mathrm{S}}1_{\mathrm{P}}$ configured LiPB. In terms of percentages, the battery's depth of discharge is defined as DoD $= 100-$ SoC. The left graph illustrates $|Z_{c,x}|$ after the first cycle, and the right $|Z_{c,x}|$ after the second cycle, for $x = \{0, 1\}$ (with the more positive cell within the pack being $x = 1$).

This particular battery pack's individual cells are actually suprisingly well matched. Their impedances are almost identical throughout most of the DoD levels during discharge. Larger inter-cell $|Z_c|$ variations are observed as EoD voltage (V_{EoD}) is approached. So far we have seen that Z_c depends on the applied stimulus frequency f_{stm} and battery SoC; it also depends on temperature, cell age, and the number of cycles accumulated.

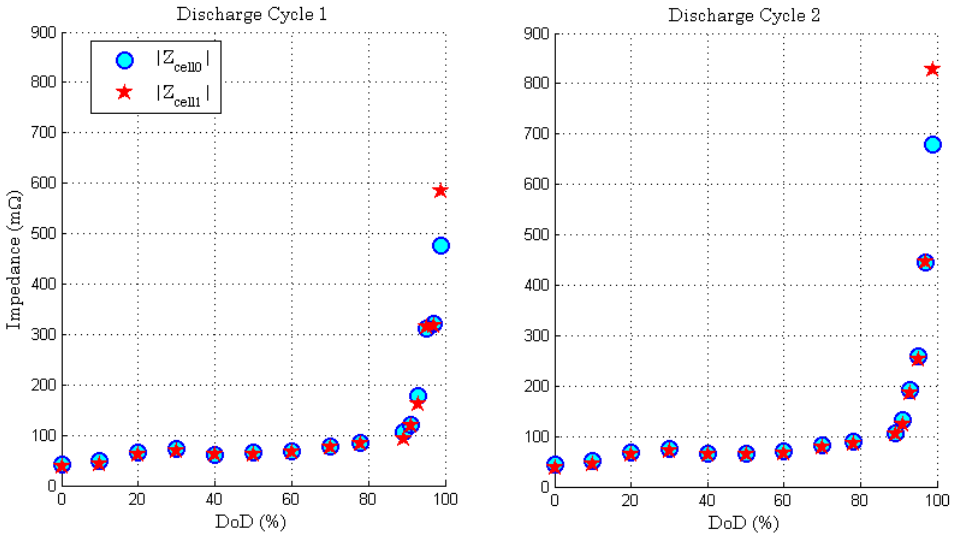

Figure 3.2: Modulus of each cell's impedance, $|Z_{c,x}|$, for $x = \{0, 1\}$, versus DoD, during two consecutive full discharge cycles.

One *full* cycle is defined as a full discharge (charge) cycle followed by a full charge (discharge) cycle, in either order (respectively). Letting N_{cc} represent the number of cycles experienced by the battery, also known as the *cycle-count*, the performance metric here is measured by graphing Q_{fcc} versus N_{cc} and noting the slope of this curve. Such a graph is usually included by the manufacturer in the cell's datasheet, as illustrated in the bottom graph of Figure 3.3. Here, Q_{max} is the battery cell's theoretical maximum chemical capacity (for a new, fresh cell), and N_{cx} is the transition point where the reduction rate of full-charge capacity ΔQ_{fcc} changes.

Noting the linearity in this graph, the we can actually approximate the relationship between cell cycle number and discharge capacity using a piecewise continuous function, comprising two linear segments. Of course, adding several more line segments could increase precision, but for our purposes the accuracy attained in using two suffices. This approximation is shown in the zoomed-in graphic (on the top portion) of Figure 3.3. Using the figure's data, this piecewise function can be written as Equation 3.4, where variable N represents the cycle count number N_{cc}.

$$Q_{fcc}(N) = \begin{cases} Q_{max} - m_1 \cdot N, & \text{if } |N| \leq N_{cx} \\ Q_{max} - m_1 \cdot N_{cx} - m_2 \cdot N, & \text{if } N > N_{cx} \end{cases} \tag{3.4}$$

The above only considers Q_{fcc} reduction from active use, however Li-ion batteries are known to lose charge over time, even when no load is attached and cells have remained inactive for an

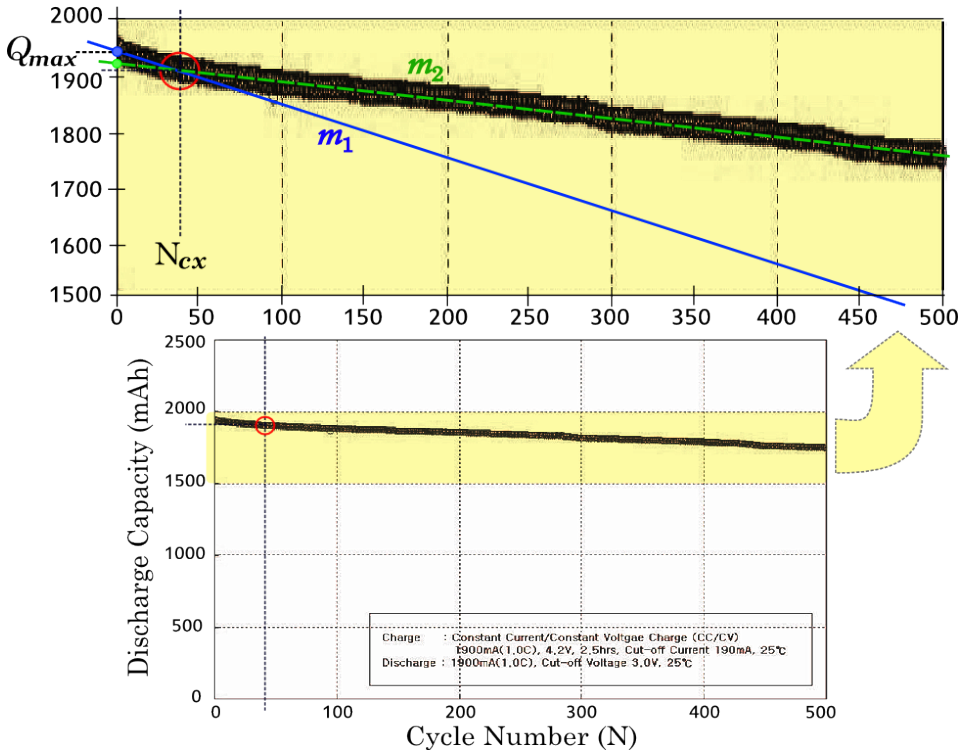

Figure 3.3: Cell cycle number versus discharge capacity (in mAh). The bottom graph is to original scale (reproduced from the cell manufacturer's specifications in [2]), and slightly modified to highlight the particular area of interest. The top graph is enlarged and zoomed-in to show detail.

extended time. This occurs as a result of discharge reaction(s) that proceed, albeit to a limited extent, thoughout the battery's lifetime. Considering the LiPB cells used here, an average SoC reduction of 3% per month (or less), is a reasonably safe assumption [40], [7], [41]. To assign a more quantitative number to this value, for 1900 mAh cells, this corresponds to a capacity reduction of $\Delta Q_{fcc} = 57$ mAh.

Clearly, from a systems viewpoint, a LiPB's dynamics are indeed non-linear and time-dependent. The effects from cell aging along with present and past (dis)charge trends govern a cell's present capabilities. As a result, this system is *not* shift-invariant in time. In this light, a distinction is made between three main time scales to simplify subsequent analysis.

- Large time intervals, from days to even years, cell aging and previous cycle trends must be considering when describing its present capabilities.
- Very small time scales, in the sub-second range, transient behavior (during both loaded and unloaded conditions) must be included in a model to accurately describe the system's

dynamics.

- For medium, or *relatively* small times (ranging from minutes to a few hours), when performing a full discharge cycle in this operating region a battery's dynamic behavior can be approximated as a linear and time shift-invariant (LTI) process.

Since the maximum chemical capacity reduction can be included in a model, as described above, large time intervals can be compensated for - to some degree. Very small time scales, corresponding to high frequency pulsed-load discharging, is observed more in mobile phones. This is not so much characteristic to mobile robots. If anything, a mobile robot's load profile exhibits more a constant, or in general a stepped constant, discharge profile. In addition, since their loads usually have many load devices with relatively large input capacitances (like DC/DC power converters and voltage regulators) a lot of the high frequency ripple in current and voltage will invariably be smoothed out. Usually ceramic capacitors are paralleled with polarized tantalum or electrolytic capacitors (of low-ESR type), which can amount to a bulk capacitance anywhere from tens to hundreds of μF, or greater.

It seems a mute point to characterize a battery's performance using high frequency pulsed-load stimuli when in actuality the battery is discharged at a much lower frequency during in-system use. Hence the last time scale listed above will be the focus here, as it actually fits the operating profile of most mobile robotic systems. Imposing this simplifying assumption will vastly reduce complexity in model formulation (and its solution). Often the problem of tracking source dynamics can be reduced to solving a series of parametric equations describing line/load variations.

3.2 Tracking Battery Dynamics

Figure 3.4 illustrates a $3_{\mathrm{S}}1_{\mathrm{P}}$ LiPB pack's V_{bat} versus SoC profile, measured during a C/2 constant-current (CC) discharge cycle, followed by a long rest period. This rest period begins when discharging is terminated, and ends when each cell's measured voltage hysteresis is less than a chosen threshold v_{hys} - usually on the order of a few (to tens of) μV. In this figure, the red square marker indicates the point at which the voltage fluctuation measured across every cell are less than $v_{hys} = 4\mu$V per second.

There is no particular reason for choosing 6μV over 7μV, or even 20μV for that matter, it is just a very small valued threshold that is used to quantify when equilibrium is (approximately) reached. This cell chemistry-specific parameter is also chosen to account for additional (albeit small) loading effects by the fuel-gauge ICs, when sleep-mode of operation is entered, during measurements. Allotting large values of t_{rlx} enables a fuel-gauge circuit to recalculate, recalibrate, and finally stabilize to a steady-state voltage (after this relaxation time has elapsed)

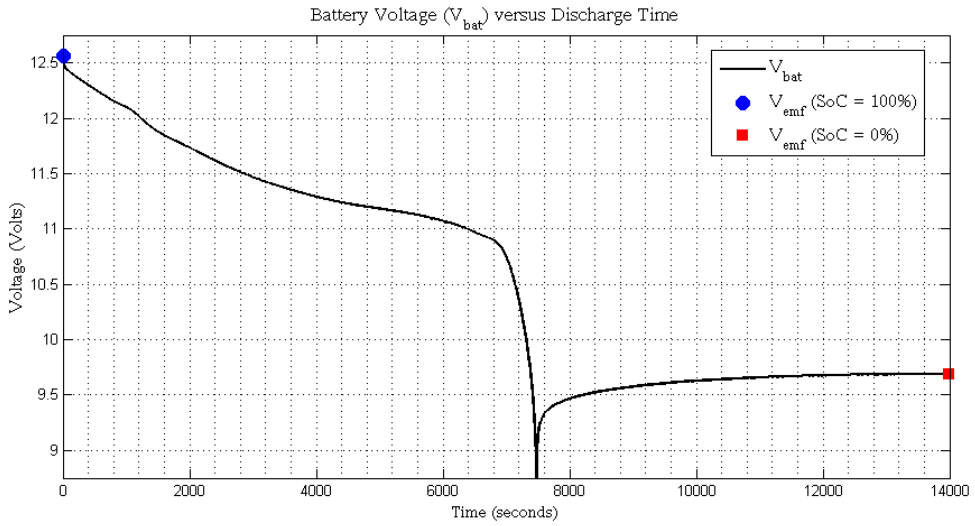

Figure 3.4: Measured V_{bat} versus time (of a 3_S1_P configured 1320 mAh LiPB pack) during a C/2 constant-current full discharge cycle, followed by a long rest period. The end-point markers represent V_{emf} measured at SoC = 100% and 0%.

to obtain better measurement of V_{oc}, since longer t_{rlx} times will result in a higher correlation between V_{oc} and the theoretical chemistry-dependent V_{emf}.

Figure 3.5 graphs a 2_S1_P LiPB's measured V_{bat} versus DoD, for five different discharge cycles. Here rates are given with respect to E_{fcc}, or E-rates for short (see appendix D about this nomenclature). Expressing discharge rate in terms of energy E, rather than capacity (or C-rates) which is commonly used, is preferred since the battery's equivalent load exhibits constant-power discharge characteristics (which will be discussed later, in Chapter 6).

The three continuous curves represent data collected during 1·E, E/20, and E/50 discharge rate cycles. Two additional 1·E cycles were performed, during which discharging was paused and the battery was allowed to relax for 5 minutes (one test) and 15 minutes (the other cycle test) as various prespecified DoD levels were reached. In Figure 3.5 the discrete points indicate the measured V_{oc} at the very end of each relaxation interval, induced at the indicated DoD level. Similarly, V_{oc} data tabulated during E/2 and E/5 discharge rates are shown at the end of 15 minute relaxation intervals, for various DoD levels.

With the exception of the last few percentages SoC, notice how close together almost every tabulated V_{oc} point is. In fact, every measured V_{oc} at SoC = 100% and EoD should be exactly equal, since after discharging was halted, when DoD = 100% was reached, all batteries were given sufficient time (several hours) to fully equilibriate after EoD is reached. The two points sitting just below the battery's observed V_{emf} (around 200mV or so) were a consequence of over-discharging (well below 3.0V per cell) during those cycle tests.

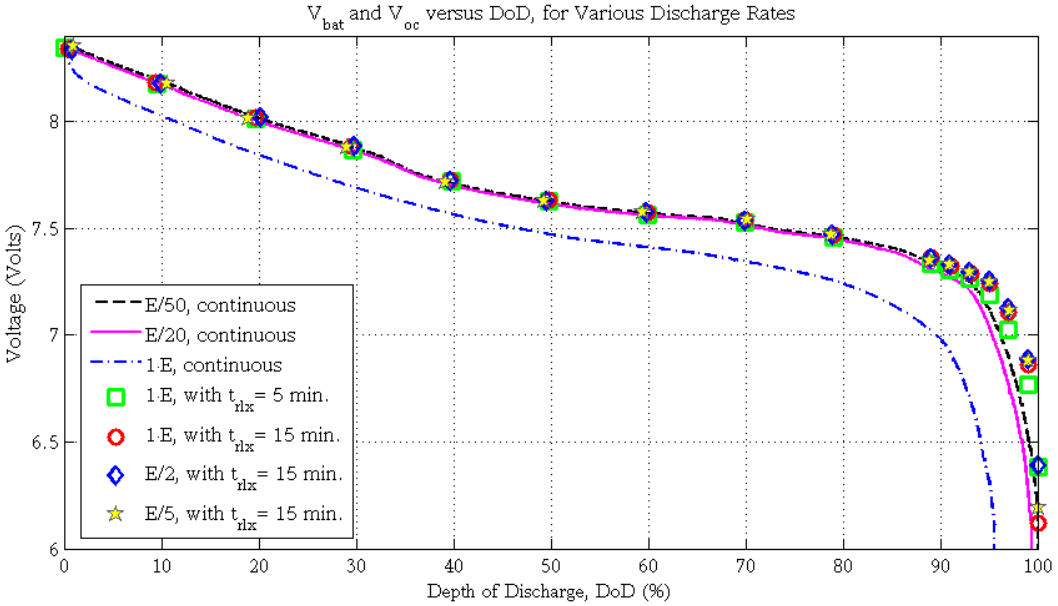

Figure 3.5: Measured battery DoD versus V_{bat} (continuous discharge curves) and V_{oc} (discrete points) for various discharge rates and t_{rlx}.

Arguably the most important feature in Figure 3.5 is how closely each V_{oc} measured after $t_{rlx} = 15$ minutes follows V_{bat} during E/20 and E/50 cycle tests. This trend remains valid from E_{fcc} to around 15% SoC, after which the measured V_{oc} after both t_{rlx} times start to deviate from V_{bat}. Even for E/20 and E/50 low discharge rates, measured errors become progressively larger as EoD is approached. In this region however, V_{oc} measured after $t_{rlx} = 5$ minutes starts to better match both E/20 and E/50 discharge curves. Another noteworthy observation is the seemingly premature EoD termination in the 1·E continuous discharge cycle. This actually highlights the difference between the battery's full-charge energy E_{fcc}, and that of usable energy E_{use}.

Because we are charting different rest times t_{rlx} for dissimilar discharge rates, there needs to be common ground for data comparison. To assist with visualizing how t_{rlx} influences V_{oc} approaching V_{emf} for variable discharging conditions, we introduce the notion of a *relaxation time constant* ($\tau_{t,rlx}$). It is defined here as the time it takes for V_{oc} to reach 63% of its final value during relaxation. Figure 3.6 plots the measured $\tau_{t,rlx}$ for different t_{rlx} and E_{dsg} rates.

End values of V_{oc} measured after t_{rlx} discharge pauses are used to define a piecewise continuous function that serves an estimate to V_{emf} - represented by $\hat{V}_{emf}$. Figure 3.7 illustrates this function, found by linearly interpolating V_{oc} using data collected after $t_{rlx} = 15$ minutes at given DoD levels, during a E/2 discharge cycle. Note, the E/5 discharge cycle performed with $t_{rlx} = 15$ minutes would probably serve a better candidate for V_{emf} estimation via interpolation.

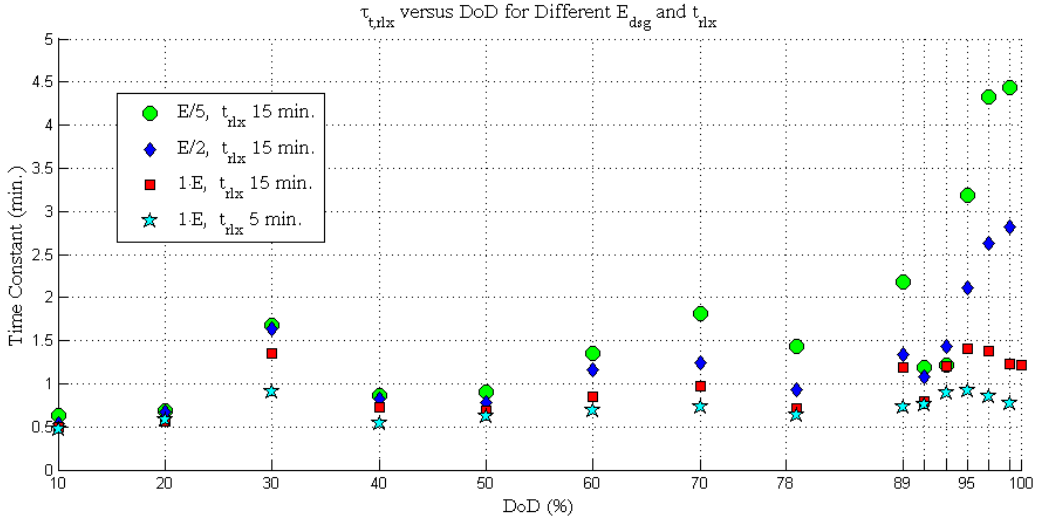

Figure 3.6: Measured relaxation time-constant ($\tau_{t,rlx}$), for different t_{rlx} times and E_{dsg} rates, using a 2_S1_P LiPB comprising 1900 mAh (nominal) capacity cells.

However, the battery was overdischarged (well beyond V_{EoD}) when DoD reached 100%; hence the E/2 cycle with $t_{rlx} = 15$ minutes was the next best choice.

This may not yield the most accurate results, especially nearing EoD, but it does however provide a fairly good estimate for a first attempt. It also exeplifies that V_{emf} can indeed be approximated by a linear relation. Using a different, more complex interpolant - such as a higher-order polynomial function, may give a better estimate to V_{emf}. Although, it was interesting to observe that cubic spline interpolation resulted in a worst estimate than linear interpolation.

Furthermore, $\hat{V}_{emf}$ data can be fit to an exponential or logarithmic funtion, using continuous voltage measurements taken during prescribed relaxation intervals can facilitate simulating stepped load discharge dynamics. As an example, consider an CPU changing between various operating modes - from normal, to sleep mode, then idle, etc. In this case, it has been shown in [40] that by discarding the first 30 seconds of relaxation voltage data it is possible to converge to an V_{oc} that is within 1% of the cell's actual V_{emf}. In fact, the authors show that V_{emf} can be found after only 5 minutes t_{rlx}, again within 1% error.

The relaxation intervals introduced during discharge are in the fractional-Hz range, so still fitting the operating profile of a mobile robot during intermittent use - consider, for example, running a quick experiment with the robot for 20 minutes, then turning it off and setting it aside for a week. Figures 3.8 and 3.9 plot the discharge profile during a 1·E cycle, where $t_{rlx} = 5$ and $t_{rlx} = 15$ minutes have been introduced, respectively.

Such book-keeping methods track a LiB's dynamics by storing discrete SoC-V_{emf} values, specific to a cell's chemistry. Introducing relaxation times at various SoC levels during discharge

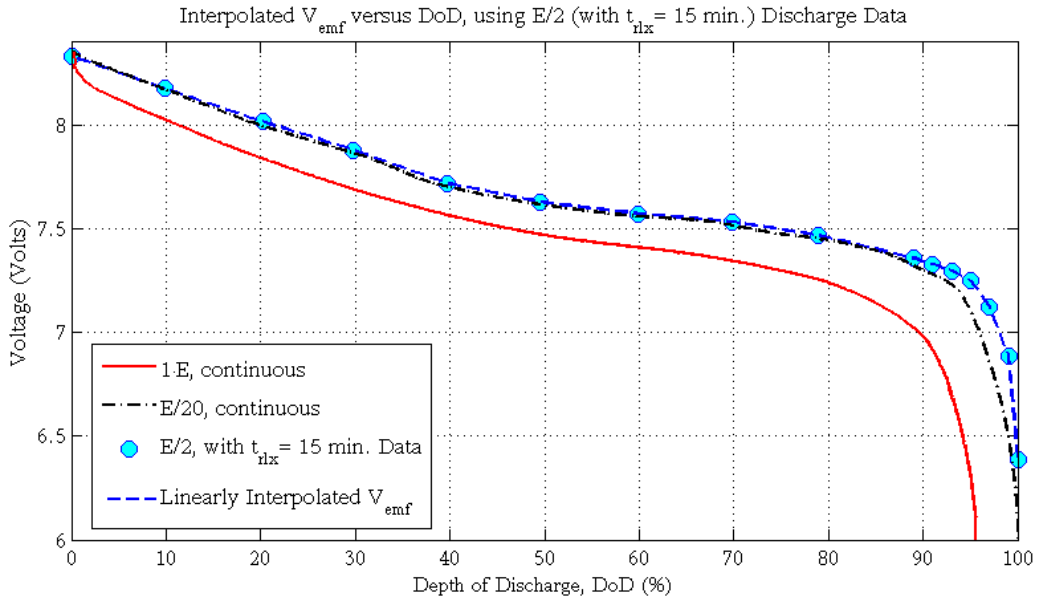

Figure 3.7: Linearly interpolated $\hat{V}_{emf}$, compared with V_{bat} measured during 1·E and E/20 discharge rates; plotted against DoD.

cycles allows fuel-gauging algorithms to start discharging from voltages that are closer to V_{emf}. Relaxation phenomena observed in Li-ion batteries are frequently used in tandem with other techniques, such as Coulomb-counting algorithms, to estimate cell dynamic parameters [16]. If discharging starts from a fully-relaxed state, Coulomb-counting can begin from a known, tabulated point. Since $V_{oc} = V_{emf}$ in fully-relaxed state (by definition), measurements can be compared with those charted in a look-up table, and even used to update Z_{bat} and E_{fcc} estimates throughout the battery's lifetime.

This is very similar to what a fuel-gauge chipset does. Figure 3.10 illustrates how internal resistance tables are updated during a C/2 discharge cycle, at different DoD grid-points, onboard a fuel-gauge chipset (described in further detail in Chapter 6).

In an effort to reduce the processing power demands of the load, it is favorable to embed monitoring functions in hardware. In this manner, estimating E_{rem} does not depend on higher-level software algorithms, nor does it infringe on the robot's finite computational resources. This also enables monitoring of cells during periods of inactivity when the robot is powered off, and the battery's internal dynamics give rise to degradation in performance due to long term capacity fading effects. Thus, to ensure end-user safety, and facilitate precision monitoring of each cell's dynamics, at *all* times, tracking a LiB's dynamics is best left to a dedicated hardware fuel-gauge.

Letting such a fuel-gauge IC take care of cumbersome calculations involved with estimating

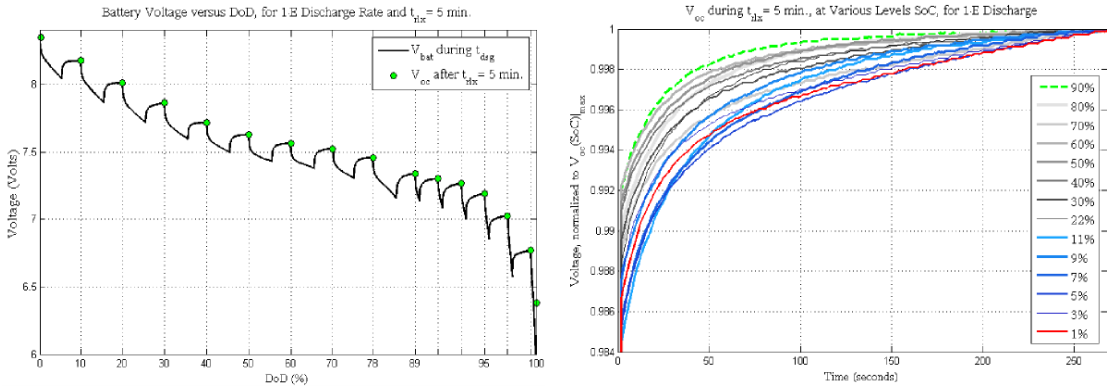

Figure 3.8: *Left*: V_{bat} measured during a 1·E discharge cycle with $t_{rlx} = 5$ minutes at various SoC levels. *Right*: V_{oc} during each t_{rlx} period, induced at the shown SoC levels. Note, each V_{oc} is normalized with respect to its maximum, end V_{oc} value.

E_{rem}, computing t_{RTE} boils down to simply measuring V_{bat} and I_{dsg} - both of which can be read back via the IC's TWI SMBus protocol. Another benefit from using such an embedded hardware solution is that, when idling in a low-power *sleep* mode, the fuel-gauge chipset actually consumes comparable power to that of the battery's self-discharge rate.

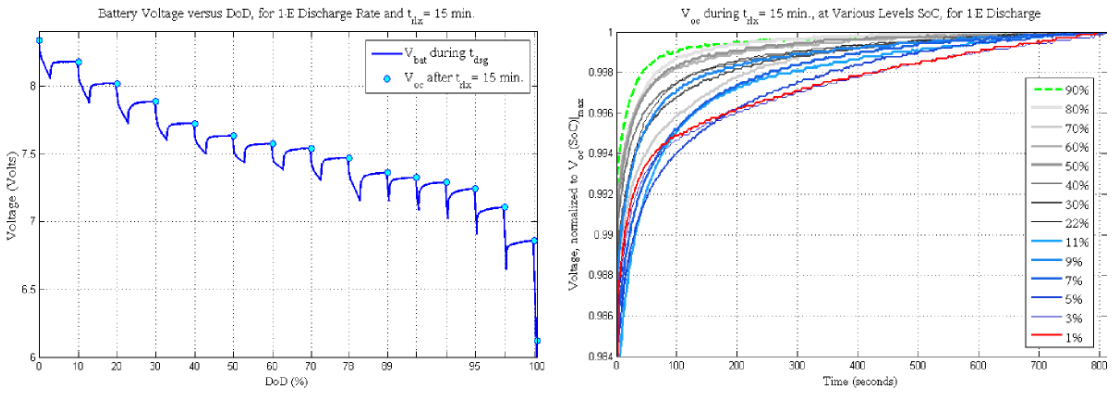

Figure 3.9: *Left*: V_{bat} measured during a 1·E discharge cycle with $t_{rlx} = 15$ minutes at various SoC levels. *Right*: V_{oc} during each t_{rlx} period, induced at the shown SoC levels. Note, each V_{oc} is normalized with respect to its maximum, end V_{oc} value.

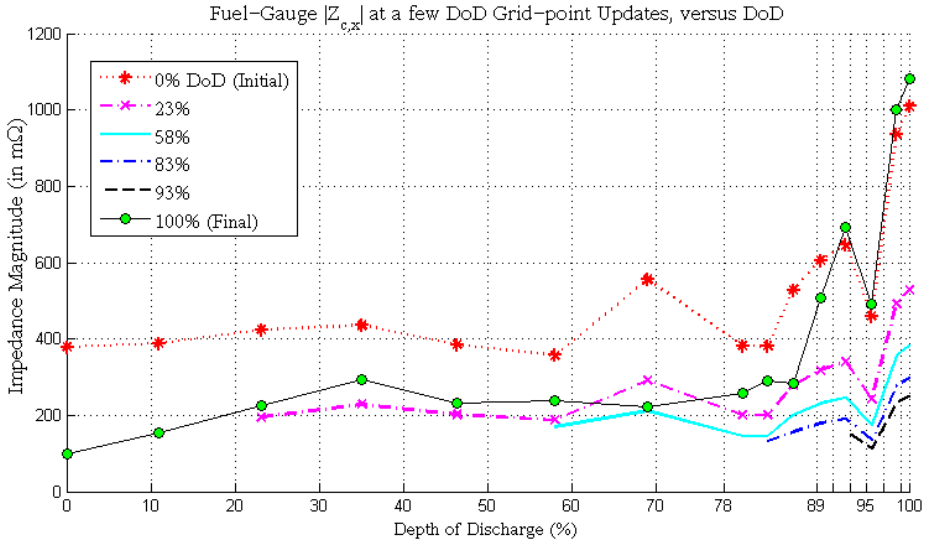

Figure 3.10: Plot of the fuel-gauge's internal resistance look-up table, shown as it updates at various DoD grid-points during a C/2 discharge cycle.

Chapter 4

Electrical Load Devices

Portable embedded systems usually house a large number of electronics. The robots considered in this thesis are equipped with: sensing and communication abilities, some form of mobility, computational resources, and onboard secondary battery source. This chapter highlights a number of such electrical devices and their power consumption requirements.

From a circuits perspective, the total power drawn from the battery (P_{dsg}) should equate to the aggregate sum of all actively powered load devices, plus stray losses (with some variability due to measurement error, and component tolerances, of course). Here the term *stray losses* lumps together many factors, ranging from a device's operating efficiency, to power lost in the form of heat.

Some of these components can be actively controlled, while others can only be enabled and/or disabled. For example, a CPU's core voltage and frequency can be modified by a software host control interface hardware scaled, while an onboard camera can be turned on/off. Clearly some components will consume more power than others; and of these, some may even prove to be negligible. To this effect, it may not be necessary to explicitly model every detail pertaining to each component's operating state(s).

Load devices can be classified as exhibiting constant current (CC), constant power (CP), or constant resistance (CR) characteristic profiles (or an ensemble of each) [7]. When a DC power converter (whether SMPC or linear regulator) is placed between the battery and system load, the battery's discharge profile will resemble more a constant power characteristic. For a power converter or regulator to maintain the necessary output power to a given load, it will draw whatever input power is needed in order to operate at a (device-specific) specified efficiency. But since the battery's voltage is actively being reduced, the converter will compensate by increasing its input current demands accordingly. This is one of the main reasons for describing battery discharging per E-rates - as mentioned in Chapter 3.

Illustrated in Figure 4.1 is a generic block diagram circuit of a mobile robot's source and

load. Block transfer functions G_B and G_C represent linear voltage regulators, and G_A a DC/DC SMPC. The smaller (orange) blocks represent various load devices scattered throughout the circuit, which operate at the DC voltages shown in red. These load devices are shown as imedances, which can (and will undoubtably) be arbitarily complex. A limited number devices are depicted in this figure, although it can easily be expanded to accomodate more. Capacitors are included here for completeness, as well as to disambiguate SMPCs from voltage regulators.

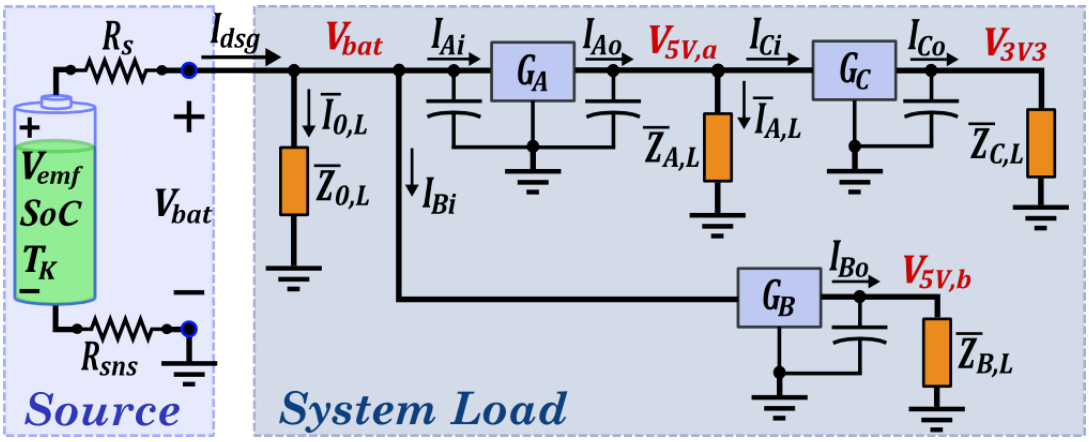

Figure 4.1: Simplified circuit schematic of a distributed power system with two cascaded power conversion stages.

Notice the outputs of G_A and G_B (labelled $V_{5V,a}$ and $V_{5V,b}$, respectively) are both 5V. The reason for illustrating two seperate 5V rails is to emphasize that frequently specific devices demand their own supply line. This is very common in embedded systems, whether for electromagnetic compatibility (EMC) reasons, noise isolation, signal conditioning, transient protection, seperation of high and low power components, and many others. If the input and output to a particular device is defined as electrical power, then G_x (for $x = \{A, B, C\}$) can be written in terms of its power efficiency.

4.1 Power Electronics

DC power conversion and voltage regulation is inherently a lossy process. There do exist, however, many newer devices specify operating efficiencies of even 95% [3], [42]. Although manufacturers emphasize throughout product literature, design guides, and application notes, that such maximum efficiencies are only achievable if designers adhere to several important guidelines. These range from circuit configuration and thermal management, to PCB layout and component placement. Recently many high efficiency devices have been put well within reach of anyone through the introduction of self-contained, point-of-load (POL) converter modules, such

as [3] and [43]. These small, single-board modules offer end-users an optimized design (in terms of reduced parts-count, low cost, thermal efficiency, and noise immunity, among many others) with plug and play functionality.

When comparing the options available for power converters, generally switch-mode DC/DC power converters (SMPCs) will have higher efficiencies than linear voltage regulators. On the other hand, SMPCs can introduce unwanted high frequency switching noise into supply lines which may be driving sensitive load electronics. Unless explicitly addressed in a design, allowing too large a ripple component in output current and/or voltage can be damaging to subsequent load devices. On the other hand, insufficient (and similarly even excessive) capacitance in filtering at either input/output terminals of a SMPC can lead to unstable operation and other unexpected problems [44]. So the best choice will depend on specific system load requirements. These types of considerations are described in the following subsections.

4.1.1 Switch-mode DC/DC Power Converters

Quite often there is one "main" SMPC responsible for dropping V_{bat}, to TTL compatible (5V and/or 3.3V logic) levels feeding many subsystems. Since V_{bat} in systems using four LiPB cells in series can be as high as even 16.8V, stepping down this voltage to 5V or less can be very lossy. So utilizing as low of battery voltage as possible in an embedded system is preferred. This way if higher voltages are required for some device in a given design, step-up (boost) converters can be used.

A converter's output power $P_{d,out}$ is related to applied input power $P_{d,in}$ through the device's operating efficiency η_d, as $P_{d,out} = \eta_d \cdot P_{d,in}$. Neglecting temperature effects for now, the power dissipated across the converter ($P_{\eta,d}$) can be represented as in Equation 4.1. The $P_{\eta,d}$ associated with a DC/DC converter is actually a function of several variables, and will change for variable operating regions as well as temperatures.

$$\underbrace{V_{d,in} \cdot I_{d,in}}_{P_{d,in}} = \underbrace{V_{d,in} \cdot I_{d,in} \cdot \eta_d}_{P_{\eta,d}} + \underbrace{V_{d,out} \cdot I_{d,out}}_{P_{d,out}} \tag{4.1}$$

Notice $V_{d,out}$ is known here, since we set this value. In addition, we will also assume that $V_{d,out}$ does not vary significantly. This is a reasonable assumption to make since most modern DC converters and regulators exhibit pretty good output voltage regulation tolerances - a fact that was later verified during testing. The non-isolated DC/DC converter modules considered here, are specified by their respective manufacturer as having a worst-case ripple in output voltage of less than 100 mV (peak-to-peak). Similar results were obtained when performing measurements in-house. Considering as well that these converters have bulk capacitance at their input and output terminals of over 200 μF, any transients or high frequency components are barely seen at either end of these devices.

Figure 4.2 illustrates how a DC/DC power converter's operating efficiency (η_d) depends on its output current ($I_{d,out}$) and input voltage ($V_{d,in}$). The original parent image (shown on the right side) is from the device's published datasheet [3].

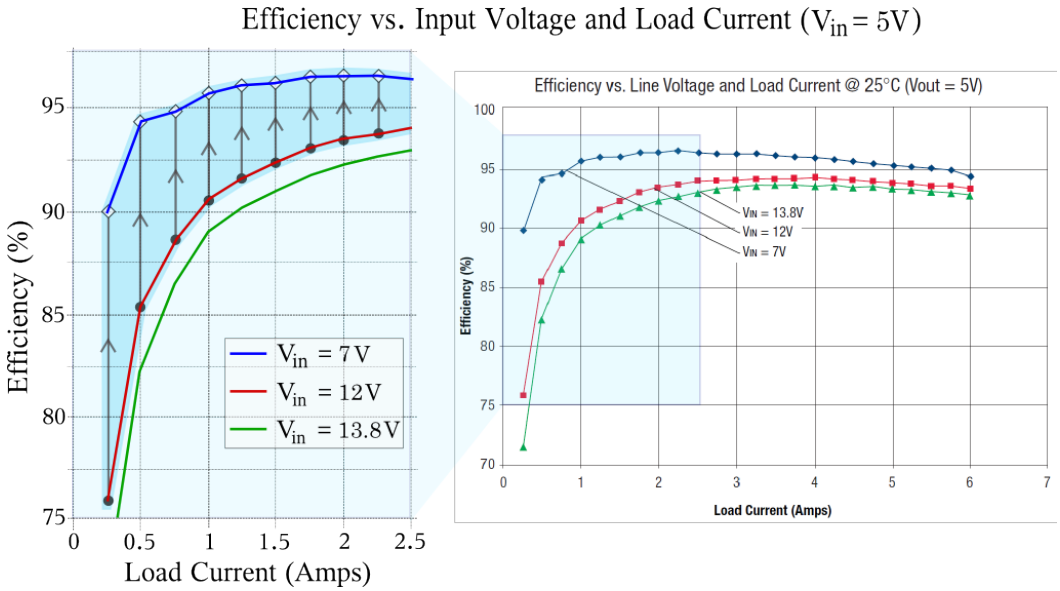

Figure 4.2: Graph of a DC/DC converter module's $I_{d,out}$ versus η_d for a few different values of $V_{d,in}$, and constant $V_{d,out} = 5$V. *Left*: Highlighted operating region of interest. *Right*: Original parent image from datasheet [3].

The highlighted, zoomed-in region on the left side of Figure 4.2 shows the approximate input voltage range for $2_S Y_P$ and $3_S Y_P$ configured LiPB packs (refer to Appendix D regarding this nomenclature). This device clearly operates more efficiently at lower input voltages. So as V_{bat} is being reduced during normal system operation, the converter will operate more and more efficiently (to a certain limit, of course) - as indicated by arrows pointing upward, moving from the solid black dots to the white diamond markers. In practice these arrows will not be straight, since the system's load current demands, which make up $I_{d,out}$, will unlikely stay constant throughout the duration of an entire discharge cycle.

This feature becomes more eminent at smaller values of $I_{d,out}$, where the difference between applying a $V_{d,in}$ of 7V and 12V results in an increased η_d of 15%. However as battery SoC approaches 0%, V_{bat} decreases more rapidly. So in this operating regime, the tradeoff for increasing DC/DC converter operating efficiency is sacrificing battery run-time (that is to say, t_{RTE}).

4.1.2 Linear Voltage Regulators

Linear LDO voltage regulators (or LDOs, for short) are widely used in battery-operated systems. As their name implies, an LDO's drop-out voltage (V_{ldo}) is much lower than traditional linear voltage regulators (see Appendix D for more details). This makes them especially useful in battery-powered electronics, where the input voltage (V_{bat}) is expected to decline with use.

LDOs also serve a means to decouple sensitive load electronics from higher power DC buses. They also prove effective in conditioning various load sections throughout DC power rails stages. Many regulator ICs also include control ports to enable/disable the device's output(s) using standard digital logic-level signals. This allows designers to further reduce a system's overall power consumption by turning off unused load segments [45].

The internal power dissipation of a single-chip LDO (P_{ldo}) is given in Equation 4.2. Here variables $V_{r,in}$, $V_{r,out}$, $I_{r,out}$, and $I_{r,gnd}$ represent (respectively), the IC's input voltage, regulated output voltage, output load current, and the device's quiescent operating current. The maximum P_{ldo} for a given application can be found with reasonable accuracy by substituting the maximum $V_{r,in}$ and minimum $V_{r,out}$ into this formula [46].

$$P_{ldo} = (V_{r,in} - V_{r,out}) \cdot I_{r,out} + V_{r,in} \cdot I_{r,gnd} \tag{4.2}$$

The majority LDO regulators manufactured within the past decade or so are optimized for use in portable battery-powered applications. Such devices have practically insignificant $I_{r,gnd}$ (at least in comparison to $I_{r,out}$), which is usually on the order of a few μA. So P_{ldo} is often approximated without the last term in Equation 4.2.

This equation does not account for temperature effects during device operation. Thermal management considerations in DC power conversion circuits is a very important topic in embedded designs. Excess heat generated during use will not only steer the performance of a regulator IC itself, but will inevitably determine the efficiency of other circuits coupled to their inputs and outputs. When modeling a regulator's heat generation during normal operation, two thermal resistances are of particular importance. The first is the junction to ambient thermal resistance (θ_{JA}), which is usually given in a device's datasheet, although it can be calculated using Equation 4.3. In this equation, $T_{A,^\circ C}$ is the ambient temperature of the environment and $T_{J,^\circ C}$ is the junction temperature.

$$\theta_{JA} = \frac{T_{J,^\circ C} - T_{A,^\circ C}}{P_{ldo}} \tag{4.3}$$

Since θ_{JA} is device specific and likely included in manufacturer performance specifications, Equation 4.3 would be rearraged and solved for $T_{J,^\circ C}$. The other important thermal resistance is the junction to (heat) sink resistance (θ_{JS}). This constant should be used when the device is mounted to a heat-sink - whether directly attached as an aperature or as a ground plane

integrated into the physical PCB. θ_{JS} can be computed for a given heat-sink's physical geometry and material properties, and using this result the mounting surface temperature ($T_{H,^\circ C}$) can be found from Equation 4.4.

$$T_{J,^\circ C} = T_{H,^\circ C} + \theta_{JS} \cdot P_{ldo} \tag{4.4}$$

4.2 Electric Drives

For the size and weight class of robots considered here, suitable candidates for motors driving the robot's wheels are permanent magnet brushed DC machines. Precious metal commutated motors were preferred over sintered graphite-based materials, since they have lower contact resistance and better linearity in performance characteristics.

Electromechanical components discussed below are separated in two categories, permanent magnet brushed DC (PMBDC) motors, and DC servo-motors. In this thesis, the discussion focuses on miniature coreless (skew-wound) PMBDC motors - used for displacing the robot; and a DC servo-motor - to actuate the robot's stabilizing caster.

4.2.1 Permanent Magnet Brushed DC Motors

Dynamics modeling of the robot's coreless PMBDC micro-motors follows the formulation outlined in [47]. The first step is to divide the DC machine into electrical and mechanical subsystems, as shown in Figures 4.3 and 4.4, respectively. All variables and constants depicted in these figures, as well as those introduced in subsequent discussions, are defined in Table A.1.

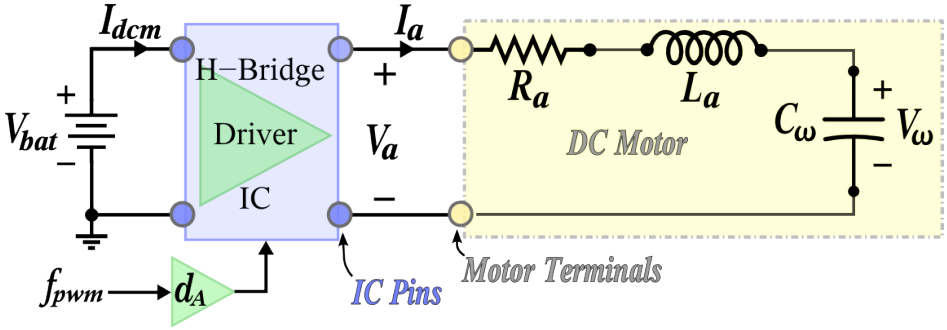

Figure 4.3: Simplified electrical model of the coreless PMBDC micro-motor.

Starting with the electrical portion of the model, Figure 4.3 is used as a visual aid. Controllable parameters here are the input PWM drive signal's switching frequency ($f_{s,pwm}$) and its duty cycle (d_A). When running the motor at rotational velocity ω_m, the counter-EMF voltage (V_ω) generated in the motor, can be found by the linear relationship $V_\omega = k_\omega \cdot \omega_m$, where k_ω

is the motor's speed constant. The electrical analogy of motor intertia is capacitance, which is given by $C_\omega = k_\omega^2 \cdot J_{eq}$, where J_{eq} is the equivalent motor (with load, gearhead, etc.) inertia, as seen by the source [47], [48].

The motor's armature current I_a can be determined by summing voltages around the right loop of Figure 4.3. Applying Kirchoff's voltage law (KVL) we obtain the differential relation in Equation 4.5 - where all variables are defined in Table A.1. To facilitate conspicuity in discerning constants from variables, those written in bold font (that is, I_a, ω_m, and V_a) represent time-dependent vectors.

$$\dot{\boldsymbol{I}}_{\boldsymbol{a}} = -\frac{k_\omega}{L_a} \cdot \boldsymbol{\omega_m} - \frac{R_a}{L_a} \cdot \boldsymbol{I_a} + \frac{1}{L_a} \cdot \boldsymbol{V_a} \tag{4.5}$$

Under DC steady-state operating conditions, $\dot{I}_a \approx 0$, and Equation 4.5 becomes linear. An important detail worth mentioning is that the motor's *actual* I_a draw is $I_a + I_{a,0}$, where $I_{a,0}$ is the no-load current.

Next, looking at the mechanical side of the motor, Figure 4.4 will be used as a reference. This figure illustrates torques acting about the shaft of rotation. Green arrows pointing upwards denote constructive (or positive) torques acting about the are shown as green arrows pointing upwards, whereas retarding torques are represented by red arrows pointing downward.

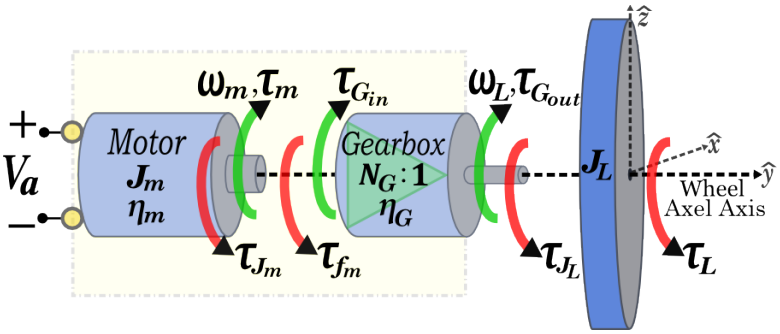

Figure 4.4: Diagram of the mechanical model portion considered for the PMBDC micro-motor.

The output torque at the load (here a wheel) is found by summing individual torques about the $\hat{y}$-axis. Due to the gear-reduction block, two torque equations must be written - one for each side of the gearhead. The gearbox's input torque (on its left side) is $\tau_m = \tau_{G,in} + \tau_{J_m} + \tau_{f,m}$; and its output torque is $\tau_{G,out} = \tau_{J_L} + \tau_L$. Here, variable $\tau_{f,m}$ is the friction torque modeling viscous damping. Since $\tau_{G,in}$ and $\tau_{G,out}$ are related by the gearhead's efficiency, we have the following constraint $\tau_{G,out} = \eta_G \cdot \tau_{G,in}$. From this fact, the previously mentioned equations can be combined and solved for τ_m, yielding the result summarized in Equation 4.6.

$$\tau_m = \tau_{J_m} + \tau_{f_m} + \frac{1}{\eta_G} \cdot (\tau_{J_L} + \tau_L) \tag{4.6}$$

However we know that $\tau_f = f_m \cdot \omega_m$; and also since $\tau_{J,m} = J_m \cdot \dot{\omega}_m$, and $\tau_{J,L} = J_L \cdot \dot{\omega}_L$, Equation 4.6 can be reduced even further. Combining prior equations, and after some algebraic simplification, the motor's mechanical model is given in Equation 4.7.

Many manufacturers often provide a parameter known as the "slope of the speed-torque curve" ($\Delta\omega_m/\Delta\tau_m$) in datasheets, which can vastly simplify analysis. Similarly, the *motor constant* k_M gives a quantitative measure of the motor's torque capabilities with respect to its input power demands.

$$\dot{\boldsymbol{\omega}}_{\boldsymbol{m}} = -\frac{f_m}{J_m} \cdot \boldsymbol{\omega}_{\boldsymbol{m}} - \frac{1}{J_m} \cdot \boldsymbol{\tau}_{\boldsymbol{m}} \tag{4.7}$$

The motor's mechanical dynamics are coupled to the developed electrical model, in Equation 4.5, through the linear relation $\tau_m = k_\tau \cdot I_a$. So Equations 4.5 and 4.7 can be expressed either in terms of τ_m or I_a. In the DC steady-state, $\dot{\omega}_m \approx 0$, so Equation 4.5 can be simplified since ω_m and τ_m can be written as a linear relation.

The motor's speed-torque curve is graphed in Figure 4.5. Also appended to this figure are the motor's mechanical output power ($P_{m,out}$) as well as its operating power efficiency (η_m). Note that mechanical output power is defined as $P_{m,out} = \tau_m \cdot \omega_m$. This is the output power of the DC motor *only*, and does not account for losses in gear-reduction, which can be just as (if not more) inefficient in electromechanical power conversion

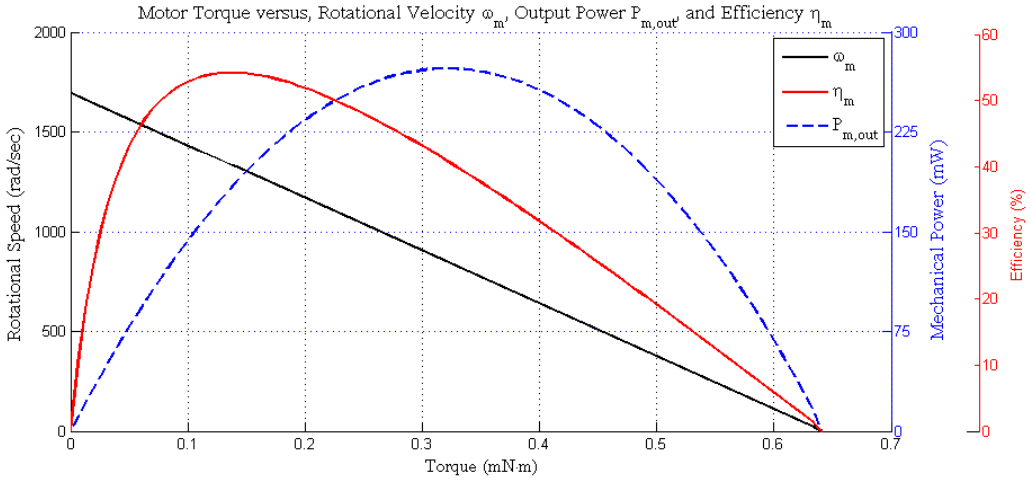

Figure 4.5: Graph of τ_m, versus ω_m, $P_{m,out}$, and operating η_m.

The motor mechanical output power delivered to the wheel is simply $P_{G,out} = \tau_G \cdot \omega_G$. This can be equated to the motor's input power $P_{m,in} = V_a \cdot I_a$ by defining (power) efficiency η_{em} as in Equation 4.8. This quanitity will define the overall motor assembly's electromechanical

power efficiency.

$$\eta_{em} = \frac{\tau_G \cdot \omega_G}{V_a \cdot I_a} \tag{4.8}$$

To investigate the effects associated with a chosen $f_{s,pwm}$, we turn our attention to the block labeled "H-bridge driver IC" in Figure 4.3. The driver IC's integrated H-bridge is shown as it attaches to the motor's terminals, in Figure A.3.

Increasing $f_{s,pwm}$ will generally increase switching losses in the H-bridge MOSFETs. However it will also reduce the amount of current ripple (Δi_a) in the total I_a. Since I_a is directly proportional to τ_m, this reduces pulsations and vibrations as a consequence of torque ripple. As a result, the motor will run "smoother," with less torque pulsations. This in turn will likely increase its operational lifetime as well. Other effects from $f_{s,pwm}$ being too high or low include inductive kick-back (which can usually be mitigated using diodes), introduction of audible noise, transient ringing, and many others. Equation 4.9 relates Δi_A to $f_{s,pwm}$, for a single-ended ($Va \in [0, V_bat]$) switching scheme during steady-state operation [49], [50].

$$\Delta i_A = \frac{d_A \cdot V_{bat}}{f_{s,pwm} \cdot L_a} \tag{4.9}$$

Figure 4.6 graphically illustrates $f_{s,pwm}$ versus ripple current Δi_A variation, for a set duty cycle. The left $\hat{y}$-axis shows the current's AC component, and the right $\hat{y}$-axis the DC-component of I_a. Notice the RMS DC component of I_a stays fairly constant throughout the range of $f_{s,pwm}$ shown.

Choosing an appropriate $f_{s,pwm}$ clearly depends on the system and its use. If we were designing a covert reconnaisance robot, then running its motors at audible frequencies would probably not be the best idea. Robots carrying sensitive payload, or streaming video from an onboard camera, a smoother drive profile may be more important - in which case, excess vibrations might distort or blur captured images.

4.2.2 DC Servo Motor

DC servo motors are found in many robotic systems. Their simple three-wire interface (supply voltage, ground, and control signal inputs) make them relatively easy to drive, and control. They are also affordable and readily available for purchase from many online vendors. However, they are physically restricted from rotating a full 360°, and as such complicates simple application of the equation for rotational mechanical power (that is, mechanical torque multiplied by rotational velocity). The mechanical torque supplied by the DC servo motor that must instead be considered is that to maintain a given angle, termed the *holding torque* (τ_{hld}).

Mounting the stabilizing caster-arm (or caster-*tail* - since it is placed on the back of the robot) to a servo motor was a compulsory constraint in order to appropriately fit inside the

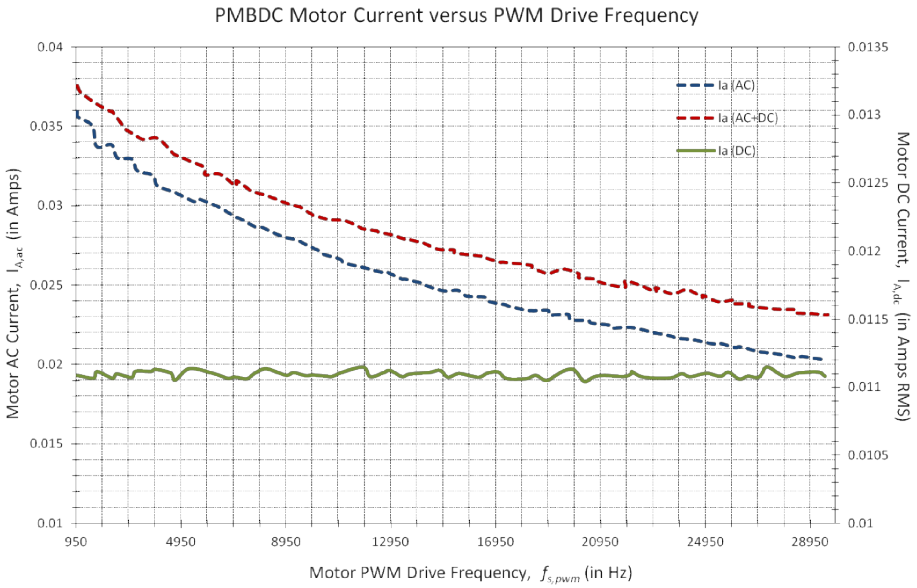

Figure 4.6: PWM switching frequency $f_{s,pwm}$ versus measured AC+DC, AC, and DC components of I_a (curves shown from top to bottom, respectively), in Amps RMS.

mobile docking and recharging station (MDS), for which the robots were designed. This was probably the largest reason why the design did not evolve, since it otherwise would require a more complex method to articulate the caster. The resultant design does however introduce a third degree of freedom (DOF) to the system, since the robot can now tilt its body about its wheel axle's axis - and in turn the field of view (FOV) of all onboard sensors.

This can also prove insightful when characterizing a TWMR's mechanical dynamics. Observing how the caster's position and orientation (with respect to the ground) influences overall system power consumption, we can associate a measure of power with maintaining structural balance. This angle can be chosen to reduce the effects of recoil jerk when halting to a sudden stop, and in turn minimize the required holding torque. If the type of surface terrain where the robot will be used is known or measurable, the designer can experimentally determine the "best" relative caster-tail angle (or at least surmise an acceptable trade-off) and even permanently fix this configuration in a robot's final design. This would in turn reduce the robot's overall power consumption by eliminating the counter-balance holding torque from the servo-motor.

So choosing a hobby-grade DC servo motor to actuate the tail's position will likely consume more power than using a DC linear actuator. Furthermore, if the robot is heavy enough, this may

even overshadow the power demands of DC motors driving the wheels. Changing the caster's physical placement on the robot, how it is mounted, its orientation, length, and other similar specifications alter the servo's static power draw (sometimes significantly) in a more intuative manner. Other, slightly less obvious, effects can also impose on power consumption, such as the caster's material properties.

The material from which the caster is fabricated will also play a part in changing the servo's power consumption. Choosing nitrile rubber favors damping the effective bounce-back during sudden stops (or similar jerking motions), which in turn will reduce impulsive additive forces that would result in larger τ_{hld} demands. On the other hand, a rigid tail will exhibit some recoil when the robot comes to a sudden halt. However bending and other deformations will consume more power when holding a static position. So there are obvious trade-offs between rigidity, stability in bounce-back, and servo-motor power consumption.

4.3 Computational Power

Most embedded systems comprise more than just one, single onboard processor. On the contrary, more often mobile robots split tasks between their onboard computational resources, utilizing different processors to perform various tasks of interest. Embedded CPUs usually fall into two very broad categories: microcontrollers and microprocessors, although both are sometimes confusingly referred to as CPUs. Most often, lower-level computational demands are usually assigned to a dedicated microcontroller (performing such tasks as motor control, data conversion, I/O switching control, and many others). Higher-level algorithms that are more computationally intensive (such as vision processing and precision floating-point computations) are best suited for a microprocessor CPU or specific system-on-chip device (for example digital multimedia processors, DSPs, and co-processor graphics cards).

In tracking power demands for processing, the main variables are the input voltage and current to the device(s), and knowledge of active I/O and memory peripherals as well as their frequencies and voltage levels. For the microcontrollers considered here (that is, 8-bit low-power consumption types), only a subset of these variables are applicable - since advanced CPU features such as DVS and DVF (for example), are not present. Although there do exist some power sub-states, such as sleep, idle, hybernation, and other comparable operating modes, that can be found from product literature.

Supported CPU core frequency (f_{core}) and voltage (V_{core}) ranges for the mobile embedded CPU used in this work are shown in Table 4.1 (data from [1]). Clearly the CPU's power consumption will depend on several parameters across all its (internal) peripherals. Those listed in Table 4.1 are SDRAM, memory controller, and internal system bus operating frequency (f_{sdram}, f_{mctl}, f_{intsb}, respectively). Hence the overall IC's power consumption (P_{cpu}) is usually described under a set of voltage (V_{cpu}) and freqency (f_{cpu}) operating conditions.

	Operating f_{cpu} Range (in MHz)	V_{core} (in V)			f_{core} (in MHz)		
		min	nom	max	min	nom	max
1	{13/13/13/13}†	0.95	1.00	1.705	13	-	13
2	{13/13/13/13}†† {91/45.5/91/45.5} {104/104/104/104}	0.95	1.00	1.705	91	-	104
3	{156/104/104/104}	0.95	1.00	1.705	-	156	-
4a	{208/104/104/104}	0.9975	1.05	1.705	-	208	-
4b	{208/208/104/104} {208/208/208/104}	1.12	1.18	1.705	-	208	-
5a	{312/104/104/104}	0.99	1.10	1.705	-	312	-
5b	{312/208/104/104} {312/208/208/104}	1.1875	1.25	1.705	-	312	-
6	{416/208/104/104} {416/208/208/104}	1.2825	1.35	1.705	-	416	-

Table 4.1: Supported CPU core voltage and frequency ranges for Marvel's PXA270 XScale processor. The allowable ranges of CPU operating frequencies (f_{cpu}) are defined as: $f_{cpu} = \{f_{core}/f_{intsb}/f_{mctl}/f_{sdram}\}$ (all in MHz). This data as well as other important information can be found in [1].

Although only a handfull of V_{core} values are shown in this table, these can be adjusted in increments of 25 mV (throughout the range 0.85V $\leq V_{core} \leq$ 1.40V), via a TWI data bus that interfaces to a dedicated power management IC (PMIC). Many PMICs are available in tiny BGA and QFN footprints while offering a wide range of features. In fact, these PMICs provide a complete solution to manage (configure, control and report) multiple power rails for a single-chip power management solution for distributed load power solutions. Power rails may included one or more inductive step-down converters, charge pumps (or inductorless step-down converters), LDO voltage regulators, and even an integrated battery charger. The specific PMIC of interest here, is taylored for use with the PXA270 processor, and is detailed in [42].

To determine such a CPU's power consumption when applied to an a mobile robot, or any embedded system for that matter, the given *power states* in the product's literature and datasheet serve as a good starting point. A more thorough discussion regarding scaling of CPU frequency and voltage settings, for the specific processor used here, can be found in [51].

The average dynamic (switching) power dissipated in a CMOS-based central processing unit (P_{cpu}) is often generalized by Equation 4.10. Variables C_{swi}, N_{swi}, and refer to the CPU's capacitance and number of switching elements, respectively. The prominent squared voltage

† This denotes different settings of the processor's core clock configuration register (CCCR); specifically for changing the core's phase locked loop (PLL) control disable bit (CPDIS), and the periphiral's PLL control disable bit (PPDIS) within the CCCR. For this particular set of frequencies and operating conditions, the CCCR bits are configured as [CPDIS,PPDIS] = [1,1].

†† For CCCR register set to [CPDIS,PPDIS] = [1,0] (refer to [1] for more details about configuration register settings).

term accentuates the importance of V_{cpu} on overall P_{cpu}.

$$P_{cpu} = C_{swi} \cdot N_{swi} \cdot V_{cpu}^2 \cdot f_{cpu} \tag{4.10}$$

A few different avenues can be taken to approximate P_{cpu}. We can look up values from device specifications and make more tables like 4.1 but for all operating conditions, or directly measure present power consumption from the PMIC's I^2C data bus. Unfortunately, for the COTS SBC employed on the systems here, the designers do not make these data lines accessible. Otherwise this would be the most accurate representation of the robot's P_{cpu}, since the PMIC feeds all of the processor's internal peripherals. On a similar note, for this same SBC (further described in appendix B) f_{core} is specified as "not offered" for the particular PBGA packaged IC physically populated on the COTS PCB [1].

4.4 Wireless Communication Peripherals and Chipsets

Wireless device radios can consume a fair amount of power at the system's load. Most of the time, a mobile robot will utilize (relatively) long range communication, for example RF, WiMAX, GSM or CDMA standards, and GPS devices; as well as short range wireless radios (such as Wi-Fi, Bluetooth, and IR signaling). This section outlines a general way to determine this power. Further details surrounding this discussion can be found in Appendix A.2, which serves to suppliment topics covered in this section.

Most wireless devices provide a data bus to configure their various operating modes. This provides host devices with the flexibility to actively control parameters that may exhibit larger influence on the system's overall power consumption - such as data transfer rate, transmit power, low power sleep or wake modes, and several others. These configurable features are often included in software drivers, and can easily be accessed via terminal commands (such as *iwconfig*, *ifdown*, and many others) on Unix machines. The transmit power (P_{TX}) read back is usually given in dBm, but can readily be converted to Watts using Equation 4.11.

$$P_{TX,dBm} = 30 + 10 \cdot \log_{10}\left(P_{TX,W}\right) \tag{4.11}$$

One of the difficulties in measuring a wireless radio module's transmit power ($P_{TX,dBm}$), at least when using terminal commands, is that this variable describes only the power contained within the transmitted signal. So the value read-back from a terminal does not account for power consumption of its internal ICs, voltage regulators, and other passive components contained within the module's encasing. Hence characterizing such a wireless radio's power consumption (in its entirety) cannot be done based solely on this value.

Many robots utilize RF radio communication links in the VHF range. In such systems, the terrestrial 75 MHz or aeronautical 72 MHz frequency bands are usually employed. Using

RF frequencies for data transmission, contrast to high (that is, greater than 1 GHz) frequency data links, has its benefits. For example, lower frequencies inherently have longer wavelengths λ (defined as $\lambda = c/f_c$, where c is the speed of light, and f_c the carrier signal frequency), and as such can travel longer distances - considering line of sight (LOS) propagation. On the other hand, sub-GHz frequencies cannot penetrate through walls and other obstacles as easily; which can lead to larger losses arising from reflections, refractions, multi-path fading, and other nonlinear destructive effects.

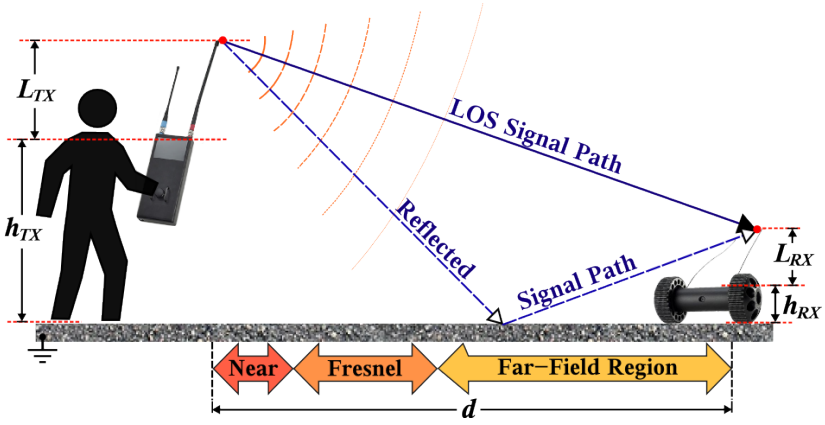

Figure 4.7: Visualizing wireless RF signal propagation for the physical setup surrounding the robot described in [4] (pictures of the robot and controller were modified from their parent images - which are from ReconRobotics Corp.).

Whether user controlled or remotely operated, the signal path propagation model for a small terrestrial mobile robot can be visualized as in Figure 4.7. In this system, the robot is shown in the far-field region, with no obstructions or interference between transmitter and receiver, only direct and indirect (that is, reflected) LOS signaling. In this case, for direct (that is, obstruction-free) LOS transmission, the ground-wave mode of propagation can dominate - contrast to the direct LOS signal or its other reflected subcomponents. This really is not surprising, since the robot's physical height from ground is less than the carrier frequency's wavelength (λ).

Reception strength directly relates to the receiver's input power, or P_{RX}, for some transmit power P_{TX}, and attenuation during signal transmission. The chosen propagation model(s) should reflect an application's end-use environment; considering terrain irregularity, carrier frequency, signal path obstructions, and many others. Some path propagation models applicable to small mobile robots (similar to those described here) include: Bullington, Broadcast and Carey models, Egli, Hata-Davidson, and Okumura propagation models, to name only a few [52]. However, if the same robot is used in a different environment, the model must be either modified or even completely changed.

$P_{TX,dBm}$ can however, be incorporated into the formulation of a specified task-efficiency. In

this context, the figure of merit lies not in power losses due to wireless radio module's supply demands, but instead the robot's ability to maintain a robust communication link between robot and user. Such an application is described in Appendix A.2, where an impedance matching network is simulated, designed, tested, and verified to almost *double* the robot's LOS communicable range.

Lying somewhere between wireless communications and active sensing, are peripheral devices used for navigation. Nevertheless, satilite-based navigation systems such as GPS modules are still categorized as wireless communication devices. Using a COTS GPS unit, with DC input voltage $V_{gps} = 3.30$V, the measured RMS steady-state current was $\overline{I}_{gps} \approx 35.50$ mA, and hence power $P_{gps} = 118.86$ mW.

4.5 Active Sensing

Within a given voltage range, proprioceptive and exteroceptive sensors can usually be approximated as constant-current sinks. If a particular sensor's supply voltage is connected directly V_{bat}, then as long as V_{bat} remains within the device's operating range, it will exhibit a constant-current load characteristic. However, since most active sensors require clean, stable supply voltages, they are often powered by low noise LDO voltage regulators - which were modelled in section 4.1.2 as constant-power load devices.

Measuring the power consumption in active sensors is relatively straightforward. If a particular sensor's input voltage is supplied directly from the battery's terminals, then the power consumed by the sensor is simply V_{bat} multiplied by its input current. This input current can be experimentally measured using a small-valued series sense resistor throughout the full range of V_{bat}. On the other hand, if a sensor's input voltage is supplied from subsequent DC power conversion or voltage regulation, its input power will be a function of the power converter's operating conditions. In this case, the sensor's input voltage will be the same as the converter's output voltage, and its current draw can again be measured using a sense resistor.

Motor encoders are integrated into the physical motor housing. They are magnetic encoders, which can take an input voltage ($V_{enc,in}$) of anywhere between 4.5V to 13.8V DC, and output is a 50% duty cycle square-wave (between $[0, V_{enc,in}]$) that is proportional to ω_m. Despite the wide input voltage range, encoders are fed a 5V supply voltage, since their output must be TTL logic-level compatible.

Chapter 5

Mechanical Dynamics and Kinematics

What distinguishes a mobile robot from a simple wireless sensor node is its ability to move, even manipulate and/or interact with its surroundings. Examples of the latter are a humanoid robot with arms, and search and rescue robots clearing a collapsed structure's rubble or debris with a manipulator. This chapter examines the mechanics of differential-drive motion and their analytics in two-wheeled mobile robots (TWMRs). Of particular interest is to determine how both passive and active mechanisms contribute to the mechanical (kinetic) energy associated with displacing a robot.

5.1 Mechanical Dynamics

To generalize the approach in model formulation, the total mechanical energy is divided in two categories: the electromechanical energy required to displace the robot, and the energy to physically maintain a *stable pose*. Here a stable pose refers to one where the robot does not physically tip over. TWMRs often employ a caster to address this issue of balance, as well as to constrain their kinematics - otherwise the robot would just spin in place when trying to drive forward/backward. Articulating the robot's caster by coupling one end to a DC servo-motor serves to evaluate the energy cost(s) to balance a TWMR. This was briefly mentioned in Section 2.2, and is revisited here - with an emphasis on mechanical dynamics.

Due to the presence of an actuating caster-tail*, the forces and torques on components of the robot will change as a function of the caster's angle with respect to ground surface. To

*The caster is referred to as a "tail" since it is attached to the back side of the robot. Regardless, the terms caster, caster-arm, caster-tail, as well as simply just *tail*, are used synonymously throughout this thesis.

determine reactionary forces with varying geometry in this system, the robot's caster-tail and its body are, together, treated as a four-bar crank slider mechanism.

The total mechanical kinetic energy of the robot (E_K) comprises both translational ($E_{K,t}$) and rotational ($E_{K,r}$) components, as summarized in Equation 5.1. Variables m_{tot}, u_{eq}, ψ_{eq}, and J_{eq} represent, respectively, the robot's total mass, equivalent linear velocity, rotational velocity (that is, its change in heading), and equivalent overall mass moment of inertia.

$$E_K = \underbrace{\frac{1}{2} \cdot m_{tot} \cdot u_{eq}^2}_{E_{K,t}} + \underbrace{\frac{1}{2} \cdot J_{eq} \cdot \psi_{eq}^2}_{E_{K,r}} \tag{5.1}$$

Let $E_{K,in}$ be the total electrical input energy demands from its PMBDC (wheel) motors. The functional mapping between $E_{K,in}$ and E_K can be represented as efficiency $\eta_{K,em}$, defined in Equation 5.2a. Similarly, defining the total energy required to stabilize the robot as E_S, and also electrical input energy to the caster's servo motor as $E_{S,in}$, the energy efficiency in stabilizing the robot is given per Equation 5.2b.

$$\eta_{K,em} = \frac{E_K}{E_{K,in}} \tag{5.2a}$$

$$\eta_{S,em} = \frac{E_S}{E_{S,in}} \tag{5.2b}$$

The overall energy delivered to electromechanical device inputs will be $E_{T,el} = E_{S,in} + E_{K,in}$, resulting in total mechanical energy $E_{T,mech} = E_K + E_S$. which will be revisited towards the end of this chapter.

5.1.1 Energy for Stabilization

To calculate the holding torque about the robot's servo-actuated caster - as a function of the tail's angle (θ_3) with respect to a global horizontal, a four-bar crank slider mechanism is used. This mechanism setup, along with its constituent linkages and angles, is shown in Figure 5.1. To better understand this illustration and what it aims to depict, refer to Figure B.5 in Appendix B.2.1.

The length of linkage 1 (l_1) is equal to the wheel's radius (r_w) minus half the tail's end effecter height (shown as r_{ctb} in Figure 5.1) - measured from the ground. Linkage 1 is placed perpendicular to the global (horizontal) ground plane. Here the end effecter employed is a garolite ball, whose shape and material were chosen to minimize friction-based losses, while still maintaining simplicity in mechanical design.

Linkage 2 (with length l_2) is placed between the wheel axle's center point and the axis about which the caster-tail angle is varied. The length of linkage 3 (l_3) is defined from the center-axis

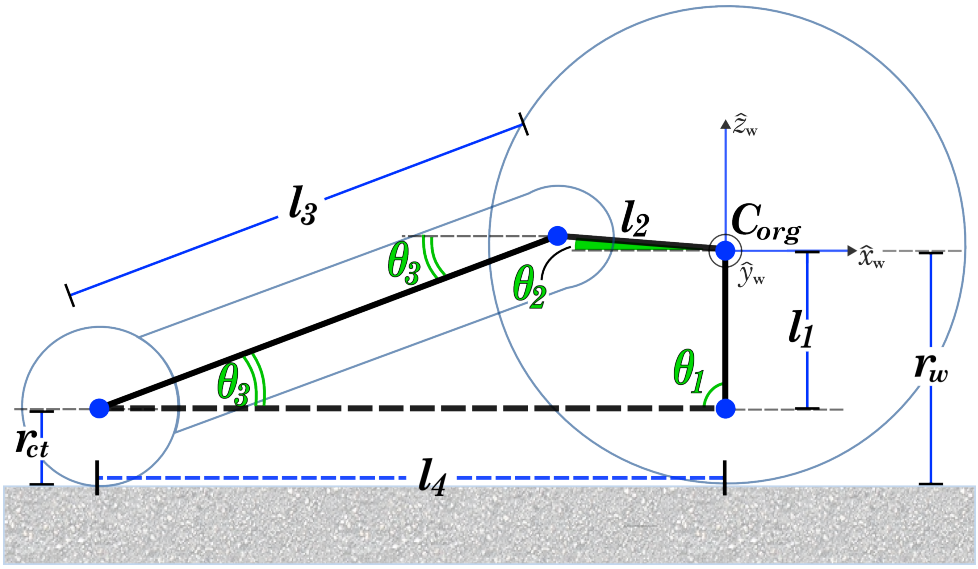

Figure 5.1: Side view of the TWMR (shown in Figure B.5) illustrating the mechanism setup for describing the caster-tail dynamics.

of the caster's pivoting point to the center of the caster's passive end effecter sphere. Finally, the length of linkage 4 (l_4) stretches from the center of the caster's end effecter back to the wheel's central axis, closing the structure by linking back to l_1. The four-bar crank slider mechanism is used to determine the angle of l_2 from the global horizontal (θ_2) and the length l_4. Here l_4 (drawn with a dashed line in Figure 5.1) will vary in length with changing θ_2. Following the formulation in [53], Equations 5.3 and 5.4 are derived for variables θ_2 and l_4 (respectively).

$$\theta_2 = sin^{-1}\left(\frac{-l_1 - l_3 \cdot sin(\theta_3)}{l_2}\right) \tag{5.3}$$

$$l_4 = l_2 \cdot cos(\theta_2) + l_3 \cdot cos(\theta_3) \tag{5.4}$$

The position of the robot's center of gravity (COG) will be shifted as the tail's angle with the ground (θ_3) is varied. This is illustrated in Figure 5.2. It is of interest here to determine how changes in angle θ_3 affect C_{sys}. In this formulation the robot is divided into two structures, its body and caster-tail, each with COG located at points marked C_{bd} and C_{ct} (respectively) in Figure 5.2.

The below transformations are used to determine the Cartesian coordinates (defined here in the $\hat{x}$-$\hat{z}$ plane, per Figures 5.1 and 5.2) of the caster and body respectively. The origin in these figures is denoted C_{org}, and is located at the center of the wheel's axel. Angle φ is defined as that between l_2 and C_{bd}. This angle is fixed and was determined from the robot's mechanical

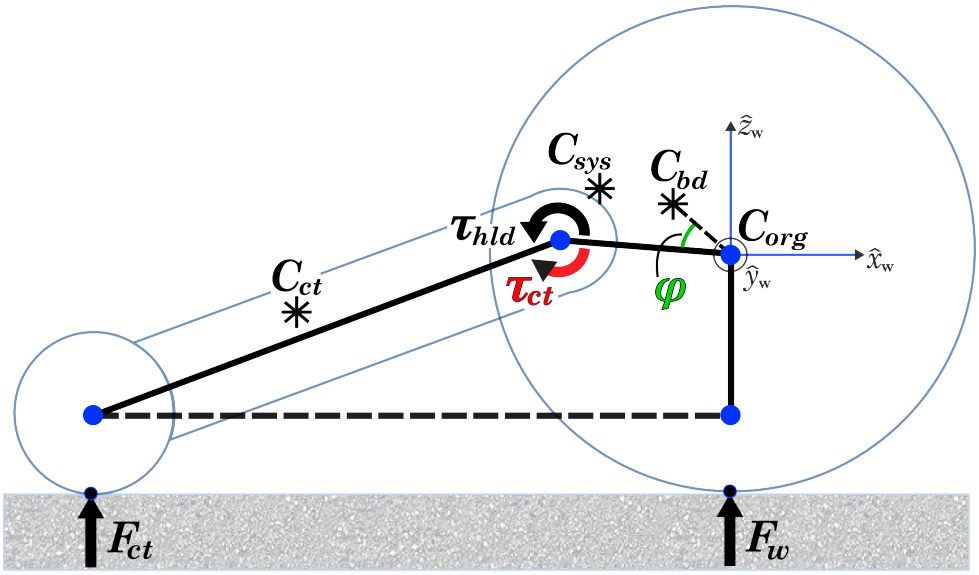

Figure 5.2: Side view of the TWMR (in Figure B.5), illustrating COG dynamics.

CAD model. Here $l_{ct,c}$ is the length from the axis of the caster-arm to the COG of the caster. Similarly, $l_{bd,c}$ is the length from the axis of the wheel to the COG of the body.

$$\begin{bmatrix} C_{ct,x} \\ C_{ct,z} \end{bmatrix} = \begin{bmatrix} l_2 \cdot cos(\theta_3) + l_{ct,c} \cdot cos(\theta_3) \\ l_2 \cdot sin(\theta_3) - l_{ct,c} \cdot sin(\theta_3) \end{bmatrix} \tag{5.5}$$

$$\begin{bmatrix} C_{bd,x} \\ C_{bd,z} \end{bmatrix} = \begin{bmatrix} l_{bd,c} \cdot sin(\frac{\pi}{2} - \varphi - \theta_2) \\ l_{bd,c} \cdot cos(\frac{\pi}{2} - \varphi - \theta_2) \end{bmatrix} \tag{5.6}$$

The resultant location of the entire robot's COG (abbreviated C_{sys}) is found by using the caster-tail and body COGs, as shown below in Equation 5.7. If the robot is assumed to traverse on a flat terrain (as mentioned above), only forces along the $\hat{x}$-axis will contribute to the overall dynamics of the caster-arm. Hence, only the $C_{sys,x}$ term (that is, its $\hat{x}$-axis component) in Equation 5.7 is required to calculate the forces (acting on) and moments (acting about) the caster-tail.

$$\begin{bmatrix} C_{sys,x} \\ C_{sys,z} \end{bmatrix} = \begin{bmatrix} \frac{C_{ct,x} \cdot m_{ct} + C_{bd,x} \cdot m_{bd}}{m_{ct} + m_{bd}} \\ \frac{C_{ct,z} \cdot m_{ct} + C_{bd,z} \cdot m_{bd}}{m_{ct} + m_{bd}} \end{bmatrix} \tag{5.7}$$

Knowing the coordinates of the entire robot's COG for all permissible tail angles (θ_3), a statics problem can be formulated, and in turn solved for the torque about the caster's pivoting axis. The normal force components acting on the wheel and tail (F_w and F_{ct}) are found using

Equations 5.8 and 5.9, respectively. Here F_N and a_G represent the normal force and acceleration due to gravity.

$$F_w = \underbrace{a_G \cdot (m_{bd} + m_{ct})}_{F_N} \cdot (l_4 - C_{sys,x}) \tag{5.8}$$

$$F_{ct} = a_G \cdot (m_{bd} + m_{ct}) \cdot \frac{(1 - l_4 - C_{sys,x})}{l_4} \tag{5.9}$$

Splitting up the robot into two separate structures (its "body" and caster), the moment about the caster's pivot-point of actuation can be found from Equation 5.10 for variable angles θ_3. These results were further verified using a CAD model of the robot (see Appendix B.2.1) in the mechanical design software Pro/ENGINEER.

$$\tau_{ct} = l_3 \cdot F_{ct} \cdot cos(2\pi - \theta_3) \tag{5.10}$$

Using Equations 5.9 and 5.10, throughout the range of permissible servo motor input angles, the torque about the stabilizing tail are plotted in Figure 5.3. Considering use of a servo-motor, the condition to maintain balance in such a TWMR is $\tau_{ct} = -\tau_{hld}$, where τ_{hld} was first briefly introduced in Section 4.2.2. The maximum holding-torque occurs at the input angle θ_3 which results in the tail's *end effecter* (that part making contact with the ground - shown here as a ball) being furthest from the system's COG. This occurs around $\theta_3 \approx 7.5°$.

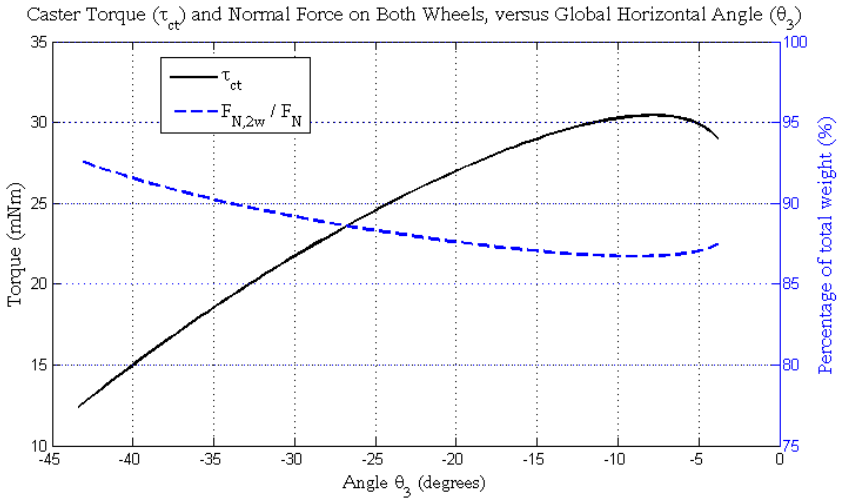

Figure 5.3: Calculated moment about the robot's tail and the percentage of the total normal force on both wheels, versus permissible input angles (measured from the global horizontal).

At the angle where τ_{ct} and F_{ct} are maximum, F_w will be at a minimum (as shown by the dashed blue curve). Referring back to Figure 5.2, only one wheel's normal force component is

shown in this side-view of the robot. So the notation F_{2w} is introduced to distinguish F_w for both wheels. Figure 5.3 is only valid however for the robot traversing a flat surface, so all forces and torques will change for different angles of inclination. Depending on the angle of declination as well as the robot's present speed, rotating the robot's COG (via actuating its tail by some degree) can actually help prevent tipping over (head-first).

5.2 Kinematics

Formulation of a two-wheeled mobile robot's kinematic model follows from the two-dimensional planar physics that govern differential-drive motion [25]. The robot's position within its environment is described in a Cartesian space, for both relative and absolute (or global) coordinates. Here relative coordinates refer to a local frame of reference, with axes attached to the robot as shown in Figure 5.4.

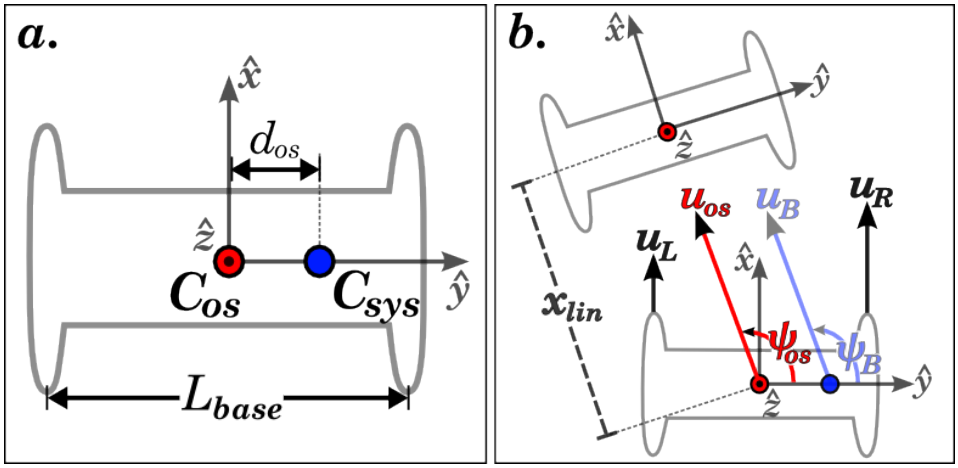

Figure 5.4: Top view of a TWMR. *Left*: Image ***a.*** illustrates using the Parallel-Axis theorem in a situation where the robot's COG (at C_{sys}) is not located at the robot's geometric center (at C_{os}). *Right*: Image ***b.*** shows the velocity vectors of each (left/right) wheel and their effective contributions to the robot's kinematics.

In general, a robot's COG is rarely located exactly at its geometric center (between its wheels). Knowing the robot's actual COG as well as L_{base}, the Parallel-Axis theorem can be applied to determine the equivalent mass moment of inertia at an arbitrary offset distance (d_{os}) from the actual COG. This relationship is summarized in Equation 5.11, where m_{tot} is the robot's total mass.

$$J_{os} = J_{cog} + m_{tot} \cdot {d_{os}}^2 \tag{5.11}$$

The illustration marked *a.* on the left side of Figure 5.4 depicts using the Parallel-Axis theorem in a situation where the equivalent COG (at C_{sys}) does not coincide with the robot's geometric center (shown here as C_{os}). So the total mechanical kinetic energy, defined in Equation 5.1, can be written either with respect to C_{sys} or C_{os}.

The robot's mechanical model in Pro/ENGINEER was used to determine how J_{cog} changes for a variable set of caster-tail input angles. Interpolating second and fourth-degree constant coefficient polynomial functions using this data (from the mechanical model), the results are illustrated in the left graph of Figure 5.5. The plot on the right shows J_{cog} before and after applying the Parallel-Axis theorem (Equation 5.11) to find J_{os}.

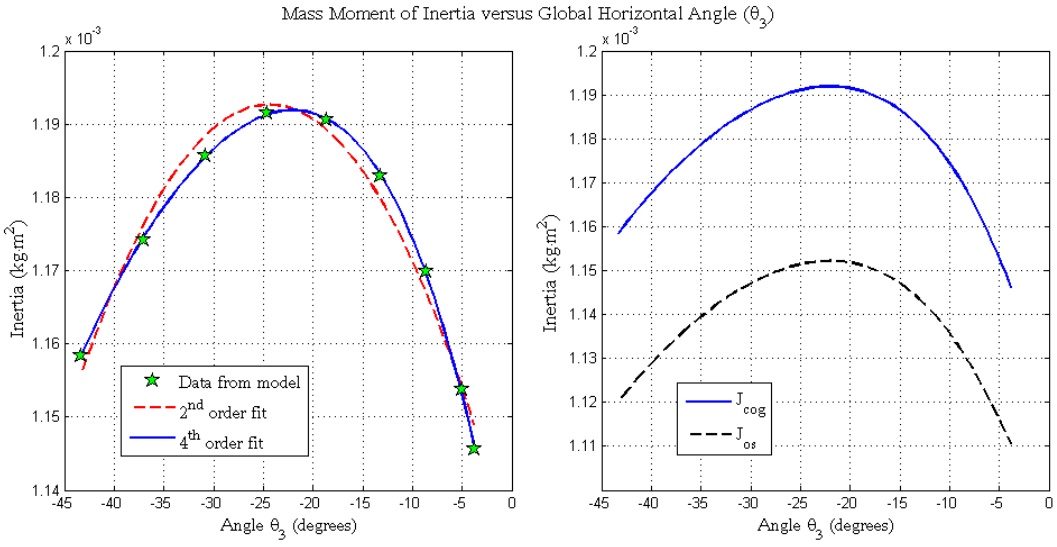

Figure 5.5: Robot's mass moment of inertia versus varying caster angle (measured from the global horizontal, θ_3). *Left*: Fitting second and fourth-degree polynomials to J_{cog} data from the robot's Pro/ENGINEER mechanical model. *Right*: Showing how the Parallel-Axis theorem shifts J_{cog} to J_{os}.

If there is no slippage at the wheel's point of contact with the ground, the kinematics and dynamics of the differentially driven robot can be simplified. For the specific system considered here, this is actually a reasonable assumption, considering the robot's weight and maximum output torque of the wheels' PMBDC motors. Imposing the *no slip* condition at the wheel's point of contact with the ground, simplifies transformation between rotational ($\omega_{R/L}$) and linear ($u_{R/L}$) velocity of left/right wheels to $u_{R/L} = r_w \cdot \omega_{R/L}$, where r_w is the wheel radius.

The robot's linear velocity u_{os}, and the change in its heading's orientation ψ_{os}, are found by substituting $(J_B, \psi_B, u_B) = (J_{os}, \psi_{os}, u_{os})$ into Equation 5.11. After some algebra, u_{os} and ψ_{os}

can be expressed as Equations 5.12 and 5.13, respectively.

$$u_{os} = \frac{1}{2 \cdot r_w} \cdot (u_R + u_L) \tag{5.12}$$

$$\psi_{os} = \frac{1}{L_{base}} \cdot (u_R - u_L) \tag{5.13}$$

The resultant efficiency $\eta_{K,em}$ can now be written as shown in Equation 5.14. Here it was assumed that both wheels have the same radius as well as rotational inertia (J_w). Note that J_w is the same as the load inertia J_L depicted in Figure 4.4.

$$\eta_{K,em} = \frac{1}{2 \cdot E_{K,in}} \cdot \left(J_{os} \cdot \psi_{os}^2 + J_w \cdot \left(\frac{u_R}{r_w} \right)^2 + J_w \cdot \left(\frac{u_L}{r_w} \right)^2 + m_{tot} \cdot u_{os}^2 \right) \tag{5.14}$$

The electromechanical power demanded by PMBDC motors was experimentally measured, integrated over small time increments, and factored in to the general mechanical kinetic energy required to establish a linear translational velocity u_{os}. This velocity was incrementally varied from a reasonably chosen minimum, to the maximum allowable value hard-coded in the robot's microcontroller firmware (approximately 520 mm/sec). Figure 5.6 graphs the measured electrical input power to both wheel motors onboard the TWMR robot described in Appendix B.2.1.

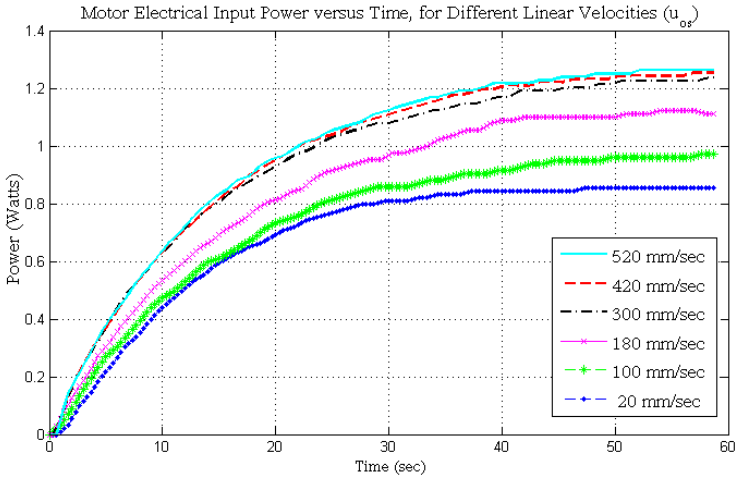

Figure 5.6: Electrical input power to PMBDC motors versus time, for various linear velocities.

Results have repeatedly shown that current drawn by the motors accounts for less than 5% of the total I_{dsg} from the battery. Almost every test evinced that power consumed by the onboard processor, active sensors (such as camera and video transmitter), and wireless communication peripherals were the driving factor contributing to battery depletion in the overall P_{dsg}.

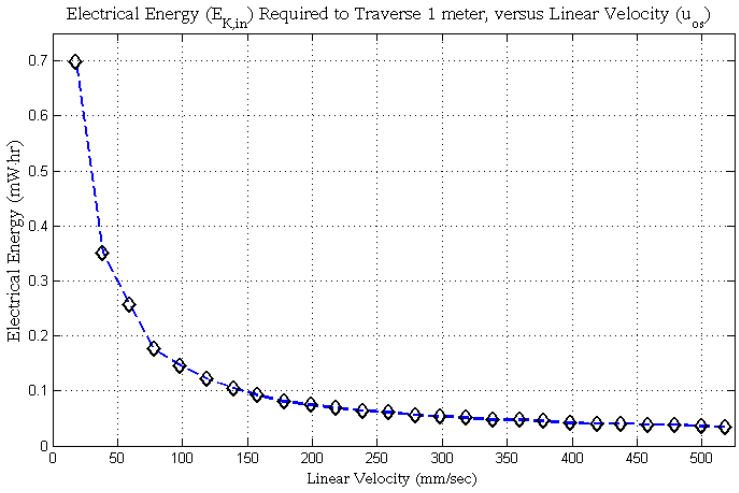

Figure 5.7: Linear velocity (u_{os}) versus electrical energy required to displace robot (detailed in B.2.1) by 1 meter.

Figure 5.7 shows the measured u_{os} for the robot detailed in Appendix B.2.1 versus electrical input energy $E_{K,in}$ demands in traversing 1 meter (on flat terrain) at this speed. Clearly more energy is required to start moving, as friction losses are larger at smaller velocities.

Chapter 6

Embedded Fuel-Gauging in Mobile Robots

A high-level block diagram overviewing the main components within a hardware-based fuel-gauge is depicted in Figure 6.1. The analog front-end (abbreviated AFE) IC serves multiple purposes in this circuit. Its internal LDO regulator powers the fuel-gauge IC, the secondary over-voltage protection IC, as well as several analog and digital 3.3V sub-circuits. Acting as the slave within the overall circuit, it reacts to overvoltage (and undervoltage) conditions, and responds to high frequency impulsive events (such as momentary current shorts and switching transients) across R_{sns}. Thresholds for a variety of cell parameters can be set and fine-tuned via the chipset's programmable internal registers.

Notice the emphasis placed on use of four-terminal *Kelvin connections* across R_{sns} and each individual cell. Defining separate low-current paths for analog signals measured, if applied properly in a PCB design, can improve the measured signal's noise-immunity (from high-current rails) and also reduces errors in measurements due to distributed line parasitics.

The P-channel power MOSFETs U_{chg} and U_{dsg} are controlled by the AFE to allow charging and discharging, respectively. A common-drain arrangement between MOSFETs allows unidirectional current flow when charging or discharging a battery, by turning on only U_{chg} or U_{dsg}, respectively. This however forces current to flow through the off MOSFET's body-diode, which is generally less efficient and can result in excess heat generation. Thus to promote user saftey by increasing device reliability and its functional lifetime, both MOSFETs are turned on regardless whether charging or discharging.

Another role of the AFE is to balance each cell within the pack when charging [54]. However, since the AFE IC's internal by-pass resistance can only sink a limited amount of current, this will increase the time required to adjust cell imbalances. While this is not an issue for smaller

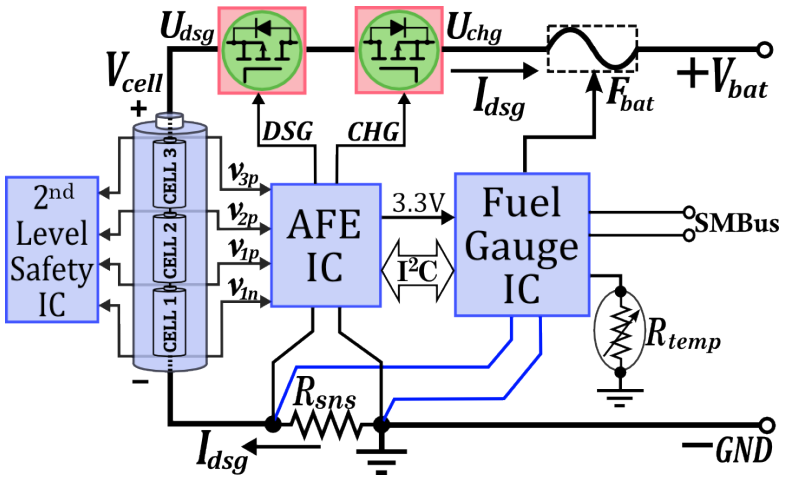

Figure 6.1: Diagram overviewing a hardware-based fuel-gauge chipset, shown with internal NTC thermistor (R_{temp}) and final-tier protective safety fuse (F_{bat}).

capacity batteries, balancing high capacity cells can be problematic - since large variations may not be adjusted in the alloted time before charging termination. To address this issue, an external (to the AFE) accelerated balancing circuit was realized and integrated into two of the three custom PCB designs (see Appendix B), for use in high capacity battery packs. This particular design also allows the AFE IC to still maintain control of (enabling and disabling) cell balancing.

This fuel-gauge chipset was physically realized on three custom PCBs, for four very different systems. However all three PCBs can easily be modified, with a few minor adjustments in both hardware and software, to allow interchanging boards between these mobile robots. The designs presented in this thesis offer a custom battery fuel-gauging solution not only for the specific systems described here, but also for future designs of robotic platforms that utilize similar battery chemistries.

Since robots do not all demand the same peripheral components and onboard devices, in an effort to promote a scalable means to track battery dynamics in other system designs, the entire fuel-gauge circuit was layed out on a seperate PCB. Shown in Figure B.2, are all four layers that make up this board (which is set up for a $3_S Y_P$ wired pack). This design was successfully applied in several different custom mobile robotic platforms. Specifically for the 1320 mAh $3_S 1_P$ LiPB packs in Explorer robot (introduced in Appendix B.2.1), and the high capacity 7600 mAh $3_S 4_P$ LiPB packs in the mobile docking and recharging station (MDS); detailed in Appendix B.2.2 - which is the same LiPB pack and fuel-gauge PCB set-up employed in another custom platform, the micro-Vision robot (but will not be discussed in this thesis).

To illustrate the modularity of the custom designed $3_S Y_P$ fuel-gauge PCB, it was reconfigured

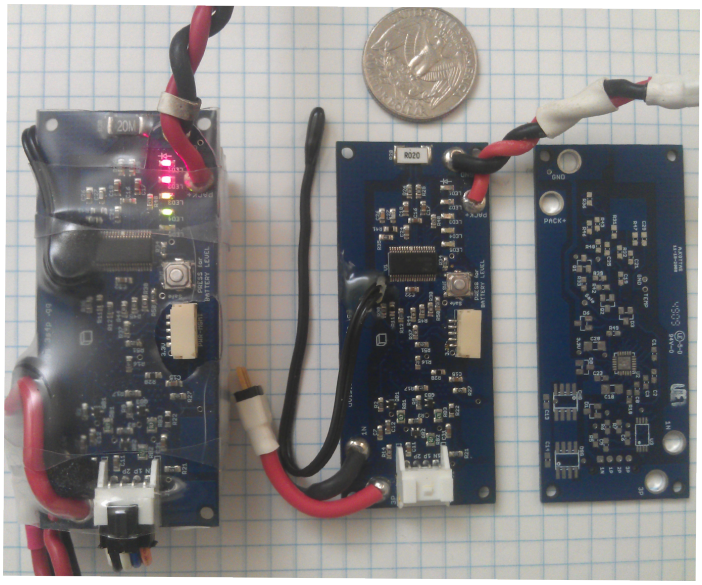

Figure 6.2: From right to left: bottom side of the fabricated fuel-gauge PCB (shown unpopulated); top side of the same PCB, but populated with components; the same board used with a 3_S1_P LiPB pack.

and applied to a 1320 mAh 3_S1_P LiPB pack, as depicted in Figure 6.2. Shown (from right to left), is the bottom side of the fabricated fuel-gauge PCB (corresponding to the CAD drawing in Figure B.2), the top side layer of a populated board, and the final product mounted atop the smaller capacity 1320 mAh 3_S1_P LiPB pack.

The PCB in Figure B.2 was slightly modified in both hardware and software serving a proof-of-concept design to accomodate use in 2_SY_P packs. After extensive testing evinced favorable results, a slightly smaller PCB was designed. So despite the fact that the previous version PCB could easily have been used, this new system's size and weight requirements posed some additional unavoidable constraints. Thus a different PCB was designed for the 1900 mAh 2_S1_P LiPB pack onboard the Aqua-Pod robot (see Section B.2.3). Each of the PCB's four layers are shown in Figure B.3.

From right to left, Figure 6.3 depicts the bottom side of the fabricated bare PCB (corresponding to the CAD drawing in Figure B.3), the top side layer of a populated board, and the final product as it attaches to the 1900 mAh 2_S1_P LiPB pack.

Besides their obvious use as a fuel-gauge and battery monitor, these PCBs also serve to quantify a system's performance by logging data from the fuel-gauge, which can greatly simplify characterizing a system's power consumption. For example, measurements taken while charging three Explorer robots, described in Appendix B.2.1, onboard the MDS (see Appendix B.2.2). Here all three robots, as well as the docking station's battery, are equipped with a fuel-gauge

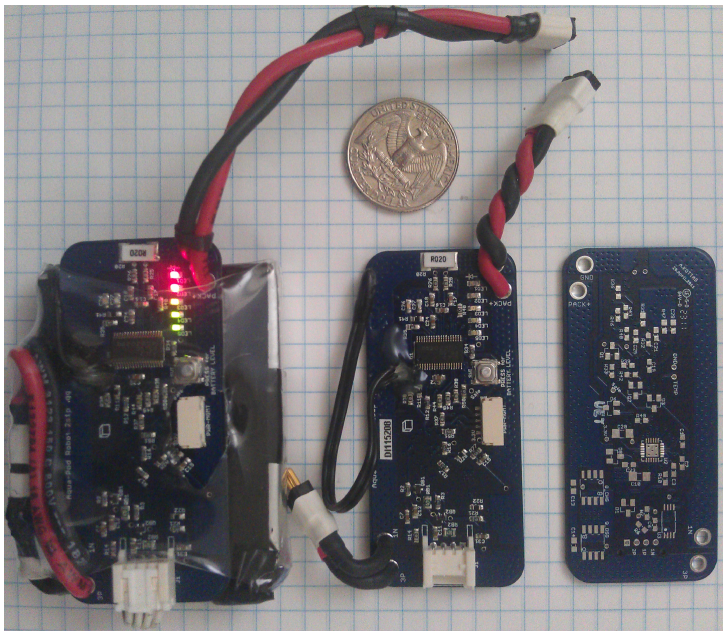

Figure 6.3: From right to left: back side of the fabricated (bare) fuel-gauge PCB; top side of the same PCB, but populated with components; the 2_S1_P LiPB pack with fuel-gauge PCB mounted on top.

PCB; from which logged data was extracted from all four systems for performance analysis.

Figure 6.4 profiles the power measured from the MDS's 7600 mAh 3_S4_P LiPB pack, while charging three Explorer robots at a 1·C rate - from almost empty to full. It was observed in experiments that loading three robots into the MDS, proceeding to charge all robots from approximately SoC = 10% (or less) to full, and then unloading every robot afterwards, resulted in completely depleting a fully-charged 7600 mAh pack. Thus, to serve any practical purpose, the MDS must be capable of UPS operation, to switch between its available batteries in order to service more than just three robots - which is only half its carrying capacity. The effects from loading and unloading robots are observed at the very left and right of this plot.

During a different test, two Explorer robots were loaded, fully-charged at a 1·C rate, then unloaded from the MDS. The MDS's 7600 mAh 3_S4_P LiPB pack's discharge power and remaining charge capacity measured during this experiment is shown in Figure 6.5.

Another unique application of the fuel-gauge PCB is demonstrated in an early design version of the Aquapod robot (see Appendix B.2.3). Figure 6.6 shows the internals of the Aquapod robot. This photograph was taken well before the 2_SY_P PCB was fabricated, The 3_SY_P fuel-gauge PCB (the dashed circled area in red, on the very right) is configured for use with a 2_S1_P LiPB pack in this early version of the Aquapod robot. The solid line circled area (towards the middle of 6.6)

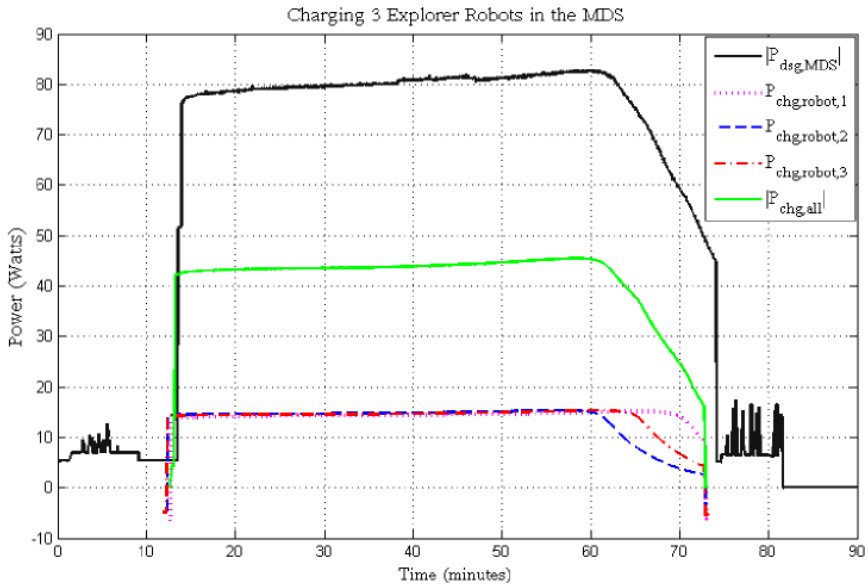

Figure 6.4: Tracking the MDS battery's power consumption, as well as all three Explorer robots being charged inside the MDS.

indicates the other custom circuit board that makes up the Aquapod robot (see Figure B.4) - which I designed with another graduate student.

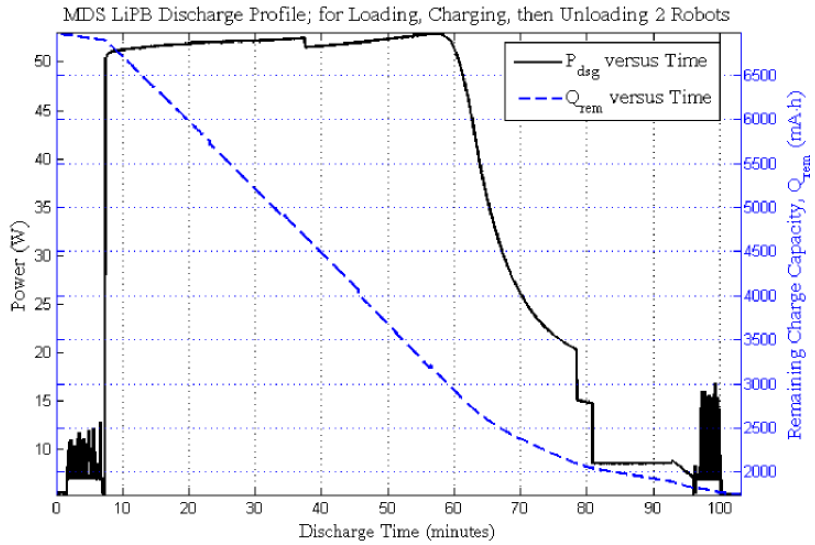

Figure 6.5: Tracking the MDS battery's power consumption and remaining charge capacity; as it loads, charges (at 1·C), then unloads two Explorer robots.

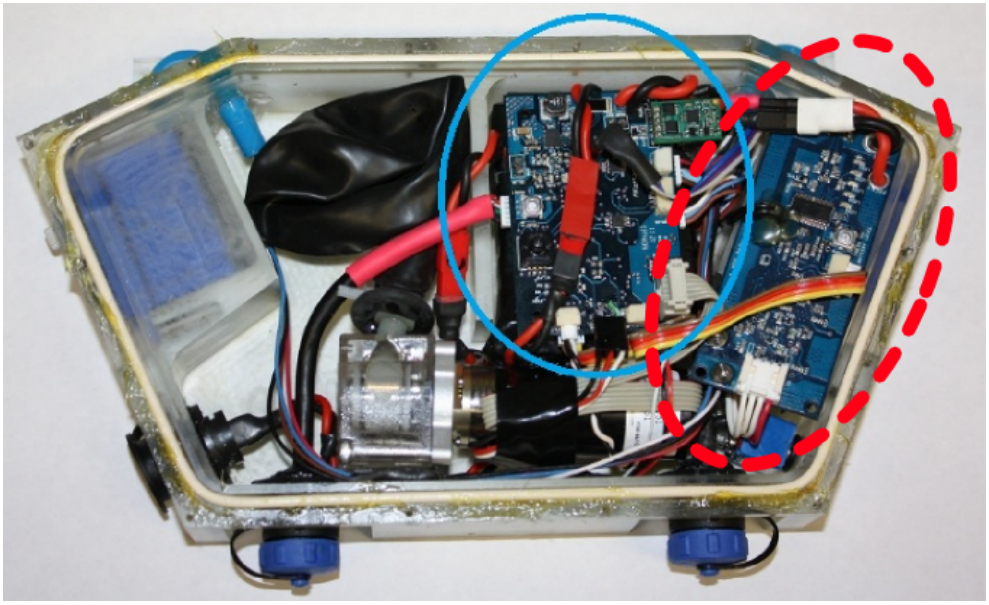

Figure 6.6: The $3_S Y_P$ fuel-gauge PCB (the dashed circled area in red, on the very right) is configured for use with a $2_S 1_P$ LiPB pack in this early version of the Aquapod robot. The other circled area is the other custom PCB onboard the Aquapod robot - see Figure B.4.

Chapter 7

Conclusions

In hindsight, this work has provided a preliminary assessment to several issues often overlooked in kinematic and dynamic analysis of miniature mobile robotic systems. We have seen how a battery's operating profile can influence the overall efficiency of a mobile robot during normal use, as well as the power demands from various peripheral components during normal operation.

A versatile fuel-gauging chipset was incorporated into three small custom PCB designs, and in turn applied across several robotic systems. These PCBs have been (and continue to be) successfully applied in many mobile robots (see Appendix B). Designs exhibited flexibility, in that they allowed recycling of the same circuit in five very different systems, with minimal modification. This was done by simply redefining a table of cell impedances and system operating characterstics in the hardware IC's flash memory. The embedded fuel-gauge system allows accurate measurement of percentage in power reduction in a robot's various onboard components. In addition, the fuel-gauge PCBs that were designed served to assist with performance testing during initial phases of developing new robotic platforms, as well as for dynamics characterization of many devices.

7.1 Future Work Expansions

The present servo-motor controlled caster-arm design continuously "burns" power. To reduce power consumption and still enable control of the robot's pitch (angle about the lateral axis), the robot's current servo-motor may be retrofitted with either a self-locking mechanism or the servo-motor substituted with a miniature linear actuator. In addition, the power dynamics resulting from variable surface inclinations as well as different terrain can be assessed to evaluate an optimum robot pose and similarly an optimal motion plan. Furthermore, the dynamic (in contrast to only static) losses due to the actuating tail's position during rolling motion can be

determined. Thermal characteristics can be investigated to further robustify our analysis.

Implementing an adaptive algorithm to infer changing battery cycling patterns can provide a more accurate measure of E_{fcc}. Contrast to the present implementation, which fixes a E_{rem} threshold whereby to deduce whether the battery has incurred one cycle-count in the discharge direction, an adaptive scheme can allow variations in this threshold. This idea stems from the example of (dis)charging a portable device, such as a cellular phone. Rarely does one wait until their mobile phone deads before recharging. Usually when a battery's SoC falls below 50% and a charger is within arms-reach, most will opt to recharge. Now assume that a battery's cycle-count threshold is defined at SoC = 25%, but is currently at SoC = 28% when someone decides to connect its charger. Notice that the present cycle (albeit not quite a full one) would not be counted. If this were to happen often, it would induce formidable error in dynamic parameter measurements and estimates, and further get propagated over time through the calculation of SoH. Hence a more robust algorithm would account for both *full* cycles experienced, as well as the number of such *pseudo* cycles accumulated.

In addition, the concepts here can be used in higher-level algorithms, such as applied task management. This can assist in developing heuristics to addresses the misappropriation of available onboard resources in mobile robotics, and in teams thereof, such as the work of [6] which serves the inspiration for this thesis.

References

[1] Marvel Semiconductor Inc. Marvell pxa270 processor: Electrical, mechanical, thermal specification. Product Specifications, Apr 2009.

[2] Saehan-Enertech Inc. Technical information of spb605060h4 (1900mah). Product Specification, Dec 2004.

[3] Murata Power Solutions Inc. *Okami* okr series adjustable output 6-amp sip-mount dc/dc converters. Product Datasheet, Mar 2011.

[4] Ian T. Burt, Andrew Drenner, Casey Carlson, Apostolos D. Kottas, and Nikolaos Papanikolopoulos. Impact orientation invariant robot design: an approach to projectile deployed robotic platforms. In *Proceedings of the 2006 IEEE International Conference on Robotics and Automation*, pages 2878–2883, 2006.

[5] Saehan-Enertech Inc. Technical information of spb603462h1 (1320mah). Product Specification, Apr 2005.

[6] Andrew William Drenner. *A Framework for Distributed Mobile Robotics*. PhD thesis, University of Minnesota, Department of Computer Science, Minneapolis, MN, USA, 2009.

[7] David Linden and Thomas B. Reddy. *Handbook of Batteries*. McGraw-Hill, New York, 3rd edition, 2005.

[8] William Ross and Peter Budney. Development of a battery runtime prediction algorithm and a method for determining its accuracy. In *Proceedings of the 17th International Telecommunications Energy Conference*, pages 277–283, 1995.

[9] P. Rong and M. Pedram. An analytical model for predicting the remaining battery capacity of lithium-ion batteries. *IEEE Transactions on VLSI Systems*, 14(4):441–451, May 2006.

[10] K. C. Syracuse and W. D. K. Clark. A statistical approach to domain performance modeling for oxyhalide primary lithium batteries. In *Proceedings of the 12th Annual Battery Conference on Applications and Advances*, pages 163–170. IEEE Press, 1997.

[11] L. Benini, G. Castelli, A. Macii, E. Macii, M. Poncino, and R. Scarsi. Extending lifetime of portable systems by battery scheduling. In *Proceedings of the Design, Automation and Test in Europe Conference and Exhibition*, pages 197–201, Mar 2001.

[12] T. L. Martin. *Balancing Batteries, Power and Performance: System Issues in CPU Speed-Setting for Mobile Computing*. PhD thesis, Department of Electrical and Computer Engineering, Carnegie Mellon University, 1999.

[13] H. J. Bergveld, W. S. Kruijt, and P. H. L. Notten. Electronic-network modeling of rechargeable NiCd cells and its application to the design of battery management systems. *Journal of Power Sources*, 77(2):143–158, 1999.

[14] J. S. Newman. *Electrochemical Systems*. Prentice-Hall, Englewood Cliffs, New Jersey, 2nd edition, 1991.

[15] Ravishankar Rao, Sarma Vrudhula, and Daler Rakhmatov. Analysis of discharge techniques for multiple battery systems. In *Proceedings of the 2003 International Symposium on Low Power Electronics and Design*, pages 277–283, Seoul, Korea, Aug 2003.

[16] T. F. Fuller, M. Doyle, and J. S. Newman. Relaxation phenomena in lithium-ion-insertion cells. *Journal of the Electrochemical Society*, 141:982–990, Apr 1994.

[17] Gregory L. Plett. Extended kalman filtering for battery management systems of lipb-based hev battery packs: Part 2. modeling and identification. *Journal of Power Sources*, 134(2):262–276, 2004.

[18] Anahita Banaei. *Real Time Condition Monitoring of Chemical Batteries*. PhD thesis, The University of Texas at Arlington, August 2010.

[19] M. Ragsdale, J. Brunet, and B. Fahimi. A novel battery identification method based on pattern recognition. In *Vehicle Power and Propulsion Conference (VPPC), IEEE*, pages 1–6, Sept 2008.

[20] Osman S. Unsal and Israel Koren. System-level power-aware design techniques in real-time systems. *Proceedings of the IEEE*, 91(7):1055–1069, 2003.

[21] Keith J. OHara, Ripal Nathuji, Himanshu Raj, Karsten Schwan, and Tucker Balch. Autopower: Toward energy-aware software systems for distributed mobile robots. In *IEEE International Conference on Robotics and Automation*, 2006.

[22] David C. Snowdon, Etienne Le Sueur, Stefan M. Petters, and Gernot Heiser. Koala: a platform for os-level power management. In *EuroSys '09: Proceedings of the 4th ACM European conference on Computer systems*, pages 289–302, New York, NY, USA, 2009. ACM.

[23] Yung-Hsiang Lu Yongguo Mei, C. S. George Lee, and Y. Charlie Hu. Energy-efficient mobile robot exploration. In *Proceedings of the 2009 IEEE International Conference on Robotics and Automation*, 2006.

[24] C.H. Kim and B.K. Kim. Minimum-Energy Motion Planning for Differential-Driven Wheeled Mobile Robots. *Journal of Intelligent and Robotic Systems*, 49(4):367–383, 2007.

[25] C.H. Kim and B.K. Kim. Minimum-Energy Translational Trajectory Generation for Differential-Driven Wheeled Mobile Robots. *Journal of Intelligent and Robotic Systems*, 49(4):367–383, 2007.

[26] W. Zhang, Y.H. Lu, and J. Hu. Optimal Solutions to a Class of Power Management Problems in Mobile Robots. *Automatica*, 45(4):989–996, 2009.

[27] Andrew Drenner, M.A. LaPoint, Ian T. Burt, K. Cannon, C. Hays, Apostolos D. Kottas, and N. Papanikolopoulos. Increasing the scout's effectiveness through local sensing and ruggedization. In *Proceedings of the 2004 IEEE International Conference on Robotics and Automation*, volume 2, pages 1406–1411, Apr 2004.

[28] W. Grey Walter. *The Living Brain*. W.W. Norton, New York, 1963.

[29] Yasushi Hada and Shin'ichi Yuta. A first experiment of long term activity of autonomous mobile robot - result of repetitive base-docking over a week. In *Proceedings of the ISER 2000 Seventh International Symposium on Experimental Robotics*, pages 235–244, Dec 2000.

[30] Milo C. Silverman, Dan Nies, Boyoon Jung, and Gaurav S. Sukatme. Staying alive: A docking station for autonomous robot recharging. In *Proceedings of the 2002 IEEE International Conference on Robotics and Automation*, pages 1050–1055, Washington, DC, May 2002.

[31] D. F. Hougen, J. C. Bonney, J. R. Budenske, M. Dvorak, M. Gini, D. G. Krantz, F. Malver, B. Nelson, N. Papanikolopoulos, P. E. Rybski, S. A. Stoeter, R. Voyles, and K. B. Yesin. Reconfigurable robots for distributed robotics. In *Government Microcircuit Applications Conf.*, pages 72–75, Anaheim, CA, Mar 2000.

[32] Pawel Zebrowski and Richard Vaughan. Recharging robot teams: A tanker approach. In *Proceedings of the International Conference on Advanced Robotics (ICAR)*, Seattle, Washington, July 2005.

[33] Trung Dung Ngo, Hector Raposo, and Henrok Schioler. Being sociable: Multirobots with self-sustained energy. In *Proceedings of the 15th Mediterranean Conference on Control and Automation*, Athens, Greece, July 2007.

[34] Casey Carlson, Andrew Drenner, Ian Burt, and Nikolaos Papanikolopoulos. Modular mobile docking station design. In *Proceedings of the IEEE/RSJ International Conference on Intelligent Robot Systems*, 2006.

[35] Yevgen Barsukov. Theory and implementation of impedance track battery fuel-gauging algroithms in bq20z8x product family. *Power Management Articles, Texas Instruments Inc.*, 2005.

[36] V. Pop, H.J. Bergveld, J.H.G. Veld op het, P.P.L. Regtien, D. Danilov, and P.H.L. Notten. Modeling battery behavior for accurate state-of-charge indication. *Journal of the Electrochemical Society*, 153(11):A2013–A2022, 2006.

[37] Yevgen Barsukov and Bernd Krafthöfer. Predicting runtime for battery fuel-gauges. *Power Management DesignLine, Texas Instruments Inc.*, Aug 2005.

[38] Yevgen Barsukov. Cell-type specific settings for cell imbalance permanent failure thresholds. Application report, Texas Instruments Inc., Sept 2007.

[39] Yevgen Barsukov. Challenges and solutions in battery fuel-gauging. In *Power Management Workbook*. Texas Instruments Inc., 2004.

[40] V. Pop, H.J. Bergveld, D. Danilov, P.P.L. Regtien, and P.H.L. Notten. *Battery Management Systems: Accurate State-of-Charge Indication for Battery-Powered Applications*. Philips Research Book Series 9. Springer Verlag, London, 2008.

[41] Yevgen Barsukov. Battery selection, safety, and monitoring in mobile applications. *Power Management Articles, Texas Instruments Inc.*, 2006.

[42] Texas Instruments Inc. Power management ic for li-ion powered systems (rev. b). Product Datasheet, Jul 2007.

[43] Texas Instruments Inc. Pt78st100 series 1.5 amp positive step-down integrated switching regulator. Product Datasheet, Jun 2000.

[44] Jason Arrigo. Input and output capacitor selection. Application report, Texas Instruments Inc., Feb 2006.

[45] Bob Wolbert. *Micrel's Guide to Designing with Low-Dropout Voltage Regulators*. Micrel Semiconductor, Dec 1998.

[46] Terry Cleveland. A method to determine how much power a sot23 can dissipate in an application. Application note, Microchip Technology Inc., 2001.

[47] N. Mohan. *Electric Drives: An Integrative Approach*. MNPERE, Minneapolis, The, 2003.

[48] Mickey McClure. A simplified approach to dc motor modeling for dynamic stability analysis. Application report, Texas Instruments Inc., July 2000.

[49] Philips Semiconductors. Motor control power semiconductor applications, 1994.

[50] Inc. Maxon Motors. Pwm-scheme and current ripple of switching power amplifiers. Company White Paper Publication, Aug 2000.

[51] P.N. Vaidya, M.H. Khan, B. Morgan, and P. Sakarda. System level adaptive framework for power and performance scaling on intel reg; pxa27x processor. In *Acoustics, Speech, and Signal Processing, 2005. Proceedings. (ICASSP '05). IEEE International Conference on*, volume 5, pages 657–660, Mar 2005.

[52] Albert A. Smith. *Radio Frequency Principles and Applications: The Generation, Propagation, and Reception of Signals and Noise*. Wiley-IEEE Press, 1st edition, 1998.

[53] Neil Sclater and Nicholas Chironis. *Mechanisms and Mechanical Devices Sourcebook*. McGraw-Hill Professional, 2001.

[54] Sihua Wen. Cell balancing buys extra run time and battery life. *Power Management, Analog Applications Journal*, 2009.

[55] Maxwell Walter, Monica Anderson, Ian Burt, and Nikolaos Papanikolopoulos. The design and evolution of the eROSI robot. *Proceedings of the 2007 IEEE International Conference on Robotics and Automation*, Apr 2007.

[56] Apostolos Kottas, Andrew Drenner, and Nikolaos Papanikolopoulos. Intelligent power management: Promoting power efficiency in teams of mobile robots. In *Proceedings of the 2009 IEEE International Conference on Robotics and Automation*, pages 2459–2464, Kobe, Japan, May 2009.

[57] Lingyin Zhao. Implementations of battery charger and power-path management system using bqswitcher^{TM}. Application report, Texas Instruments Inc., 2006.

[58] Andrew Drenner and Nikolaos Papanikolopoulos. Docking station relocation for maximizing longevity of distributed robotic teams. In *Proceedings of the IEEE International Conference on Robotics and Automation*, pages 2436–2441, Orlando, FL, USA, May 2006.

[59] Benchmarq Microelectronics Inc., Duracell Inc., Energizer Power Systems, Intel Corporation, Linear Technology Corporation, Maxim Integrated Products, Mitsubishi Electric Corporation, National Semiconductor Corporation, Toshiba Battery Co., Varta Batterie AG. *Smart Battery System Manager Specification*, Dec 1998.

[60] Benchmarq Microelectronics Inc., Duracell Inc., Energizer Power Systems, Intel Corporation, Linear Technology Corporation, Maxim Integrated Products, Mitsubishi Electric Corporation, National Semiconductor Corporation, Toshiba Battery Co., Varta Batterie AG. *Smart Battery Charger Specification*, Dec 1998.

[61] Myounggu Park, Xiangchun Zhang, Myoungdo Chung, Gregory B. Less, and Ann Marie Sastry. A review of conduction phenomena in li-ion batteries. *Journal of Power Sources*, 195(24):7904–7929, 2010.

[62] Benchmarq Microelectronics Inc., Duracell Inc., Energizer Power Systems, Intel Corporation, Linear Technology Corporation, Maxim Integrated Products, Mitsubishi Electric Corporation, National Semiconductor Corporation, Toshiba Battery Co., Varta Batterie AG. *Smart Battery Data Specification*, Dec 1998.

Appendix A

Referenced Calculations

To promote coherent presentation of information in this thesis, specific details in various discussions throughout chapters have been redirected to this appendix. These are mostly related to topics surrounding DC motors and wireless RF signal propagation.

A.1 DC Motors

Table A.1 defines all DC motor related parameters and variables used throughout this thesis. The specific PMBDC motors described in Section 4.2.1 and used onboard the robot detailed in Appendix B.2.1, are illustrated in Figure A.1.

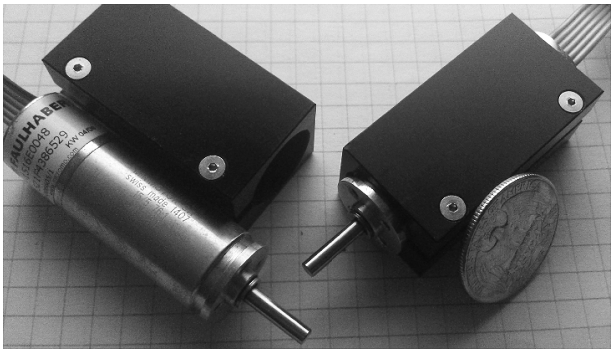

Figure A.1: Actual PMBDC micro-motors used in the Explorer robot (detailed in Appendix B.2.1) along with their custom housing mounts.

Having found the input and output power relation in Section 4.2, let's see how some of these parameters factor into losses acrued in electromechanical power conversion. For example, operating PMBDC motors at very small velocities results in higher losses, since the motor's

starting torque is much higher than that during normal operation. This was seen in Figures 5.6 and 5.7.

Variable Symbol	Units	Definition
$f_{s,pwm}$	kHz	PWM drive signal frequency
$T_{s,pwm}$	sec	PWM signal time period (equal to $1/f_{s,pwm}$)
d_A	dimension-less	Duty cycle of applied PWM drive signal
V_a	V	Applied armature voltage
V_ω	V	Counter-EMF voltage (induced in the motor)
I_a	A	Motor armature current
$I_{a,0}$	A	Motor's no-load current
Δi_a	A	Armature (peak-to-peak) ripple current
k_ω	V·sec/rad	Back-EMF constant of the motor
k_τ	N·m/A	Torque constant of the motor
ω_m	rad/sec	Rotational velocity of the motor
τ_m	N·m	Motor's mechanical output torque
$\tau_{G,out}$	N·m	Motor gearhead output torque
τ_L	N·m	Load torque at output shaft
R_a	Ω	Armature resistance
L_a	μH	Motor armature inductance
C_ω	F	Motor equivalent (analogous) electrical capacitance
J_m	kg·m^2	Rotational inertia of the motor
f_m	N·m·sec/rad	Coefficient of viscous damping (proportional to ω_m)
$T_{m,elec}$	sec	Motor's electrical time-constant (defined as L_a/R_a)
$T_{m,mech}$	sec	Motor's mechanical time-constant
η_m	dimension-less	Motor (power) efficiency
η_G	dimension-less	Gearbox (power) efficiency

Table A.1: Definitions for DC Motor variables and electromechanical parameters

When determining the power consumption of a DC motor, the root mean square (or RMS) must be used to effectively, and moreover correctly, calculate the total I_a (and include the effects from Δi_a). Since armature current is directly proportional to τm produced by the motor, torque must also be measured in RMS.

I_a is not the same as the supplied current (I_{dcm}) to the motor circuit(s), unless the H-bridge driver IC operates 100% efficiently. For a supply voltage equal to V_{bat}, the relationship between these two currents is shown in Equation A.1, where the fractional voltage is usually called the *overdrive ratio*.

$$I_{dcm} = I_a \cdot \frac{V_a}{V_{bat}} \tag{A.1}$$

Consider a DC motor with electrical time constant $T_{m,elec}$, driven by a PWM signal with switching period $T_{s,pwm}$, as defined in Table A.1. If $T_{m,elec} \gg T_{s,pwm}$, then the DC steady-state I_a will approach an (almost) ripple-free, and approximately constant DC current. In the opposite

case, where $T_{m,elec} \ll T_{s,pwm}$, the I_a waveform will closely follow the applied V_a square-wave. This is best explained pictorally. The I_a waveform is graphed in Figure A.2 using four different $f_{s,pwm}$ values, for d_A increasing (from top to bottom), and $V_a = 12$V. Notice that the $\hat{y}$-axis is *not* in units of mA, but is instead normalized with respect to the peak I_a value.

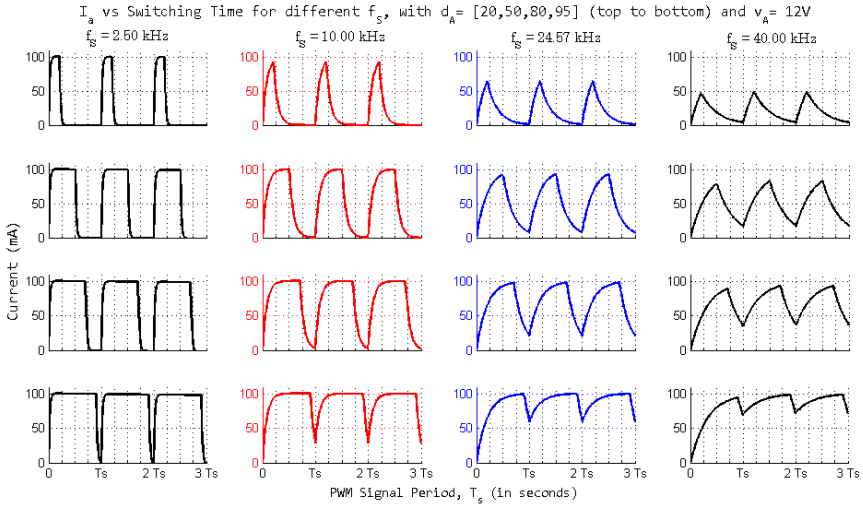

Figure A.2: Armature current I_a waveform graphed against PWM switching time period ($T_{s,pwm}$, but written as T_s for short). Each row of graphs corresponds to a single duty cycle, which is shown increasing (from top to bottom row) by discrete steps $d_A = \{20, 50, 80, 95\}$. Similarly, each column represents a single PWM switching frequency, increasing (from left to right) in discrete steps $f_{s,pwm} = \{2.50, 10.0, 24.57, 40.0\}$ kHz, drawn in black, red, blue, and (again) black, respectively.

The motor PWM driver IC's integrated H-bridge is shown, as it attaches to the motor's terminals, in Figure A.3. Since integrated motor drivers contain many internal subcomponent blocks (FET gate drive signals, switching control logic, filters, and many others), for the sake of clarity and simplicity, internal peripherals irrelevant to this discussion were intentionally omitted. Similarly, stray leakage currents, such as the one that would go through the body-diode of $U_{P,2}$, as well as the IC's quiescent (ground) current are not included. If such leakage and stray current effets are neglected, then switching losses in the driver's power MOSFETs will be proportional to the square of their drain-to-source current (I_{DS}) and on-resistance ($R_{DS,on}$).

The influence of $R_{DS,on}$, in terms of the overall equivalent motor circuit's operation can be seen in the right portion of Figure A.3. Notice that the return path for I_a is not connected directly to ground, but is instead seperated by an $R_{DS,on}$ element.

The voltage drop $V_{DS,on}$ attributed to each $R_{DS,on}$ will result in a slightly different V_a than expected (from the theoretical $V_a = d_A{\cdot}V_{bat}$). Noting the voltage dividers within this circuit,

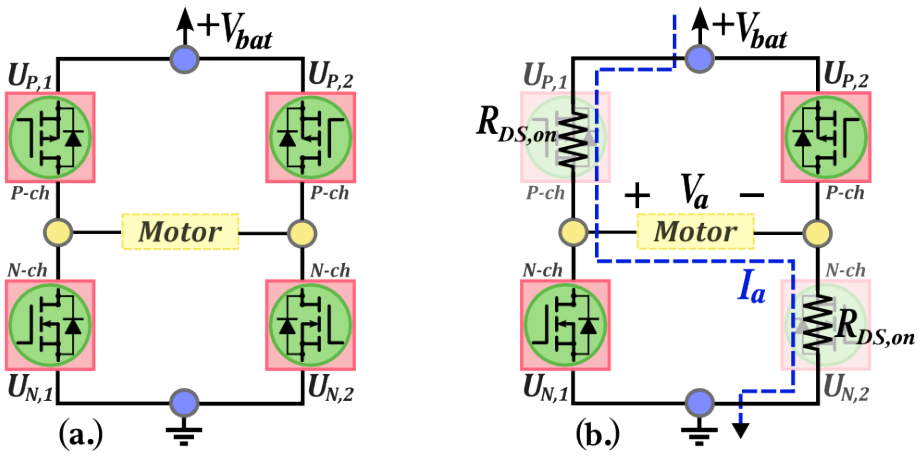

Figure A.3: *Left*: PWM driver IC's integrated H-bridge circuit, shown as it connects to the motor's terminals. *Right*: Simplified illustration of internal MOSFETs $R_{DS,on}$ during forward (first quadrant) motor operation.

the power loss in each $R_{DS,on}$ element (abbreviated $P_{DS,on}$) can be written as Equation A.2.

$$P_{DS,on} = \underbrace{d_A \cdot V_{bat} \cdot \left(\frac{R_{DS,on}}{2 \cdot R_{DS,on} + (R_a + \jmath \cdot 2\pi f_{s,pwm} \cdot L_a)} \right)}_{V_{DS,on}} \cdot I_a \tag{A.2}$$

A closed-loop speed controller can be implemented for each motor using feedback encoders. Several manufacturers offer optical or magnetic encoders conveniently built in to the motor's casing, such as the motor shown in Figure A.1 - which uses the latter.

This specific encoder accepts a wide range of supply voltages, so it can be powered directly from V_{bat} or even a low power 5V supply rail. The encoder circuit comprises a frequency-to-voltage converter, fed to a comparator that is coupled to a voltage-controlled oscillator. The output signal is a 50% duty cycle square-wave, with fundamental frequency (f_{enc}, in Hz) proportional to the motor's ω_m (in rad/sec). This relationship is shown in Equation A.3, where N_{enc} defines the encoder's resolution (in units of encoder *ticks* per motor shaft revolution).

$$\boldsymbol{\omega_m} = \frac{2\pi \cdot \boldsymbol{f_{enc}}}{N_{enc}}. \tag{A.3}$$

A.2 RF Wireless Radios

Reception strength directly relates to the receiver's input power, or P_{RX}. Given transmit power P_{TX}, P_{RX} can be approximated via the Friis formula, shown in Equation A.4. This is a theoretical generalization describing the case where a transmitted signal is attenuated by only

free-space path loss, for transmitter and receiver antennas are seperated by distance d. Here antenna gains at the transmitter (G_{TX}) and receiver (G_{RX}) are expressed with respect to an isotropic radiator.

$$P_{RX} = G_{RX} \cdot G_{TX} \cdot P_{TX} \cdot \left(\frac{\lambda}{4\pi \cdot d} \right)^2 \tag{A.4}$$

If customizations are made to the transmitter and/or receiver antenna(s), then most likely there will be a line-load impedance mismatch. Unless appropriately compensated, this can lead to a vast decrease in system performance by increasing the reflection coefficient between antenna and receiver $\left|\Gamma_{RX/ant}\right|$ (or $|S_{11}|$, in terms of S-parameters), power efficiency, as well as reducing LOS range.

To show how some of these concepts can be applied to a small robot, the experimental test platform used in this section is the ruggedized mobile robot described in [4]. This system employs a miniature 75 MHz COTS radio receiver within its exterior titanium (Ti) shell, with only a small vertically-mounted monopole antenna (of length $\lambda/16$) pertruding to capture transmissions.

The left Smith chart in Figure A.4 shows this antenna's measured input impedance ($Z_{RX,ant}$), for a single carrier frequency $f_c = 75.57$ MHz, after adding a small segment coaxial feedline during measurements. Clearly adding the robot's exterior Ti shell shifts a once capacitive equivalent load impedance (residing in the bottom-half of the Smith Chart) to become inductive - in the top-half hemisphere on the Smith chart.

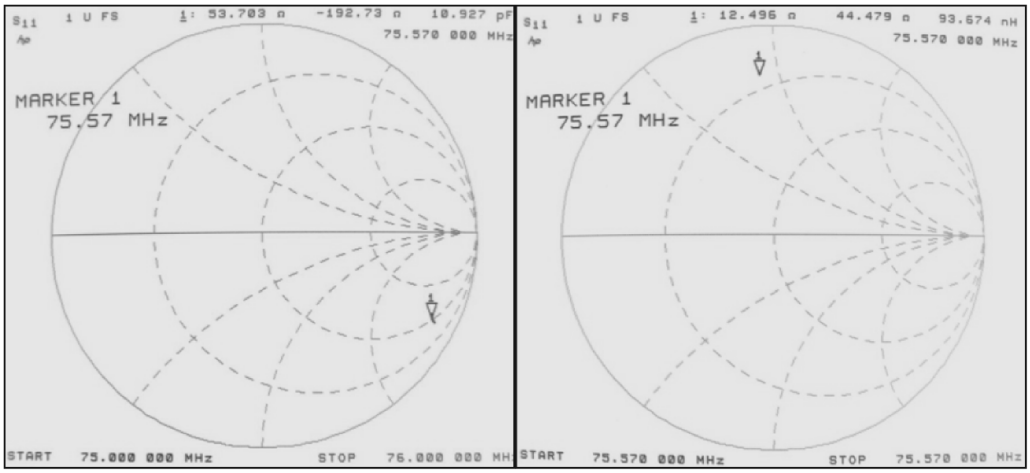

Figure A.4: $|S_{11}|$ measured with a VNA for a frequency sweep of 75–76 MHz, showing the equivalent $Z_{RX,ant}$ after adding a coaxial feedline cable connecting antenna and receiver input, on the Smith chart. *Left*: measurement taken without the robot's external Ti shell. *Right*: measurement taken after the robot's Ti outer shell has been added. All impedances are normalized with respect to $Z_0 = 50\Omega$. Measurement markers indicate $f_c = 75.57$ MHz.

Compensating for this impedance mismatch by adding a simple passive $L{\cdot}C$ matching network between antenna and receiver input, results in almost doubling the robot's LOS range to the transmitter. This is indicated in Figure A.5, which graphs the receiver's power at the device's input terminals with respect to its sensitivity. For this simulation, the path propagation model assumed for the mobile robot in [4] is a combination of LOS, reflected, and ground-wave modes of signal transmission and path losses.

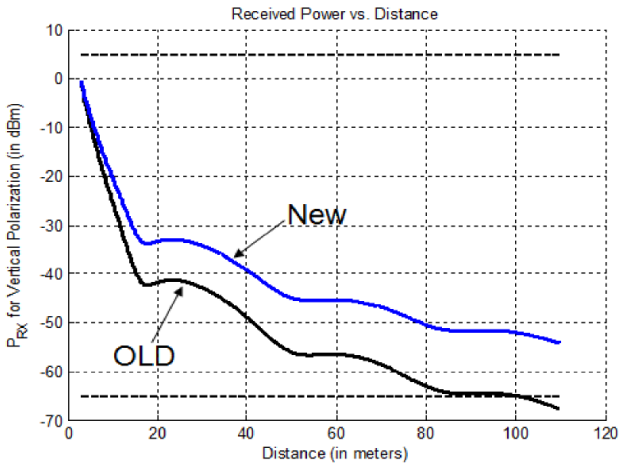

Figure A.5: Graph showing the increased D_{ant} by adding a third-order $L{\cdot}C$ matching network. The bottom (black) curve marked "OLD" and the upper (blue) curve marked "NEW," respectively illustrate P_{RX} before and after the addition of a matching network. Dashed lines represent receiver sensitivity bounds, where the lower dashed line defines the noise-floor for RF measurements.

Appendix B

Details of Systems Designed

Specifics regarding the experimental system set-up used in this work are described below. In this appendix, various details ommitted from prior sections, specifically regarding experimental setups, some of the designed robotic platforms, and the LiPB fuel-gauge PCBs that were introduced in Chapter 6.

B.1 Custom PCB and Hardware Design

Each PCB is fabricated on four-layer FR-4 boards (layers are sperarated by a 0.5 mm core), with 1-oz Cu-clad traces (maximum height 0.05 mm). Since these PCBs are relatively small and the circuits comprise many devices, real-estate is scarce. Hence it is difficult to inlude large ground planes for heat sinking in the design. So all unpopulated areas with higher current paths use many 10 mil thru-hole vias to cover a large surface area to facilitate heat-sinking and a robust inter-layer connection. Both top and bottom sides are populated.

In practice, the performance of all devices are governed by board-level dynamics. There are far too many to discuss here, as this depends on the PCB's dielectric composite material properties; the geometry, weight, and conductivity of traces, the use of ground planes for heat-sinking, signal isolation, and countless others. Using longer trace length(s) increases signal path inductance, whereas addition of more plated thru-hole (as well as inter-layer) vias will increase parasitic capacitances. When designing multi-layer PCBs, carefully choosing how the overall stack-up of layers are defined can help minimize these effect.

Layers comprising the first PCB designed are shown in Figure B.1. This board is housed in the Explorer robot, and is referred to as the robot's main PCB (see Appendix B.2.1 for further details). The fuel-gauge section within this PCB (roughly the top one-third portion of the board) was also modified to facilitate proof of concept, and also initial testing, for use in subsequent high-capacity LiPB packs. These later designs make use of a different circuit to

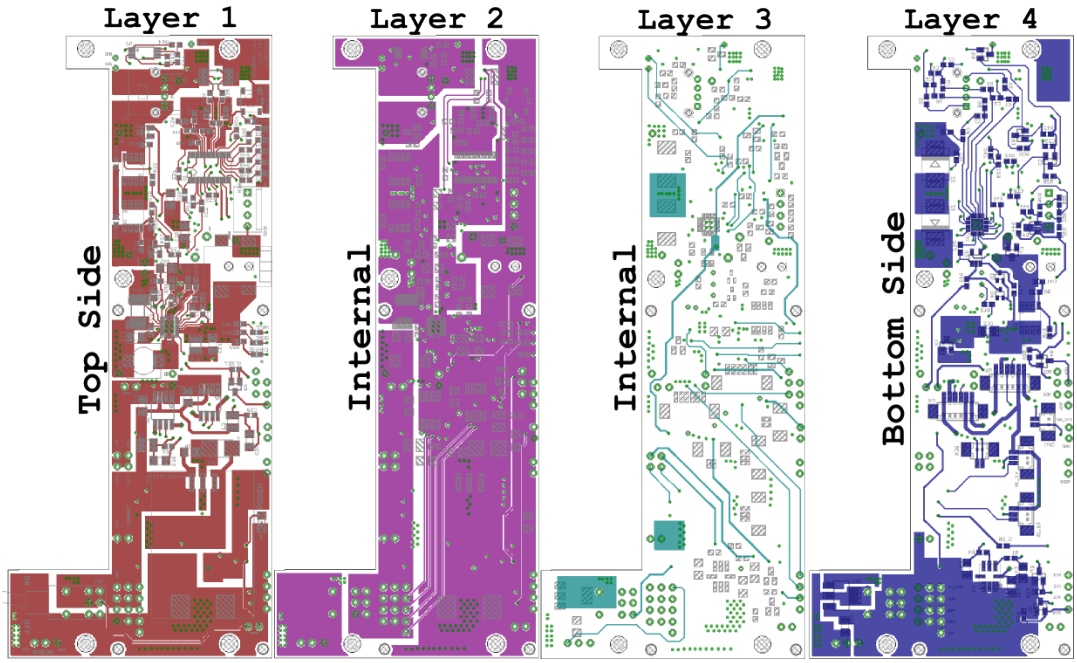

Figure B.1: Each of the four layers comprising the Explorer robot's main PCB. Layers shown from left to right (respectively) are: the top component side layer, second and third internal layers, and lastly the bottom component side layer. Each layer "slice" is illustrated as transparent; meaning, they are depicted as if "looking thru" the board (as a whole) from top to bottom - so *none* of the pictured layers have been mirrored.

accomodate larger bypass currents for balancing individual cells while charging.

Since robots do not all demand the same peripheral components and onboard devices, in an effort to promote a scalable means to track battery dynamics in other system designs, the entire fuel-gauge circuit was layed out on a seperate PCB. Shown in Figure B.2, are all four layers that make up this board (which is set up for a $3_S Y_P$ wired pack). This design was successfully applied in several different custom mobile robotic platforms. Specifically for the 1320 mAh $3_S 1_P$ LiPB packs in Explorer robot (introduced in Section B.2.1), and the high capacity 7600 mAh $3_S 4_P$ LiPB packs in the mobile docking and recharging station (detailed below in Section B.2.2) - which is the same LiPB pack and fuel-gauge PCB set-up employed in another custom platform, the micro-Vision robot (but will not be discussed in this thesis).

The PCB shown in Figure B.2 was slightly modified in both hardware and software serving a proof-of-concept design to accomodate use in $2_S Y_P$ packs. After extensive testing evinced favorable results, a slightly smaller PCB was designed. So despite the fact that the previous version PCB could easily have been used, this new system's size and weight requirements posed some additional unavoidable constraints. Thus a different PCB was designed for the 1900 mAh

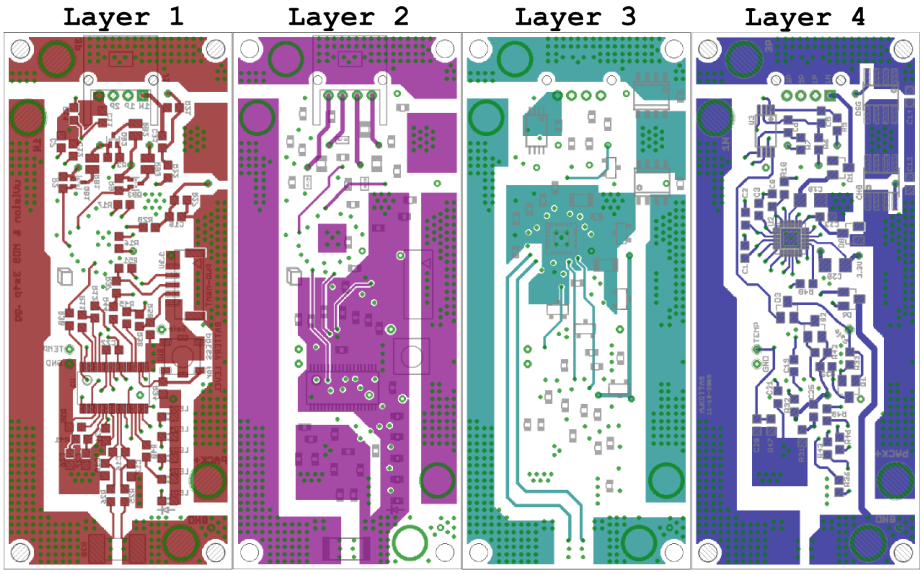

Figure B.2: Each of the four layers comprising the $3_S Y_P$ LiPB's fuel-gauge PCB. Layers shown from left to right are: the top (component side), internal layers 2 and 3, and lastly the bottom (component side) layer. Each layer "slice" is illustrated as transparent; meaning, they should be thought of as if "looking thru" the PCB (from top to bottom) as a whole - so *none* of the images have been mirrored.

$2_S 1_P$ LiPB pack onboard the Aqua-Pod robot (see Section B.2.3). Each of the PCB's four layers are shown in Figure B.3.

B.2 Robot Experimental Test Platforms

This section describes three custom mobile robotic platforms which house the designed PCBs (see above), as well as the batteries detailed in Appendix C.

B.2.1 Explorer Robot

The main robotic test platform is a custom-designed TWMR platform, the Explorer robot - introduced in [55], discussed in [56], and illustrated in Figure B.5. The Explorer robot project started as a complete re-design of the previous generation TWMR educational platform, the eRosi robot - which was vastly limited in terms of computational capabilities (two 8-bit micro-controllers) and only near-field (Bluetooth) communication abilities. Both robots were proposed as a system to provide students and researchers with a safe, easy to use, scalable robotic platform, to use in projects and software algorithm development. In addition, the Explorer serves as the robotic system used with the mobile docking and recharging station, discussed below in

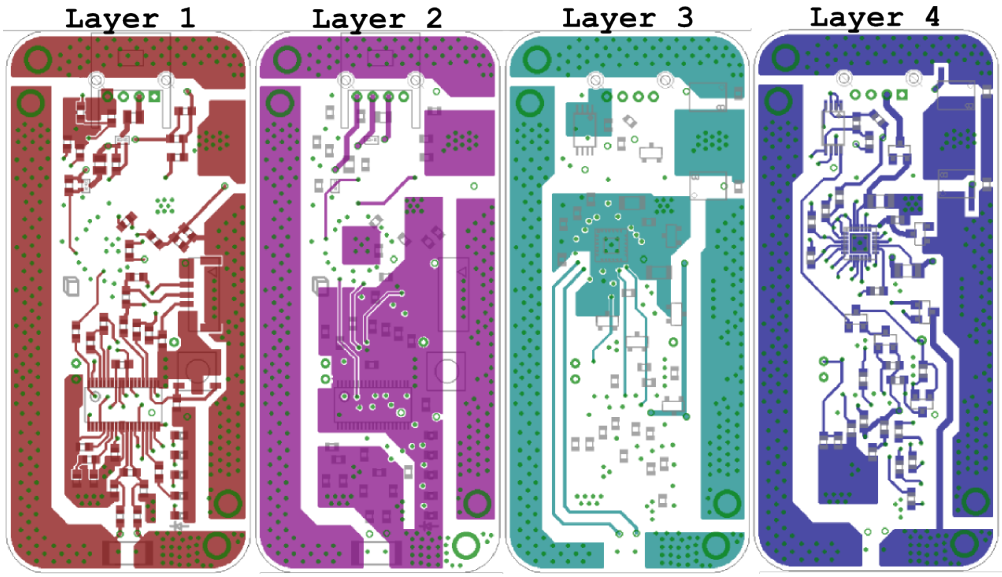

Figure B.3: Each of the four layers comprising the $2_S Y_P$ LiPB's fuel-gauge PCB. Layers shown from left to right are: the top (component side), internal layers 2 and 3, and lastly the bottom (component side) layer. Each layer "slice" is illustrated as transparent; meaning, they are depicted as if "looking thru" the PCB, from top to bottom (so *none* of the layers are mirrored).

Section B.2.2.

This differentially driven TWMR measures 14 x 6 x 4.5 cm in size, and is retrofitted with an additional servo to control the orientation of its stabilizing caster-tail, impelling a third degree of freedom to the robot's otherwise planar motion constraints, as discussed in Section 4.2.2.

The custom PCB shown in Figure B.1 is part of the robot's main chassis, as it is mounted in a manner so to play a role in maintaining overall structural integrity. This PCB serves as the central hub for all onboard systems, providing an interface between battery and load devices. These include, for example, the system's main DC/DC converter, motor drivers, sensors, and wide range of connectors (terminal block headers, sockets, and interconnects). In addition, the system-side fuel-gauge circuits are all embedded within this PCB, and utilize a leaded NTC thermistor to provide the necessary length to reach within the battery pack and make direct contact with the cells.

A high-level block diagram of the Explorer robot's onboard components and PCB arrangement is offered in Figure B.6. Although this figure does not show every intricate detail within each PCB, we can roughly see how these expansion boards are interconnected to the main, custom PCB.

This custom circuit board is actually one of a total of five PCBs used in the robot, and arranged in a stacked configuration (with the custom board sitting on the bottom). First in

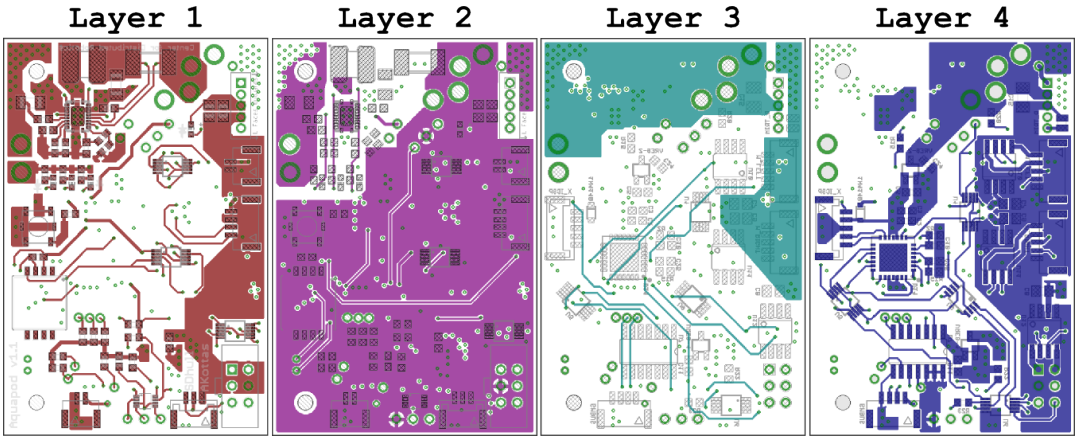

Figure B.4: Each of the four layers comprising the Aquapod Robot's custom main PCB. Layers shown from left to right are: the top (component side), internal layers 2 and 3, and lastly the bottom (component side) layer. Each layer "slice" is illustrated as transparent; meaning, they are depicted as if "looking thru" the PCB, from top to bottom (so *none* of the layers are mirrored).

this stack is an expansion board with an 8-bit microcontroller, versatile audio-codec chipset, a few voltage regulators and some serial bus level translators and converters. In addition, this PCB also serves as the break-out interface (through a 60-pin Hirose connector) to the next PCB in the stack. This second (and quite complex) PCB is a single-board computer (motherboard). It houses an ARM-core Marvell PXA270 (with XScale® microarchitecture core) 416 MHz processor, running the Ångström distribution Linux OS and Linux Kernel version 2.6.21. It also has flash memory ICs, a Bluetooth wireless radio module, a multi-output power management IC, and expansion connectors to build on the stack of PCBs. The third and fourth (final) boards that make up the overall stack on the robot, enable wireless 802.11(b/g) connectivity - providing network transfer rates up to 54 Mbps, and micro-SD card slot.

The battery pack used in the Explorer is based on the 1320 mAh LiPB cell discussed in Appendix C.1, and is wired in a 3_S1_P arrangement. The robot utilizes an embedded hardware fuel-gauge in a system-side configuration (defined from the viewpoint of the battery pack - in contrast to being housed internal to the pack itself), described in [56] and [35]. There are many benefits of embedding a hardware-based fuel-gauge to track power dynamics. It does not directly infringe on computational resources (as opposed to higher-level, software-based implementations), drawing current on the order of nano-Amperes. The hardware-based fuel-gauge closely monitors each cell, tracking their degradation throughout lifetime use, and providing capacity measurements accurate to within 1% error (specified by the IC's manufacturer and also observed in practice).

A highly integrated LiPB switch-mode charge management IC is also included on the robots

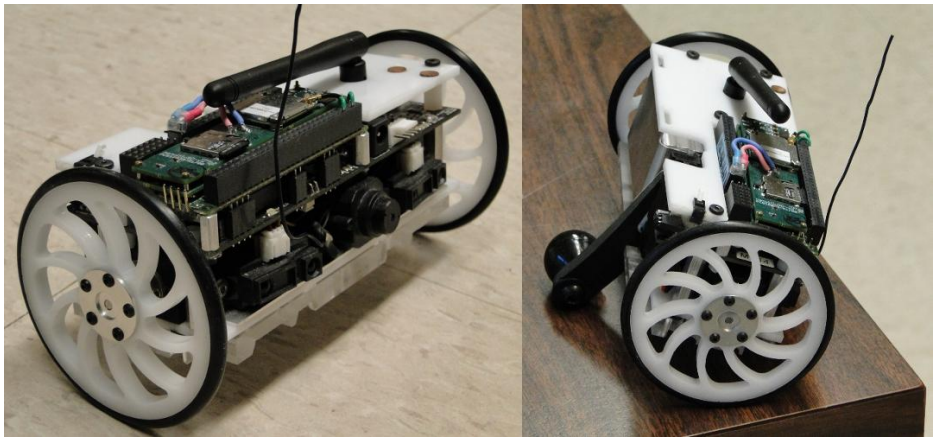

Figure B.5: The Explorer robot, one of the experimental robotic systems used in this work.

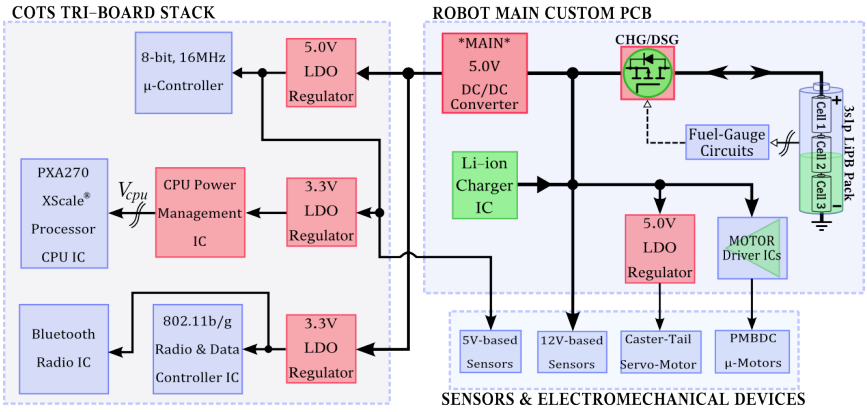

Figure B.6: A high-level block diagram generalizing the Explorer robot's PCBs and their housed peripherals.

main PCB. Configured to charge the LiPB pack at a 1·C rate, this assures the fastest charge time (while still ensuring safe operating conditions) for this particular cell chemistry. A direct connection power-path topology between charger and battery is implemented in the current design [57]. In this topology the external power supply is isolated from the LiPB and system by connecting the chargers output and batterys positive terminal directly to the system power bus. Alternatively, a path selection topology switches the systems supply rail from battery to the external power supply. This latter approach is more energy efficient, and should be considered to reduce residual losses when charging robots in-field via a mobile docking station (MDS). However, the direct connection topology was chosen for two main reasons. Firstly to effectuate design simplicity, both spatially (in terms of limited PCB real-estate) and monetarily (reducing the number of components used). The second is for allowing the robot to remain powered on

while charging, a decision made for a few reasons, but primarily to effectuate a simple solution for charging robots onboard the mobile docking and recharging station described in [34], [58], and [6]. However this feature also proves useful during firmware development and testing stages, where developers would otherwise have to wait until the robot recharges to program it - or even worse if the robot dies during programming (which can "brick" a device and require reflashing its bootloader).

B.2.2 Mobile Docking and Recharging Station

The fuel-gauge PCB described above in B.1 is the heart of an integrated multi-level power system architecture on a mobile docking and recharging station (MDS), introduced in [34], [58], and [6]. This system is proposed as a means to deploy/distribute, collect, and recharge smaller in-field mobile robots (specifically the Explorer robots in Section B.2.1) comprising a homogeneous distributed team. Figure B.7 is a picture of the MDS with four Explorer robots; one docked, another docking (actually being lifted by the fork-lift mechanism), and two waiting to dock.

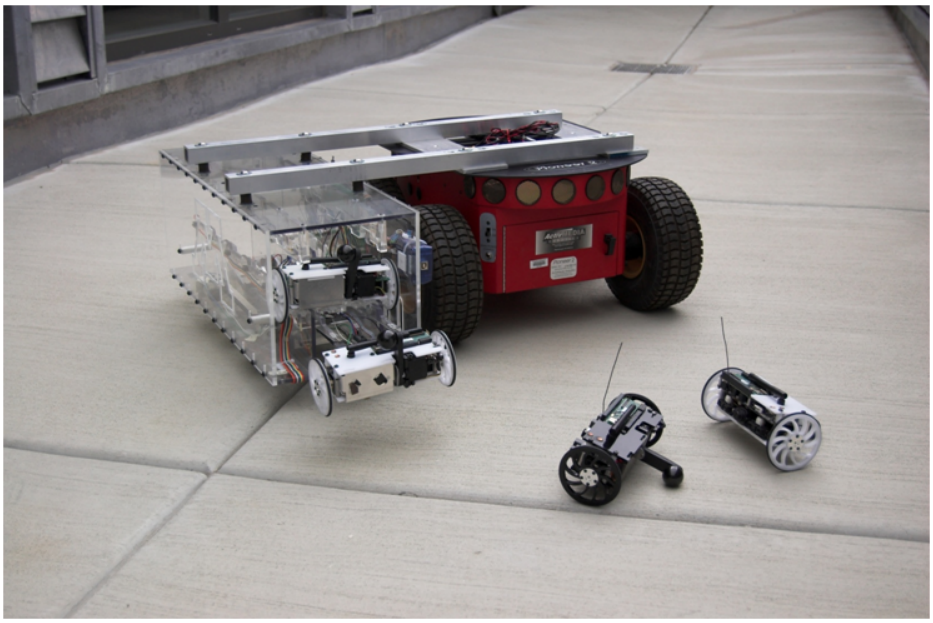

Figure B.7: The mobile docking and recharging station with four Explorer robots.

A simplified block-diagram of the MDS is illustrated in Figure B.8. Each onboard battery is equipped with a separate fuel-gauge PCB - marked as FG_x (for $x = 1, 2, ..., n$), all of which are controlled by a battery selector CPU. This design provides the general framework to construct an uninterruptable power supply (UPS) that addresses the energy demands from all load systems.

Currently, the MDS is configured with input plugs to accomodate using four of the 7600 mAh LiPB packs.

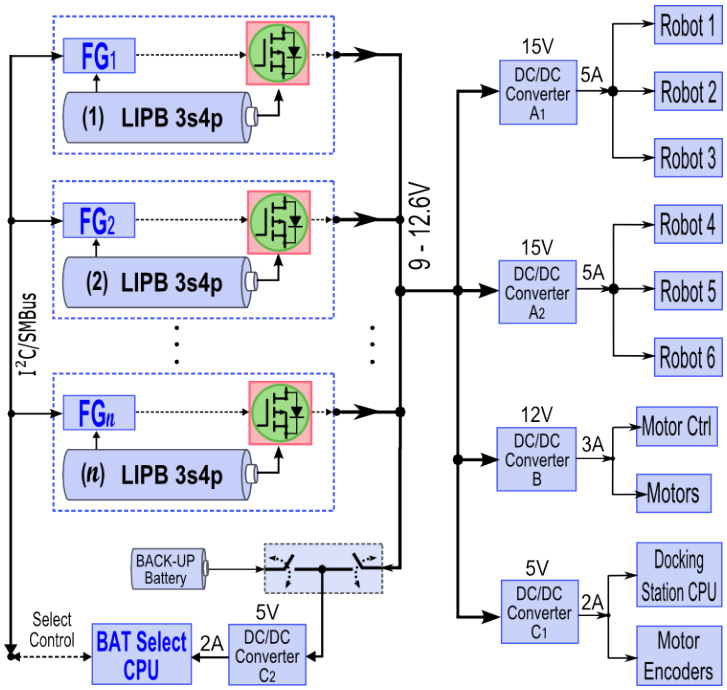

Figure B.8: High-level diagram generalizing the power architecture onboard the MDS.

The power infrastructure designed for the MDS forms the necessary foundation to incorporate a full, multi-level smart battery system manager, adhering to specifications detailed in [59]. On a similar note, it is worth mentioning that the resulting end (smart battery) system also supports the smart battery charger specification 1.1 [60]. The physical realization of these systems provide the preliminary pieces to build upon for realizing a distributed team of mobile robots with a mobile docking (and recharging) station to augment less capable entities within the team. The entire SBS-1.1 compliant smart battery power management solution onboard the MDS is further enhanced by a dedicated SBC capable of CPU frequencies upwards 416 MHz, Wi-Fi and Bluetooth, all on a (fanless) SBC running an embedded Linux Kernel.

Several details regarding the MDS design were omitted from this figure, mostly for clarity and limited space. One such omission for example is in the block labelled "motors," since five different motors were actually employed in the MDS's construction. Similarly, details regarding the DC/DC converters were not included. Some of these converters are quite complex, specifically the one outputting 12V as well as the two 15V output modules. These both are single-ended primary-inductance converter (or SEPIC) topologies, where the two converters with 15V outputs are fitted with large external heat-sinks since they provide input power to each of the housed

robots' chargers.

B.2.3 Aquapod Robot

The fuel-gauge circuit is also applied to power an aquatic mobile robot (Aquapod), whose electrical systems I designed alongside another graduate student. The designed power system for this robot is shown if Figure B.9. This architecture should look familiar to the example circuit shown in Figure 4.1. Both fuel-gauge PCBs were successfully applied in this robot, where the $3_S Y_P$ design was modified for $2_S 1_P$ use; as shown in Figure 6.6.

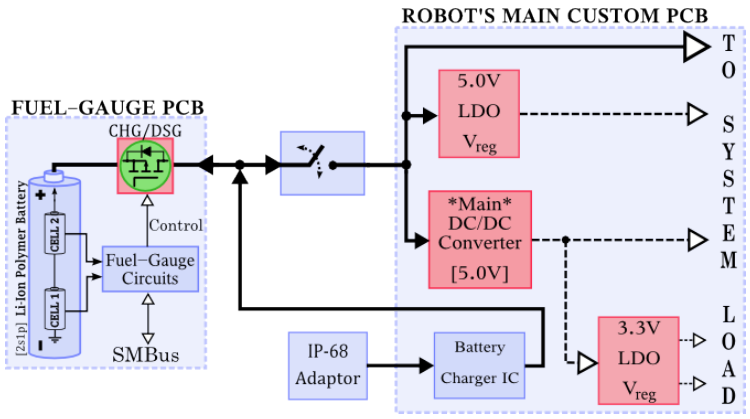

Figure B.9: Simplified diagram of the Aquapod robot's power system.

B.2.4 Roomba Robot Fuel-Gauge Integration

The same design was also verfied on a commercial robotic vacuum, the Roomba (from iRobot). Its original NiCd battery would no longer hold enough of a charge to even last for a minute. So the old NiCd pack was removed from its plastic housing and was replaced with a new custom battery pack, comprised of 1320 mAh cells (described in Appendix C.1) and were arranged in a $4_S 2_P$ custom wiring. This new pack's internal electronics - which rest on top of the new LiPB pack, are shown in Figure B.10 with the orignial casing opened up.

A control signal was wired to the robot's main ON/OFF switch, which toggles a line on the fuel-gauge PCB to induce a low-power sleep mode - for when the robot is off. In addition, the orignal NiCd battery pack's plastic enclosure was slightly modified, as three small segments were machined out from its top cover. One spot was fit with a push-button to query battery SoC. This is only useful if we can actually see the SoC level; so a transparent piece of acrylic was carefully glued under the second cut-out to facilitate viewing the fuel-gauge's LED indicator display. The third was for allowing easy access to the PCB's SMBus port, for programming, calibration, trouble-shooting, and data-logging during testing.

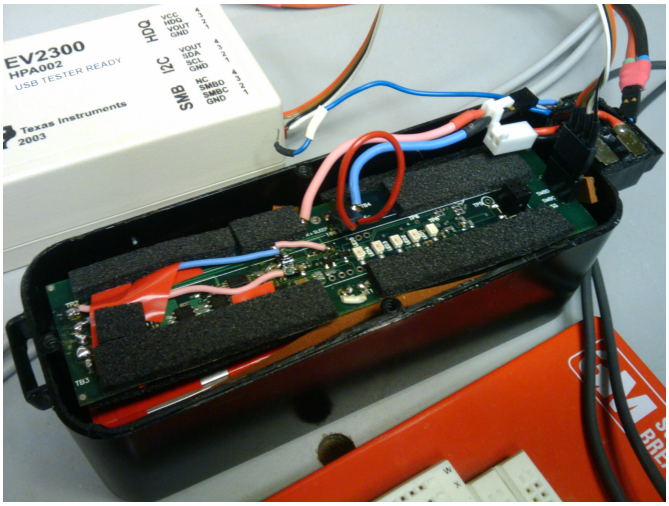

Figure B.10: The custom 4_S2_P LiPB pack's internal fuel-gauge PCB, shown during initial testing - with the Roomba's old battery case opened-up.

B.3 Overview of Hardware and Software Used

Several experiments performed to determine a device's power consumption independently, made use of the blank spare PCBs supplied as extras from the manufacturing facility. These boards were partially populated to accomodate the minimum number of components required to conduct the particular experiment(s) of interest. During testing, these PCBs were power by seperate power sources than those within the DUT, to facilitate unbiased measurements.

Data was collected from fuel-gauges (over SMBus) and the CSAs (via I^2C bus) by a PIC 16F1827 microcontroller, which contains the firmware for data logging. This in turn was streamed over a serial (UART) port to an external PC running a Python script - which logs and organizes acquired data in a tabular format (comma-separated values, or .csv). Finally, the Python-generated .csv log file was imported into MATLAB for data analysis and generating graphs.

The CSA used in experiments was the MAX9611, from Maxim IC. Measurements with the device were carried out on the manufacturer designed evaluation PCB. An Agilent DMM (model U1253B) provided verification of measurement accuracy. The armature inductance of motors were measured using an Agilent LCR meter (model U1732B).

For the data presented in Sections 4.4 and A.2, measurements were taken using a vector network analyzer (VNA), comprising an HP8753C network analyzer with 85046A S-Parameter test set. The VNA was calibrated using open, short, and 50Ω load terminations from calibration kit 85032B. All measurements were performed using phase-matched 50Ω APC-7 test-port cables (model 11857D).

To simulate the designed impedance matching network, a two-month student trial version of Agilent's Advanced Design System (ADS) suite was used.

The mechanical design software Pro/ENGINEER was employed to determine several parameters in the Explorer robot's CAD model. This was detailed in Chapter 5.

MATLAB version 7.9.0.529 (R2009b) was used to simulate various models, plot simulation their results, and to graphically visualize experimental data collected. Besides graphs generated in MATLAB, most of the other figures in this thesis were made using Inkscape, a vector graphics editor. Only a very small number of images were taken from other sources, which are explicitly noted in figure captions with links to their respective source references.

Appendix C

Li-ion Polymer Battery Details

To facilitate a coherent presentation of information throughout this thesis, many details regarding equations and calculations of battery dynamics have been redirected to this appendix chapter.

C.1 Cell Specifications

Two similar Li-ion polymer battery cells were used in this work, each with different nominal capacity. Individual cells are assembled however, into very different battery pack configurations. The first pack comprises 1320 mAh LiPB cells, and is wired in a $3_{\mathtt{S}}1_{\mathtt{P}}$ arrangement. The second is made using 1900 mAh cells, arranged in a $2_{\mathtt{S}}1_{\mathtt{P}}$ configuration. These two cells' discharge capacity versus terminal voltage specifications are shown in Figure C.1.

A third LiPB pack, based on the same 1900 mAh cells (connected as $3_{\mathtt{S}}4_{\mathtt{P}}$), was also employed in some experiments and research extensions (such as in [56]. This configuration results in a 7600 mAh pack, capable of outputting very high discharge currents; and can easily be used with the same fuel-gauge circuit (and PCB) detailed in Appendix B.1, requiring only minimal modifications.

Each LiPB cell is encased in a flexible aluminum (foil-like) laminate film pouch, which offers a thin, lightweight, stackable form factor. Individual cells were manufactured by Ener1 of Korea (formerly Saehan-Enertech), although they are wired and assembled into a final COTS product by Thunderpower RC - a well-known supplier of LiPBs to hobbyists and R/C enthusiasts alike. The anode (negative) electrode's Cu-foil current collector is coated with a thin layer of graphite, as carbon black powder. A lithium cobalt oxide ($LiCoO_2$) crystalline film is deposited on the cathode (positive) terminal's Al-foil substrate in the form of a powder slurry. The cell manufacturer specifies in their material safety datasheet that $LiCoO_2$ and carbon have specific gravity 4.95 and 2.09–2.2, respectively. It is also noted that the material used for the cell's

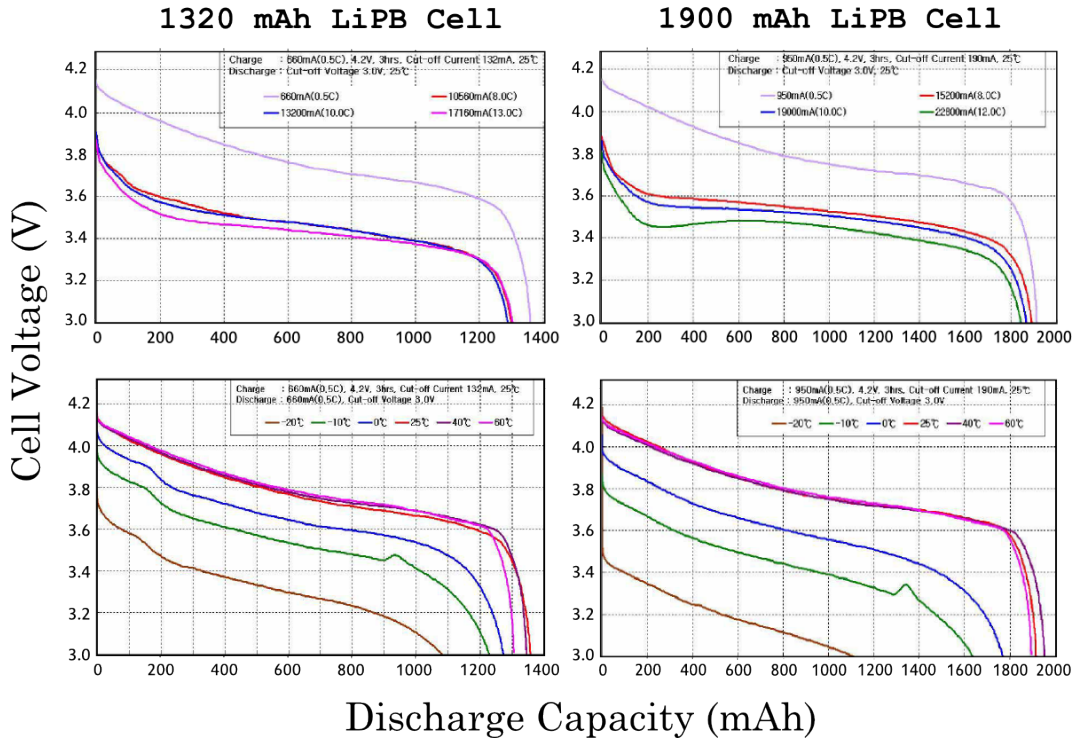

Figure C.1: Discharge capacity (in mAh) versus cell voltage (in Volts), for various load currents (top two figures) and temperatures (bottom two graphs). The *left* two plots are for the 1320 mAh LiPB cell [5], and the *right* two correspond to data for the 1900 mAh LiPB cell [2] used in this work. Graphs were reproduced from the noted sources (given by the cell manufacturer), but were modified from their original form mainly because of space constraints and for clarity (since most of their fonts and graphics were illegible).

polymer binder is polyvinylidene (di)fluoride (PVdF).

C.1.1 Li-ion Battery Modeling Details

The observed V_{bat} differs from V_{emf} and V_{oc} because of internal voltage drops within cells. In general, a battery's *overpotential* (V_η) describes the total sum of all internal potentials that arise during charging or discharging. These potentials are consequent to many possible rate-limiting mechanisms, such as ionic mobility, diffusion, and several others - each contributing to V_η differently. Overpotentials are often modeled seperately before superimposed to obtain a single, equivalent V_η. Equation C.1 shows how V_η relates to V_{emf}, V_{oc}, and V_{bat}.

$$\begin{aligned} V_\eta &= V_{emf} - V_{bat}|_{I_{dsg}=0} \\ &= V_{emf} - V_{oc} \end{aligned} \tag{C.1}$$

Usually V_η is decomposed into three sub-components. These are the diffusion, kinetic, and Ohmic overpotentials, abbreviated $V_{\eta,dif}$, $V_{\eta,kin}$, and $V_{\eta,\Omega}$ (respectively). Developing an appropriate V_η model is an fundamental step in electrochemical cell analysis. Not to mention, each V_η is given variable, often ambiguous, definitions in literature. Thus each merits some clarification.

- $V_{\eta,\Omega}$ – This is the Ohmic, or sometimes called $I{\cdot}R$, polarization. It describes the voltage drops attributed to cell construction, materials properties (often lumping electrolyte resistance in this term). This is the dominant overpotential observed throughout most SoC levels during a discharge cycle.

- $V_{\eta,dif}$ – Also known as the mass-transport overpotential, this accounts for ionic diffusion at the electrode-electrolyte interface.

- $V_{\eta,kin}$ – This overpotential is often divided into two sub-potentials. These are the activation and concentration polarizations ($V_{\eta,actv}$ and $V_{\eta,conc}$), which represent overpotentials from reaction kinetics associated with charge-transfer and mass-transfer, respectively.

Depending on operating conditions and state of charge (SoC), contributions from each overpotential to the total V_η can be weighted. For example, it is known that there is an increase in $V_{\eta,dif}$ when the battery approaches empty [36]. Hence equivalent circuit models offer a means to couple empirical observations of internal electrochemical processes with electrical analogies. These models range in complexity from approximating a battery's internal impedance as a single real-valued resistance, to detailed distributed-parameter circuit networks which model spatio-temporal effects. Lying somewhere in between (in terms of complexity) are a variety of lumped-parameter circuits that use a small number of passive elements to model cell dynamics. One such circuit widely used for its simplicity and effectiveness in AC battery modeling, is the Randles equivalent circuit - shown in Figure C.2.

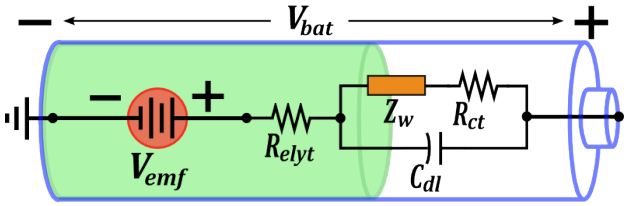

Figure C.2: The Randles equivalent circuit, where Z_w denotes the Warberg impedance element, C_{dl} the electrical double-layer capacitance, R_{elyt} represents the (combined) electrolyte and seperator resistance, and R_{ct} the charge-transfer resistance.

Each overpotential is often ascribed an equivalent impedance. So using $V_{\eta,dif}$ again as an example, the influence from mass-transport on concentration changes when applying some load current stimulus, is represented by a so-called Warburg impedance element (Z_w). The Warburg

impedance is a constant phase element modeling linear diffusion across a semi-infinite plane $[0, \infty)$, and characterizes the 45° slope seen at lower frequencies in cell's complex impedance spectrum - as tabulated on a Nyquist plot (see Figure 3.1). For a general constant phase element (CPE) impedance Z_{CPE} defined per Equation C.2, Z_w is defined by setting $n = 1/2$. Here f_{dsg} is the frequency of applied discharge stimuli, and $Z_{0,cpe}$ represents a DC reference impedance.

$$Z_{CPE} = \frac{Z_{0,cpe}}{(j \cdot 2\pi \cdot f_{dsg})^n} \tag{C.2}$$

All dynamic parameters are subject to change with ambient temperature ($T_{amb,K}$). Ambient temperature dependence is shown in the top two graphs of Figure C.1. Internal temperature variations are clearly observed by noting the "dips" in the bottom two graphs in the same figure. These dips are a consequence of self-heating effects generated within the cells. Increasing environmental temperature during operation, will result in decreased internal cell impedance.

It is not of interest to go into great detail about the electrochemical inner workings LiPBs. The following subsection briefly highlights some important features in LiPB electrochemistry and thermodynamics analysis, to provide a better understanding of the chosen battery chemistry's dynamics.

C.1.2 Electrochemistry

Charge transfer in a LiPB occurs when electrons disseminate between heterogeneous chemical species - for example, from electrolyte to solid-state electrodes. Hence this charge transfer process is termed heterogeneous electron transfer. LiPBs are fabricated using several different materials types, although the specific cells considered here comprise a graphite anode and $LiCoO_2$ cathode.

When discharging, lithium ions de-intercalate (are extracted) from the anode's (negative) crystal matrix structure, and are adsorbed at the cathode (positive terminal). The positive electrode half-reaction is summarized in Equation C.3, where the forward arrow direction indicates discharge. Similarly, Equation C.4 shows the negative electrode half-reaction.

$$\mathrm{Li}_{1-x}\mathrm{CoO}_2 + x\mathrm{Li}^+ + x\mathrm{e}^- \rightleftharpoons \mathrm{LiCoO}_2 \tag{C.3}$$

$$\mathrm{Li}_x\mathrm{C}_6 \rightleftharpoons x\mathrm{Li}^+ + x\mathrm{e}^- + 6\mathrm{C} \tag{C.4}$$

A first attempt towards formulating a closed-form expression often starts from noting that several electrochemical and thermodynamic parameters follow an Arrhenius-type (decreasing

exponential) behavior [9]. The Arrhenius equation relates the rate constant of chemical reactions (k_{chem}), to the thermodynamic temperature (T_K) and activation energy (E_a), as shown in Equation C.5. Here a_T is the pre-exponential temperature parameter, and R_{gas} the Gas constant.

$$k_{chem} = a_T \cdot e^{-E_a/(R_{gas} \cdot T_K)} \tag{C.5}$$

In principle, an equation for V_{oc} can be found from thermodynamic data and Equation C.6 - the Nernst equation. Variables z, and $[a]$ represent, respectively, the number of moles of electrons exchanged in the reaction, and the chemical activity of reduced and oxidized species (shown with subscripts *red* and *ox*). The standard electrochemical electrode (reduction) potential is written $V_{red}^{\ominus}$ which can be found in many texts (such as [14]), along with the Faraday constant F.

$$V_{red} = V_{red}^{\ominus} - \frac{k_{chem} \cdot T_K}{z \cdot F} \cdot \ln \frac{[a_{red}]}{[a_{ox}]} \tag{C.6}$$

Using standard electrode (reduction) potentials along with the Tafel equation, we can relate discharge current density (J_{dsg}) to V_η. The Tafel equation, a more general form of the Butler-Volmer equation, is given in Equation C.7, for characteristic constants A_η and B_η of the electrode system. B_η gives some insight to the reaction mechanism, while A_η provides information about the reaction's k_{chem}.

$$V_\eta = A_\eta \pm B_\eta \cdot \log |J_{dsg}| \tag{C.7}$$

Since a Li-ion cell will release heat during discharge conditions, we know the discharge reaction is exothermic. Hence the change in enthalpy (ΔH) is negative. Also assumed, is that the cell's internal pressure does not change to a degree that would influence its ability to output energy. From this assumption, and since the aim of such an analysis is to find a cell's ability to do useful work, it makes more sense to use the Helmholtz (versus Gibbs) free-energy $A_{f,E}$ to describe the cell's available internal energy. The definition of $A_{f,E}$ is given in Equation C.8, where ΔS is the change in entropy, and $U_{int,E}$ the system's (i.e. the battery's) internal energy.

$$A_{f,E} \equiv U_{int,E} - T_K \cdot \Delta S \tag{C.8}$$

Using the fundamental law of thermodynamics, with δQ_c representing incremental heat differentials within a cell, and dW_c the work performed on/by the cell, we get Equation C.9. For constant ambient temperatures, any change(s) in cell temperature during normal (discharge) operation will be attributed to δQ_c [61].

$$dU_{int} = \delta Q_c - \delta W_c \tag{C.9}$$

There are far too many parameters to model, estimate, and moreover calculate in order to fully characterize a LiPB's dynamics; that is, following a theoretical electrochemistry-based approach. The large number of uncertainties, not to mention computational complexity, involved in such an algorithmic formulation makes this an unattractive solution for use in portable, embedded systems. Regardless, this kind of analysis can prove beneficial when analysis is performed off-line, since it may uncover some possible underlying simplifications in a battery model.

Appendix D

Glossary and Acronyms

Care has been taken in this thesis to minimize the use of jargon and acronyms, but this cannot always be achieved. This appendix defines jargon terms in a glossary, and contains a table of acronyms and their meaning.

D.1 Glossary

- $X_S Y_P$ **cell configuration** – Describes the arrangement of cells within a battery pack. The X_S part refers to the number (X) of series connected cells in the pack; and the Y_P portion denotes the number (Y) of parallel connected cells. Larger numbers in X give rise to increased (total) battery pack voltage; whereas larger Y increases the overall battery pack's capacity. For a single cell battery, we have a $1_S 1_P$ configuration.

- x·E **rate** – Used as an alternative to C-rates (see the definition below), although both are used in reference to a particular rate of (dis)charge. A 1·E discharge rate denotes the electrical *power* required to discharge a battery in one hour. All E-rates are given as ratios or multiples with respect to E_{fcc}. So for a discharge rate x (where $x = E/E_{fcc}$), if $x \geq 1$, then the particular E-rate of discharge is written as x·E. On the other hand, if $|x| < 1$, then x is replaced by its fractional form (for example, if $x = 0.25$, then 0.25·E is written E/4).

- x·C **rate** – Defined as the electrical *current* required to (dis)charge a battery in one hour. This is particularly confusing when talking about charging, since a 1·C rate does not imply charging the battery in one hour, but instead gives the electric current magnitude at which constant-current mode charging is performed. C-rates specify (dis)charge rates with respect to Q_{fcc} - the battery's full-charge capacity. So abbreviations using ratios and

multiples (for example, C/2 and 1·C, respectively) are similar to those described above for E-rates, but with respect to Q_{fcc} instead of E_{fcc}.

- **Open-circuit voltage** (V_{oc}) – This is sometimes referred to as OCV in other literature. Nevertheless, it is defined as a battery cell's voltage under *no-load* conditions. Note, this is *not* the same as a battery cell's EMF voltage (V_{emf}).

- **Electromotive force voltage** (V_{emf}) – Describes the battery terminal voltage when in a fully relaxed (i.e. equilibrium) state. Here *relaxed* suggests all cells comprising the battery pack have had "adequate" time to rest - after being perturbed. The required rest time for a cell to reach its equilibrium voltage V_{emf} greatly depends on the specific cell's chemistry, the applied (dis)charge load stimulus (whether constant-current, power, or resistance), cell and ambient temperatures, SoC, cell age, and the battery's cycle-count. It is also important to note that $V_{oc} \neq V_{emf}$ necessarily, or at least not immediately. Instead V_{oc} approaches V_{emf} as the battery is allowed sufficient time to relax after some (dis)charge load disturbance(s).

- **Overpotential** – A battery or battery cell's *overpotential*, represents (by definition) the difference battery's V_{emf} and the (dis)charge battery voltage [40]. See Chapter 3 and Appendix C for further details.

- **Low drop-out** (**LDO**) – A specific type of (linear) voltage regulator which, as its name implies, is capable operating normally at drop-out voltages (V_{ldo}) much lower than traditional linear voltage regulators. For a given input and output voltage ($V_{r,in}$ and $V_{r,out}$, respectively), the regulator's V_{ldo} is defined as the minimum input-output voltage differential such that the component can still perform within its normal specified operational limits. In other words, $V_{ldo} < \min |V_{in} - V_{out}|$. As the right-hand side of the inequality approaches V_{ldo}, small changes in output (load) current (or even temperature) can brown-out the IC and compromise its functionality.

- **Single-board computer** (**SBC**) – A type of computer, usually fanless, which utilizes a system-on-chip CPU containing all onboard peripherals locally. These may include static and dynamic memory ICs, power supplies and converters, and many others; all on a single PCB (hence the nomenclature).

- **Wi-Fi** – An acronym for "wireless fidelity," which, over time, has become synonymous with simply *wireless* - as in *wireless device(s)*. In this thesis, a Wi-Fi radio describes a device that conforms to the wireless LAN regulatory standards set by the Wi-Fi Alliance consortium, a working group of the IEEE 802 project's LMSC. These regulations embody a wide range of standards for wireless data transmission at frequencies that reside in the 2.4–5 GHz band region; such as various 802.11(a/b/g/n)-based protocols.

D.2 Acronyms

Table D.1: Acronyms

Acronym	Meaning
IC	Integrated circuit
CPU	Central processing Unit
CAD	Computer-aided design
COTS	Commercial off-the-shelf
DUT	Device under test
DMM	Digital multi-meter
VNA	Vector network analyzer
SBC	Single-board computer
PCB	Printed circuit board
RAM	Random access memory
SDRAM	Synchronous dynamic RAM
MOSFET	Metal-oxide semiconductor field-effect transistor
CMOS	Complementary metal-oxide semiconductor
TTL	Transistor-transistor logic
DCR	DC resistance
ESR	Equivalent series resistance
LED	Light emitting diode
IR	Infra-red
MEMS	Micro electromechanical system
CSA	Current-sense amplifier
ADC	Analog-to-digital converter (sometimes referred to as “A2D”)
NTC	Negative-temperature coefficient
ppm	Parts per million
TWI	Two-wire interface
I^2C	Inter-integrated circuit bus (trademark of the Philips Corporation)
SMBus	System management bus (a trademark of the Intel Corporation)
SBS	Smart battery system (see [62])
PNGV	U.S. Partnership for a New Generation of Vehicles
LAN	Local Area Network
MAN	Metropolitan Area Network
Wi-Fi	Wireless Fidelity

Continued on next page

Table D.1 – continued from previous page

Acronym	Meaning
GSM	Global System for Mobile Communications
CDMA	Code division multiple access
GPS	Global Positioning System
LMSC	LAN/MAN Standards Committee
R/C	Radio (or remote) controlled
VHF	Very high frequency; defined from approximately 30 to 300 MHz
EMC	Electromagnetic compatibility
COG	Center of gravity
LOS	Line of sight
TWMR	Two-wheeled mobile robot
MRT	Mobile robotic team
MDS	Mobile docking (and recharging) station
Counter-EMF	Counter-electromotive force voltage (V_ω)
Back-EMF	Synonymous with counter-EMF (see above)
PWM	Pulse-width modulation
DVS	Dynamic voltage scaling
DFS	Dynamic frequency scaling
PMBDC	Permanent magnet brushed DC (motor)
DC/DC	DC-to-DC (power converter)
SMPC	Switch-mode (DC/DC) power converter
LDO	Low drop-out (voltage regulator)
Cu	Chemical symbol for element copper
Al	Chemical symbol for element aluminum
Ti	Chemical symbol for element titanium
$LiCoO_2$	Lithium cobolt oxide
LiC_6	Lithium graphite
PVdF	Poly(vinylidene fluoride)
Li-ion	Lithium-ion
LiB	Li-ion battery
LiP(B)	Li-ion polymer (battery)
AFE	Analog front-end
PMIC	Power management IC
DPPM	Dynamic power-path management
OCV	Open-circuit voltage

Continued on next page

Table D.1 – continued from previous page

Acronym	Meaning
EMF	Electromotive force (voltage)
SoC	State of charge (and *not* system-on-chip)
ASoC	Absolute SoC (relates to Q_{max})
RSoC	Relative SoC (relates to Q_{use})
DoD	Depth of discharge (DoD = 100− SoC)
EoD	End of discharge
SoH	State of health
FCC	Full charge capacity
V_{EoD}	EoD voltage; for LiPB cells considered here, $V_{EoD} = 3.0$V per cell
Q_{rem}	Battery's remaining charge
Q_{fcc}	Battery's full charge capacity
Q_{max}	Maximum chemical charge (relates to ASoC)
Q_{use}	Usable chemical charge (relates to RSoC)
(dis)charging	Short for "discharging or charging"
SMD	Surface mount device
SMP	Surface mount package (of a SMD)
BGA	Ball grid array (type of SMP)
QFN	Quad-flat no-leads (type of SMP)